LAND SURFACE EMISSIVITY VARIATIONS
AT INFRARED WAVELENGTHS FOR THE SELECTED REGIONS
IN TURKEY

A THESIS SUBMITTED TO
THE GRADUATE SCHOOL OF NATURAL AND APPLIED SCIENCES
OF
MIDDLE EAST TECHNICAL UNIVERSITY

BY

BERAT AKYÜZ

IN PARTIAL FULFILLMENT OF THE REQUIREMENTS
FOR
THE DEGREE OF MASTER OF SCIENCE
IN
THE DEPARTMENT OF PHYSICS

AUGUST 2011

Approval of the thesis:

LAND SURFACE EMISSIVITY VARIATIONS AT INFRARED WAVELENGTHS FOR THE SELECTED REGIONS IN TURKEY

submitted by **BERAT AKYÜZ** in partial fulfillment of the requirements for the degree of **Master of Science in Physics Department, Middle East Technical University** by**,**

Prof. Dr. Canan Özgen
Dean, Graduate School **of Natural and Applied Sciences**

———————

Prof. Dr. Sinan Bilikmen
Head of Department, **Physics**

———————

Assoc. Prof. Dr. Akif Esendemir
Supervisor, **Physics Dept., METU**

———————

Examining Committee Members:

Dr. Ali Alaçakır
TAEK

———————

Assoc. Prof. Dr. Akif Esendemir
Physics Dept., METU

———————

Assoc. Prof. Dr. Enver Bulur
Physics Dept., METU

———————

Prof. Dr. Raşit Turan
Physics Dept., METU

———————

Assist. Prof. Dr. Sinan Kaan Yerli
Physics Dept., METU

———————

Date: 26.08.2011

I hereby declare that all information in this document has been obtained and presented in accordance with academic rules and ethical conduct. I also declare that, as required by these rules and conduct, I have fully cited and referenced all material and results that are not original to this work.

Name, Surname: Berat Akyüz

Signature:

ABSTRACT

LAND SURFACE EMISSIVITY VARIATIONS

AT INFRARED WAVELENGTHS FOR THE SELECTED REGIONS

IN TURKEY

Akyüz, Berat

M.Sc., Department of Physics

Supervisor: Assoc. Prof. Dr. Akif Esendemir

August 2011, 98 Pages

In this thesis, land surface emissivity variations are examined with respect to the land surface type, wavelength, and time (season and month) for the seven selected regions in Turkey using MODIS emissivity database and precipitation amount. Investigating land surface emissivity variations are important in many applications and it is known that studies about these variations are done for many regions except Turkey. This study is prior knowledge for Turkey to be used in infrared (IR) background models, surface radiation budget calculations, and land cover type classifications specific for Turkey. The results indicate that precipitation has a great influence on monthly/seasonal emissivity values depending on the land cover type and causes spectral emissivity variations. As a result, we

determined appropriate IR wavelengths for the investigation of the seasonal emissivity variations and seasonal factors causing emissivity variations according to the land cover types.

ÖZ

TÜRKİYE'DE SEÇİLİ BÖLGELER İÇİN KIZILÖTESİ
DALGABOYLARINDA
KARA YÜZEYİ SALICILIK DEĞİŞİMLERİ

Akyüz, Berat

Yüksek Lisans, Fizik Bölümü

Tez Yöneticisi: Doç. Dr. Akif Esendemir

Ağustos 2011, 98 Sayfa

Bu tez çalışmasında, Türkiye'de seçili yedi bölge için kara yüzeyi salıcılık değerlerinin bitki örtüsü tipi, dalgaboyu ve zamana (ay ve mevsim) göre değişimleri MODIS salıcılık veritabanı ve yağış verileri kullanılarak incelenmiştir. Kara yüzeyi salıcılık değişimleri bir çok uygulamada önemlidir ve bu değişimler hakkındaki çalışmaların Türkiye haricinde pek çok bölge için yapıldığı bilinmektedir. Bu çalışma Türkiye'ye özgü kızılötesi (KÖ) karasal arkaplan modelleri, yüzey ışıması hesaplamaları ve bitki örtüsü tipi sınıflandırılması çalışmalarında ön bilgi olarak kullanılabilecektir. Sonuçlar, yağışın aylık/mevsimsel ve tayfsal salıcılık değerlerinde bitki örtüsüne bağlı olarak büyük etkiye sahip olduğu ve salıcılık değerlerinde değişimlere neden

olduğunu göstermiştir. Sonuç olarak, mevsimsel değişimlerin incelenmesi için uygun KÖ dalgaboyları ve bitki örtüsü tiplerine göre salıcılık değişimlerine neden olan mevsimsel faktörler bu çalışmada belirlenmiştir.

Anahtar Kelimeler: Kara yüzeyi yayınım katsayısı, Yayınım katsayısı değişimleri, Mevsim, Bitki örtüsü tipi, MODIS.

To my endless love……

ACKNOWLEDGEMENTS

I would like to express my deepest gratitude and thanks to Assoc. Prof. Dr. Akif Esendemir for his supervision, guidance, and suggestions during the development of this thesis.

I would like to express my sincere thanks to the Assoc. Prof. Dr. Cemil B. Erol at İLTAREN for reading, commenting, and making useful suggestions throughout the thesis.

I wish to thank all of my friends at İLTAREN for their encouragement, valuable contributions and suggestions during this study.

Special thanks go to my dear friends, especially Aybüge Çekinmez and Yağmur Atay, who are always ready to offer help and not leaving me alone.

It is a very big pleasure to express my special thanks to my love Tayfun Aytaç for reading and commenting again and again, his patience, and pure love. All this work would not be possible (remember nothing impossible) without your support. Thank you for everything.

A deep sense of appreciation goes to all my family members; Atiye, Aydın, and Burcu Akyüz for their love, patience, and constant support through-out my life. They are always there whenever I needed a hand.

TABLE OF CONTENTS

LIST OF TABLES

TABLES

LIST OF FIGURES

FIGURES

LIST OF ABBREVATIONS

ε: Emissivity

p: Precipitation amount

LST: Land Surface Temperature

IR: Infrared

MWIR: Midwave Infrared

LWIR: Longwave Infrared

TIR: Thermal Infrared

SRB: Surface Radiation Budget

ERB: Earth Radiation Budget

RSR: Relative Spectral Response

LUT: Look Up Table

cwv: Column water vapor

TOA: Top of Atmosphere

BRDF: Bidirectional Reflectance Distribution Function

SM: Soil Moisture

SMC: Soil Moisture Content

FC: Field Capacity

EOS: Earth Observing System

MODIS: MODerate resolution Imaging Spectroradiometer

ASTER: Advanced Spaceborne Thermal Emission Reflection
                Radiometer

AMSR-E: Advanced Microwave Scanning Radiometer

NDVI :   Normalized Difference Vegetation Index

IGBP: International Geosphere Biosphere Programme

MAS: MODIS Airborne Simulator

TIMS: Thermal Imaging Multispectral Spectrometer

IR-LSEMA: IR Land Surface Emissivity Analyses

TUG: Tübitak Ulusal Gözlemevi - TÜBİTAK National Observatory

GAP: Güneydoğu Anadolu Projesi-Southeastern Anatolia Project

LW$_n$: Net longwave radiation

NCAR: National Center for Atmospheric Research

CLM2: Community Land Model version 2

Jan: January

Feb: February

Mar: March

Apr: April

Aug: August

Sep: September

Oct: October

Nov: November

Dec: December

CHAPTER 1

INTRODUCTION

Thermal radiation is the emitted electromagnetic radiation from any object when it is at a temperature greater than absolute zero [1]. In other words, all matters with a temperature greater than absolute zero emit thermal radiation. Thermal radiation is released by the vibration of atoms when heat energy increases [2]. Heated matters radiate energy in the IR region of the electromagnetic spectrum extending from 0.75 to 1000 µm, which has subdivisions near IR (NIR) (0.7-1 µm), shortwave IR (SWIR) (1-3 µm), midwave IR (MWIR) (3-5 µm), longwave IR (LWIR) (8-12 µm), and very longwave IR (VLIR) (>12 µm) [3]. Inherent efficiency of the matter converting heat energy into radiant energy is defined as emissivity [4].

Land surface emissivity is the spectral emissivity of the soil surface in bare areas or at the top of the canopy in vegetated areas [4]. It depends on the surface characteristics and dynamic parameters such as, surface composition, moisture content and meteorological conditions [4][5]. It is expected to show significant variations depending on the seasonal effects (snow, rain, drought etc.), land cover type (forest and bare soil), and spectral band range. Therefore, it is difficult to determine land surface emissivity and investigate its variations.

Determination of land surface emissivity and its variations under different conditions are important mainly for the IR background models, surface

radiation budget (SRB) calculations, land surface characterization, and geological applications [4]-[7]. For instance, SRB, which is explained in detail in the Appendix, determines the amount of incoming and outgoing radiation by the land surface using its emissivity. Spatial and temporal variations of land surface emissivity cause SRB variations, which directly affect the atmospheric and oceanic circulations, their thermal conditions, and climate [7][8]. Therefore, emissivity variations should be taken into account for the emissivity estimation. Any error in the estimation of emissivity without considering its variations will result in two times larger error than that in the atmospheric correction [7]. For this reason, estimation of the land surface emissivity in different regions under different meteorological conditions is continuing to be a hot research topic.

Many studies have been proposed to estimate the land surface emissivity for better simulations of atmospheric models and SRB calculations [1][9][10]. However, there is a lack of global land surface emissivity survey and a common consensus in the determination of emissivity. For example, in the global climate models developed by the Center for Ocean-Land-Atmosphere Studies of the Chinese Institute of Atmospheric Physics, the land surface emissivity is modeled with the value of 1.0 or close to 1.0 for certain surfaces [8]. Such simple representations (constant emissivity assumption) neglect the spatial, temporal, and spectral variations of the emissivity and introduce errors, which are also discussed in the Appendix. For example, land surface emissivity is determined as 0.7-0.8 at 9 μm for the Saharan deserts. Assuming constant emissivity for this area as 1.0 will cause an error of about 15 W/m^2 in the annual net longwave radiation which is about 160 W/m^2 [9][10].

1.1 Objective of the Study

All studies about land surface emissivity and its variations are made for many regions such as Europe, Iran, Morocco, Sahara Desert, Northern Africa, and the Arabian Peninsula [6][8][11][12]. To the best of our knowledge no attempt has been made previously to examine the emissivity value and its spectral, seasonal, and regional variations for Turkey. There is a need of studies about land surface emissivity and its variations to be used in Turkey because these studies enable the researchers to develop more accurate IR background models, mine detection algorithms, extensive land cover maps and classification algorithms, and agricultural prediction systems. This is basically our main motivation in this thesis.

In this study, several regions from Anatolia having different land cover types and precipitation properties are selected in order to examine land surface emissivity variations. These variations are investigated for the selected regions using emissivity database and precipitation amount, which are obtained from MODerate Resolution Imaging Spectro-radiometer (MODIS) and the Turkish State Meteorological Services, respectively. Consequently, land cover type and month/season dependent land surface emissivity variations with respect to precipitation are examined for the selected regions using IR Land Surface Emissivity Analyses (IR-LSEMA) interface, which we developed.

The thesis is organized as follows: Chapter 2 introduces emissivity, land surface emissivity determination by remote sensing and MODIS with its emissivity retrieval algorithm. Chapter 3 reviews spectral land surface emissivity variations in terms of season and land cover type changes. In Chapter 4, selected regions for the Turkey are defined and land surface emissivity variations are investigated for those regions. Finally, results are discussed and directions for future research are provided in the last chapter.

CHAPTER 2

EMISSIVITY

Emissivity (ε) of an object, which is ability of emitting radiation, is defined as the ratio of the radiant emittance of the object to that of the blackbody at same wavelength and temperature as given in Equation (2-1) [2][3].

$$\varepsilon_\lambda = \frac{M(\lambda, T)}{M_{bb}(\lambda, T)}$$

(2-1)

Here, M and M_{bb} are the radiant emittance (W/cm^2) values of the object and blackbody, respectively, depending on the wavelength (λ) and temperature (T). Blackbody is a material that transforms heat energy to radiant energy at a possible maximum rate [2]. However, materials are not perfect blackbodies and they emit radiation depending on their own characteristics, i.e. spectral emissivities. Three types of radiators can be considered according to their ε variations with respect to the wavelength as shown in Figure 2-1 [3]:

- A blackbody or Planckian radiator; ε is constant and is equal to 1.0.

- A graybody; ε is independent of wavelength and is smaller than 1.0.

- A selective radiator; ε depends on the wavelength.
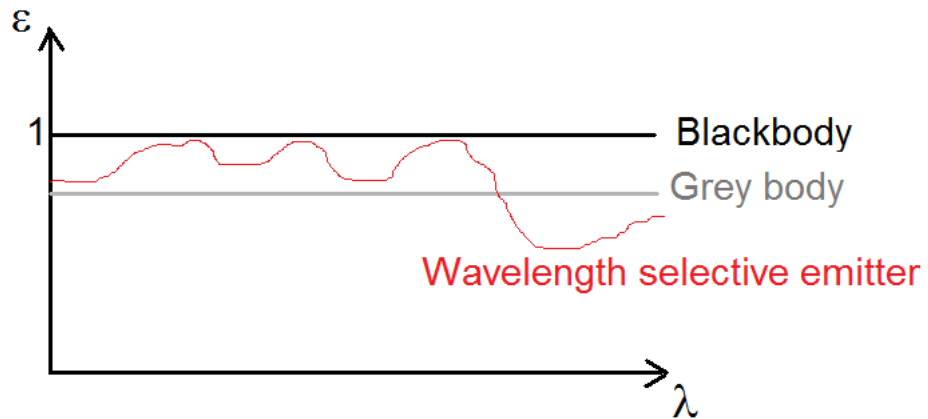
Figure 2-1 Spectral emissivity of three types of radiators [3].

For example, land surface generally behaves like wavelength selective emitter; however, in some cases it can behave like a graybody. Land surface ε values are generally greater than 0.8 because nonmetals have high ε values (ε>0.8) and polished metals have very low ε values (ε<0.1) as given in Table 2-1 [3].

Table 2-1 Emissivity of various common materials [3].

Material	ε
Glass: polished plate	0.94
Copper: polished	0.05
Copper: heavily oxidized	0.78
Water: distilled	0.96
Human skin	0.98
Brick: red common	0.93

Emissivity of a material is also a function of the direction. Therefore, ε can be classified according to the direction of measurement [3]:

- **Hemispherical emissivity:** It is defined as the ε of a source radiating into the hemisphere and is important for the calculation of the amount of heat transferred by radiation.

- **Directional emissivity:** It is measured in a small solid angle θ from the normal to the radiating surface.

- **Normal emissivity:** This is the particular case of the directional ε, where θ is zero. This ε type is conveniently used. Unless otherwise stated, ε is understood as normal ε.

Kirchhoff's law of radiation has a great importance in ε studies. This law states that a body is as good an absorber as an emitter [3][13]. The absorbance is equal to the emissivity, if the material, which is land surface in our case, is at thermal equilibrium with its surroundings (isothermal surface) [13]. It can be assumed that the Earth's surface and the atmosphere up to about 50–70 km are at local thermal equilibrium [13].

A fraction of incident energy on a surface may be absorbed, reflected, and transmitted. Due to energy conservation, following equation can be written as [3]:

$$a + r + \tau = 1 \tag{2-2}$$

Here α, r, and τ absorbance, reflectance and transmittance, respectively. As a result of the Kirchhoff's law, ε calculation from r is also possible for an opaque material (no transmittance) by using Equation (2-2) as follows [3]:

$$\varepsilon = 1 - r \ (\tau = 0) \tag{2-3}$$

This relationship is convenient because in some cases, r measurements are more practical for ε prediction when compared to ε measurements [3]. For example, determining land surface ε can be difficult due to the following reasons [9]:

- It is a dynamic surface property which can show variations with time.

- Land surface is composed of different land cover types with different ε.

Because of these difficulties, land surface ε can be derived from surface leaving radiation measured by remote sensing instruments for large areas [13]. For this reason, in most of the ε studies, land surface ε values are obtained from satellite data (MODIS, ASTER, and NOAA AVHRR etc.). In our study, we used land surface ε values from MODIS data, which is briefly explained in the following section. (From now on, ε is used to indicate land surface ε for brevity.)

2.1 MODerate Resolution Imaging Spectro-radiometer (MODIS)

NASA has carried out a program for long term observation, research, and analysis of the Earth's land, oceans, and atmosphere and their interactions including measurements from Earth Observing System (EOS). The EOS is funded by Earth Science Enterprise Program and includes a coordinated series of Earth observing satellites and an advanced data system for collection and analysis purposes [17].

MODIS and Advanced Spaceborne Thermal Emission Reflection Radiometer (ASTER) instruments installed on board of the NASA's EOS TERRA platform, which was launched in 1999, were designed to provide high quality observations of land surfaces (Terra), oceans (Aqua), and atmosphere [18]. Terra MODIS views the entire Earth's surface every 1 to 2 days and scans ± 55° from nadir in 36 spectral bands, which are changing in between 0.4 and 14.4 μm. As given in Table 2-2, seven of these bands are applicable for land studies.

Table 2-2 MODIS band used for land studies [19].

Band	Bandwidth (µm)	Primary use
20	3.660-3.840	Ocean and land studies
22	3.929-3.989	Atmospheric and land studies
23	4.020-4.080	Atmospheric and land studies
29	8.400-8.700	Land studies
31	10.780-11.280	Atmospheric and land studies
32	11.770-12.270	Atmospheric and land studies
33	13.185-13.485	Atmospheric and land studies

MODIS ε database has six bands (bands 20, 22, 23, 29, 31, and 32) ε values and relative spectral response (RSR) functions of these bands are shown in Figure 2-2 [29].

2.2 Land Surface Emissivity Determination from Remote Sensing Instruments

Some spaceborne technologies provide main surface parameters such as surface net radiation, vegetation index, soil moisture, land surface temperature, and ε [8][14]. As shown from the Figure 2-3, remote sensing instruments mainly measure the leaving surface radiation modified by the atmosphere in different spectral channels [8].
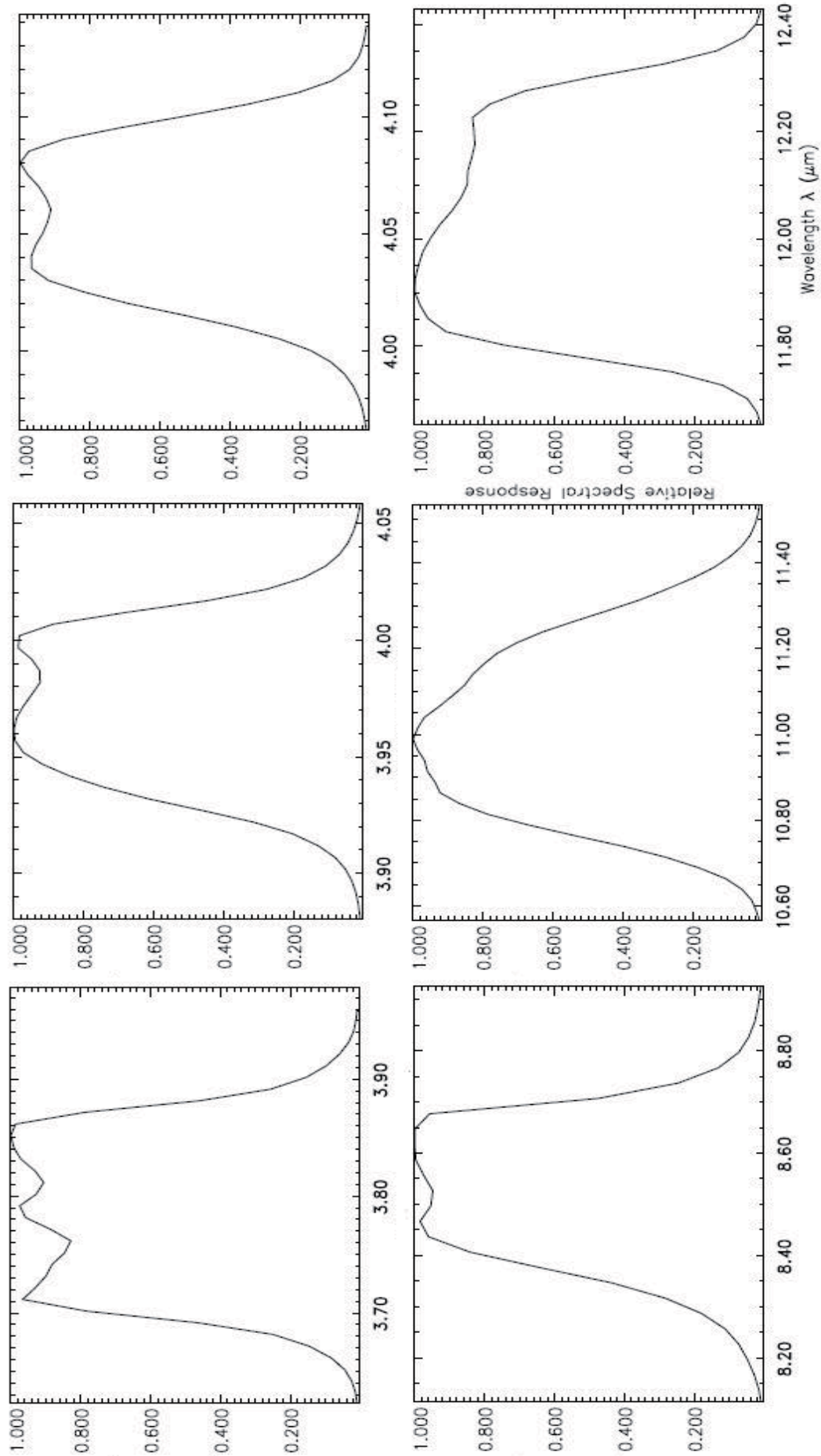
Figure 2-2 MODIS RSR functions for the six spectral bands 20, 22, 23, 29, 31, and 32, respectively [29].
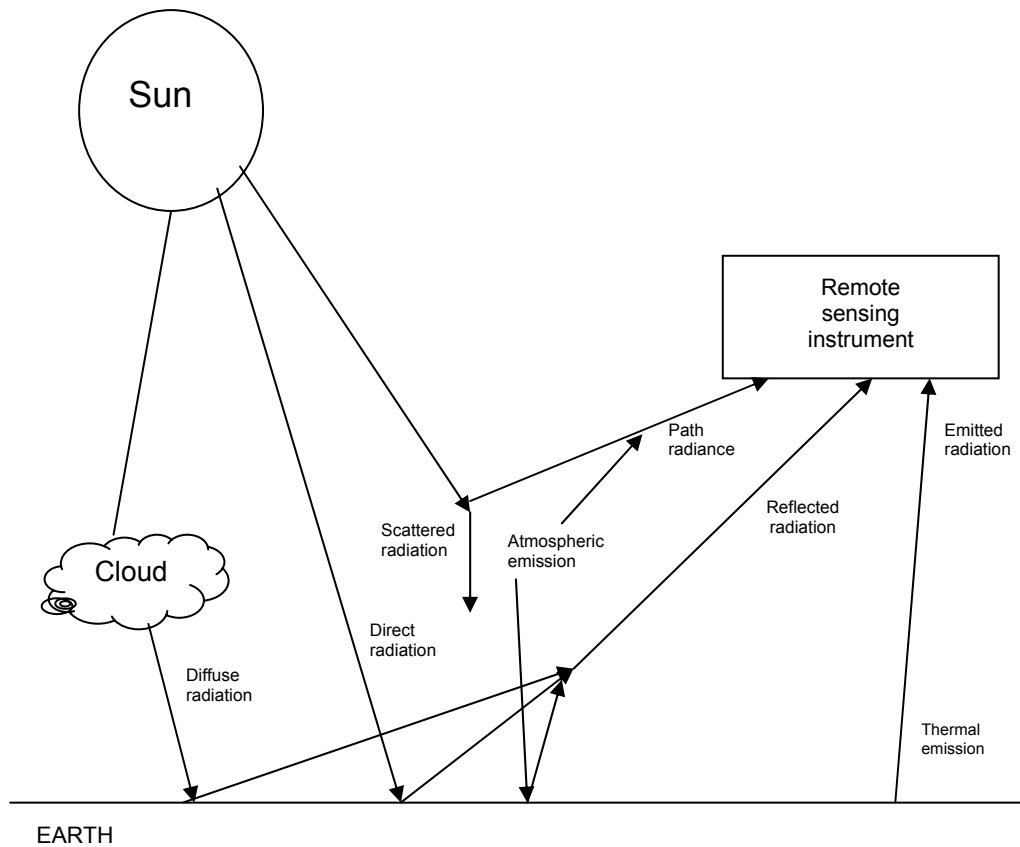
Figure 2-3 Radiance components observed by the remote sensing instrument.

Measured radiance (L(j)) by a satellite for the spectral band j at the top of atmosphere (TOA) under the clear sky conditions is composed of three basic components: path radiance (L_{path}), emitted radiance ($L_{emitted}$), and reflected radiance ($L_{reflected}$) as given in Equation (2-4) [7].

$$L(j) = L_{emitted}(j) + L_{path}(j) + L_{reflected}(j)$$

(2-4)

This equation is the simplified retrieval equation of any remote sensing instrument. In order to understand final retrieval equation, it is necessary to study the three components in detail.

2.2.1 Path radiance

Path radiance, which does not depend on surface properties, results from atmospherically scattered solar radiation (L_s) and thermally emitted radiance (L_a). This radiance can be expressed as in Equation (2-5) where λ is the wavelength center of the spectral band j (µm), µ and μ_0 are viewing and solar zenith angles, respectively, and Φ_0 is the relative azimuth angle (absolute difference between the viewing azimuth angle and the solar azimuth angle) [1][16]. These angles are shown in Figure 2-4.

$$L_{path} = L_a(\lambda, \mu) + L_s(\lambda, \mu, \mu_0, \phi_0)$$

(2-5)
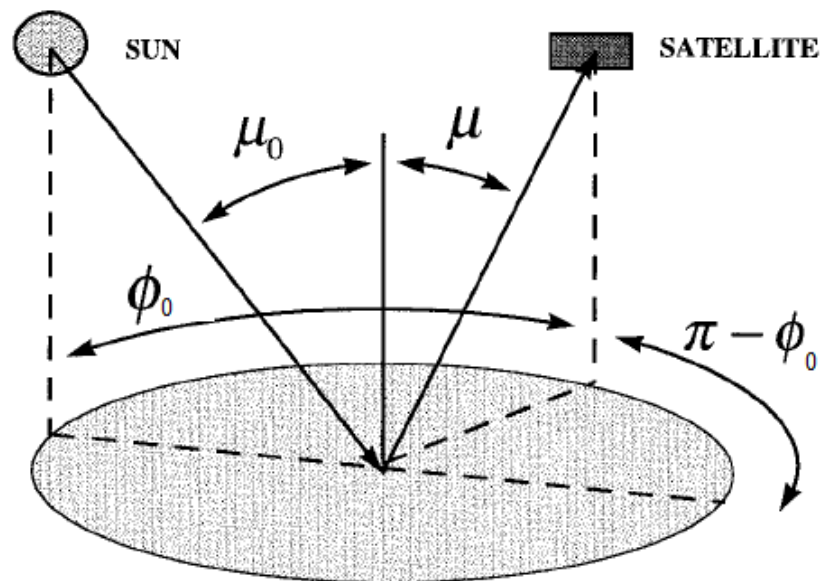
Figure 2-4 Angle representations [15].

2.2.2 Emitted radiance

The land surface is not at absolute zero temperature and radiates electromagnetic energy by itself according to Planck's law. Planck's law describes the spectral distribution of the radiation from a blackbody ($\varepsilon=1$) as

given in the Equation (2-6), where M represents the spectral radiance emitted by a blackbody (W/cm^2 µm), h is Planck's constant (h=6.6256x10^{-34} W sec^2), k is the Boltzmann constant (k=1.38054x10^{-23} W sec/$^\circ$K), c is the velocity of light (c=2.997925x10^{10} cm/sec), and T is absolute temperature ($^\circ$K) [3].

$$M(\lambda, T) = \frac{2\pi hc^2}{\lambda^5} \frac{1}{\exp(\frac{hc}{\lambda kT} - 1)}$$

(2-6)

Emitted spectral radiance (L$_e$) from a surface at wavelength λ and at thermal equilibrium surface temperature T$_s$ is given by Equation (2-7) where M is defined in Equation (2-6) [16].

$$L_e(\lambda, T_s) = \varepsilon M(\lambda, T_s)$$

(2-7)

Emitted radiance (L$_{emitted}$) in the simplified retrieval equation (Equation (2-4)), is the transmitted radiance through atmosphere, therefore, it is multiplied by the atmospheric transmittance (t) as given in Equation (2-8) [1][16].

$$L_{emitted} = t(\lambda, \mu) L_e(\lambda, T_s)$$

(2-8)

2.2.3 Reflected radiance and bidirectional reflectance distribution function (BRDF)

Solar radiance and atmospherically emitted radiance are reflected by the surface and constitute two main reflected radiance components in the simplified retrieval equation. As shown in Figure 2-3, solar radiation received at Earth's surface is mainly separated into direct and diffuse solar radiation [20]. The reflected radiance components, which are atmospherically emitted, direct, and diffuse solar radiation, can be represented by using BRDF. BRDF (f(θ$_r$, Φ$_r$, θ$_i$, Φ$_i$)) represents for each incoming angle (θ$_i$, Φ$_i$) the amount of

12

light which is reflected in each outgoing angle (θ_r, Φ_r) as shown in Figure 2-5.
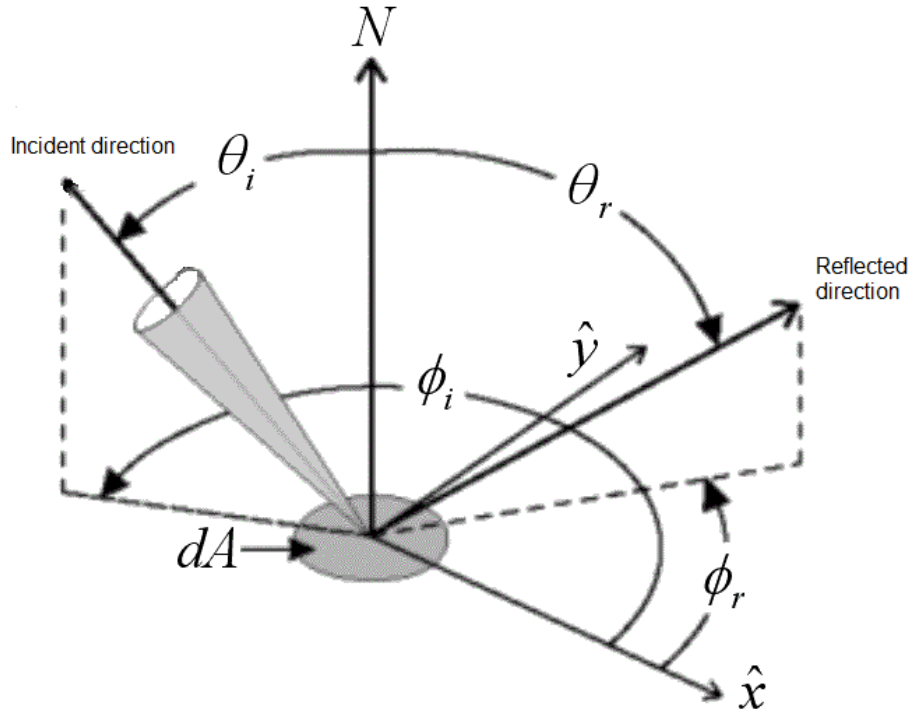
Figure 2-5 Light reflection geometry (BRDF) [21].

In general, reflected radiance (L_r) can be calculated by integrating BRDF and the incident radiance (L_i) over the whole sphere as given below [22]:

$$L_r = \iint_{\Omega} f(\theta_r, \phi_r, \theta_i, \phi_i) L_i(\theta_i, \phi_i) \cos(\theta_i) d\theta_i d\phi_i$$

(2-9)

For a Lambertian (perfectly diffuse) surface, which reflects light equally in all directions, BRDF is constant and is given in Equation (2-10), where r is the reflectance independent of direction [23].

$$f(\theta_r, \phi_r, \theta_i, \phi_i) = \frac{r}{\pi}$$

(2-10)

BRDF anisotropic factor (α_r), given in Equation (2-11), is defined by the ratio of the surface reflected solar beam at the view direction to the Lambertian surface radiance, where E_i is incident irradiance on the surface [16][19][23].

13

$$\alpha_r = \frac{dL_r}{\frac{r}{\pi}dE_i} = \frac{\pi f(\theta_r, \phi_r, \theta_i, \phi_i)}{r} \qquad \text{(2-11)}$$

Total reflected radiance has three components: reflected direct solar beam radiation, reflected diffuse solar radiation, and reflected atmospherically emitted downward thermal radiance as given in Equation (2-12) [1][16].

$$L_{reflected} = t_2(\lambda, \mu, \mu_0)\mu_0 E_0(\lambda) f(\mu; \mu_0, \phi_0) +$$
$$\int_0^{2\pi}\int_0^1 \mu' f(\mu; \mu', \phi')[t_3(\lambda, \mu)L_d(\lambda, -\mu', \phi') + t_4(\lambda, \mu)L_t(\lambda, -\mu', \phi')]d\mu' d\phi' \qquad \text{(2-12)}$$

Here, $E_0(\lambda)$ is spectral solar irradiance incident on TOA, $L_d(\lambda, -\mu', \Phi')$ is downward solar diffuse irradiance, $L_t(\lambda, -\mu', \Phi')$ is the atmospheric downward thermal irradiance, $-\mu'$ and Φ' are incident directions, $f(\mu, \mu', \Phi')$ and $f(\mu, \mu_0, \Phi_0)$ are BRDF functions, and t_i (i=1,…,4) are the band effective transmission functions [16].

2.2.4 Final retrieval equation

As explained previously, path, emitted, and reflected radiance components constitute retrieval equation, which describes total radiation received by the remote sensing instrument. If contributions of the three terms are added, simple retrieval given in Equation (2-4) becomes as [16][19]:

$$L(\lambda, \mu) = t_1(\lambda, \mu)\varepsilon B(\lambda, T_s) + L_a(\lambda, \mu) + L_s(\lambda, \mu, \mu_0, \phi_0)$$

$$+ t_2(\lambda, \mu, \mu_0)\mu_0 E_0(\lambda) f(\mu; \mu_0, \phi_0) +$$

$$\qquad \text{(2-13)}$$

$$\int_0^{2\pi}\int_0^1 \mu' f(\mu; \mu', \phi')[t_3(\lambda, \mu)L_d(\lambda, -\mu', \phi') + t_4(\lambda, \mu)L_t(\lambda, -\mu', \phi')]d\mu' d\phi'$$

To simplify Equation (2-13), following three assumptions can be made about the surface properties [16][19].

- Unless rain and/or snow occurs during the short period of time, particularly for bare soils in arid and semi arid environments, ε does not change, but it varies with vegetation coverage and surface moisture content.

- In the 3.66-4.20 µm range, there are quite strong spectral variations in surface reflectance for most terrestrial materials. However, their BRDF anisotropic factor has very small variations (~2%). As a result, single BRDF anisotropic factor can be used for surface reflected direct solar beam for these bands.

- In LWIR and MWIR range, atmospheric radiative transfer simulations prove that surface reflected diffuse solar irradiance (L_d) is much smaller than surface reflected direct solar beam term (E_0) and surface reflected atmospheric downward thermal irradiance term (L_t) is smaller than surface thermal emission ($L_{emitted}$). Therefore, Lambertian assumption for surface reflectance does not introduce significant errors. As a result, $f_r(\mu, \mu', \Phi')$ can be written as Lambertian BRDF from the Equation (2-10) and can be used in ε expression, given in the Equation (2-3).

After these assumptions, radiance measured in band j can be written as in Equation (2-14) [16][19].

$$L(j) = t_1(j)\varepsilon(j)B_j(T_s) + L_a(j) + L_s(j) + \frac{1-\varepsilon(j)}{\pi}[t_2(j)\alpha_r\mu_0 E_0(j) + t_3(j)E_d(j) + t_4(j)E_t(j)] \qquad \textbf{(2-14)}$$

In this equation, all the terms are band averaged, E_d is solar diffuse irradiance, and E_t is atmospheric thermal irradiance. ε, α_r, and B_j depend on the surface properties and conditions. All other terms, which can be given by numerical simulations of atmospheric radiative transfer, depend on

atmospheric water vapor and temperature profiles and solar and viewing angle effects [16][19].

2.2.5 Solution of the retrieval equation

Three methods have been proposed to solve the Equation (2-14) for land surface temperature (LST) [16][19]:

- **Single IR channel method:** It requires surface ε, accurate radiative transfer model, and atmospheric profiles.

- **Split window method:** From differential absorption in adjacent IR bands, corrections are made for the atmospheric and surface ε effects; it requires surface ε as an input.

- **Day/Night MODIS LST method:** Day/night pairs of TIR data in seven MODIS bands are used for simultaneous determination of surface temperatures and emissivities without knowing atmospheric temperature and water vapor profiles at high accuracies.

Although, the first two methods require ε knowledge with high accuracy, it is almost impossible to estimate band averaged emissivities to such accuracy for regions with variable emissivities [16][19]. After comprehensive numerical simulations and analysis, two LST algorithms are implemented for MODIS products, the generalized split window and the day/night LST and ε algorithm. The last the algorithm is used in the ε database in our study and will be explained briefly in the following section.

2.2.6 MODIS day/night LST and ε algorithm

To retrieve LST and ε at an acceptable accuracy, it is necessary to use multi-temporal and multi-channel data by considering atmospheric conditions [19]. For any location of the Earth's land surface, MODIS data from EOS AM (day) and PM (night) platforms are retrieved up to four times a day providing LST diurnal change observations [24]. In this model, daytime data in the 3.66-4.20 μm range, where MODIS bands 20, 22, and 23 are located, enables the solar radiation to be used as thermal IR source for obtaining the surface reflectance [6]. Thus, LST and ε can be simultaneously retrieved by combining nighttime data in these three bands and day/night data in the other four bands (bands 29, 31, 32, and 33) in LWIR [6][16][19].

In this algorithm, there are 2N observations due to day and night measurements in N MODIS TIR bands. N band emissivities, daytime and night time surface temperatures (T_{s-day} and $T_{s-night}$), two water vapor profiles (column water vapor, cwv), two air temperature profiles (T_a), and the anisotropic factor (α) are total number of unknown variables (N+7) [16][19] [31]. To solve the Equation (2-14), it is known that number of observations (2N) should be greater than or equal to the number of unknowns (N+7), i.e. N ≥ 7, so that seven MODIS bands 20, 22, 23, 29, 31, 32 and 33 in TIR are used in the algorithm [16][19]. As a result, the set of 14 nonlinear equations are solved in this algorithm.

To solve these equations, method based on look up tables (LUTs) is used for calculating atmospheric and solar terms in Equation (2-14) and these LUTs are developed from complete series of radiative transfer simulations [19]. Atmospheric temperatures and water vapor profiles are the most important atmospheric variables in thermal IR, for this reason column water vapor (cwv) and air temperatures (T_a) are obtained from MODIS product of atmospheric temperature and water vapor profiles. To solve the final

retrieval equation, initial values of the variables are provided by LUTs and other MODIS data products. Consequently, uncertainties due to initial atmospheric conditions are reduced and better self consistent solution for LST and ε is provided [16][19][24].

2.2.6.1 Emissivity determination

MODIS day/night algorithm can retrieve ε in bands 20, 22, 23, and 29 [6]. Band averaged emissivities are used for ε in bands 31 and 32 (in the 10.780-11.280 μm and 11.770-12.270 μm intervals) because these bands are at the maximum of emission for targets at ambient temperature [19][25]-[27]. Therefore, the emissivities of land cover types are relatively stable and known within approximately 0.01 in this range [19][25]-[27]. These band averaged emissivities ($\bar{\varepsilon}(j)$) calculated from the published spectral reflectance data of 80 terrestrial samples of Salisbury and D'Aria as given in Equation (2-15) and Equation (2-16) [25][26].

$$\bar{\varepsilon}(j) = \frac{\int_{\lambda_{j,L}}^{\lambda_{j,U}} \psi(\lambda)\varepsilon(\lambda)B(\lambda,T)d\lambda}{\int_{\lambda_{j,L}}^{\lambda_{j,U}} \psi(\lambda)B(\lambda,T)d\lambda} \qquad (2\text{-}15)$$

$$\bar{\varepsilon}(j) = \frac{\int_{\lambda_{j,L}}^{\lambda_{j,U}} \psi(\lambda)\varepsilon(\lambda)d\lambda}{\int_{\lambda_{j,L}}^{\lambda_{j,U}} \psi(\lambda)d\lambda} \qquad (2\text{-}16)$$

In Equation (2-15), Ψ is the response function of the spectral band j, which is shown in Figure 2-2 with lower ($\lambda_{j,L}$) and upper boundaries ($\lambda_{j,U}$) [16][19][24]. $\bar{\varepsilon}(j)$ is written in Equation (2-16) independent of surface temperature because temperature dependence is usually very small in the Earth surface environment [16][19].

Table 2-3 shows ε values for bands 31 and 32 used in the algorithm for different land cover types with small modifications. Approximately averaged ε values are used for broadleaf forest, woody savanna, grass savannas, and shrubs in their seasonal cycles from green to senescent because greenness change and its impact on the ε at a pixel scale are not easy to detect in these two bands [6].

Table 2-3 ε values in bands 31 and 32 and in the last two columns show the root-mean-square (rms) values of their mean and difference used in the MODIS algorithm [6].

Description of landcover (type #)	ε_{31}	ε_{32}	rms m_em	rms d_em
Water (0)	0.992	0.988	0.0049	0.0024
Evergreen needleleaf forest (1)	0.987	0.989	0.0029	0.0005
Evergreen broadleaf forest (2)	0.981	0.984	0.0035	0.0015
Deciduous needleleaf forest (3)	0.987	0.989	0.0029	0.0005
Deciduous broadleaf forest (4)	0.981	0.984	0.0035	0.0015
Mixed forest (5)	0.981	0.984	0.0035	0.0015
Closed shrublands (6)	0.983	0.987	0.0034	0.0014
Open shrublands (7)	0.972	0.976	0.0134	0.0042
Woody savannas (8)	0.982	0.985	0.0039	0.0013
Savannas (9)	0.983	0.987	0.0034	0.0014
Grasslands (10)	0.983	0.987	0.0034	0.0014
Permanent wetlands (11)	0.992	0.988	0.0049	0.0024
Croplands (12)	0.983	0.987	0.0034	0.0014
Urban and built-up (13)	0.970	0.976	0.0139	0.0074
Cropland and mosaics (14)	0.983	0.987	0.0034	0.0014
Snow and ice (15)	0.993	0.990	0.0023	0.0006
Bare soil and rocks (16)	0.965	0.972	0.0074	0.0032
Unclassified (17)	0.978	0.981	0.0085	0.0034

2.2.7 MODIS data accuracy and validation

MODIS database is validated in multiple validation sites in relatively wide ranges of surface and atmospheric conditions by aircraft and satellite data and field measurements [16][24]. Temporal and spatial validations have

been made by field measurements, MAS (MODIS Airborne Simulator) and TIMS (Thermal Imaging Multispectral Spectrometer) data [16]. It is found that standard deviations of errors are in between 0.005-0.008 for bands 20, 22, 23, 29, and 31-32 in retrieved emissivities and it is 0.012 for the last band 33 because of the low transmission of this band in the atmospheric condition [16].

Figure 2-6 shows that spatial ε variations based on ASTER and MODIS observations ranges from 0.84 to 0.96 in Sahara Desert in the 8–12 µm window [8].
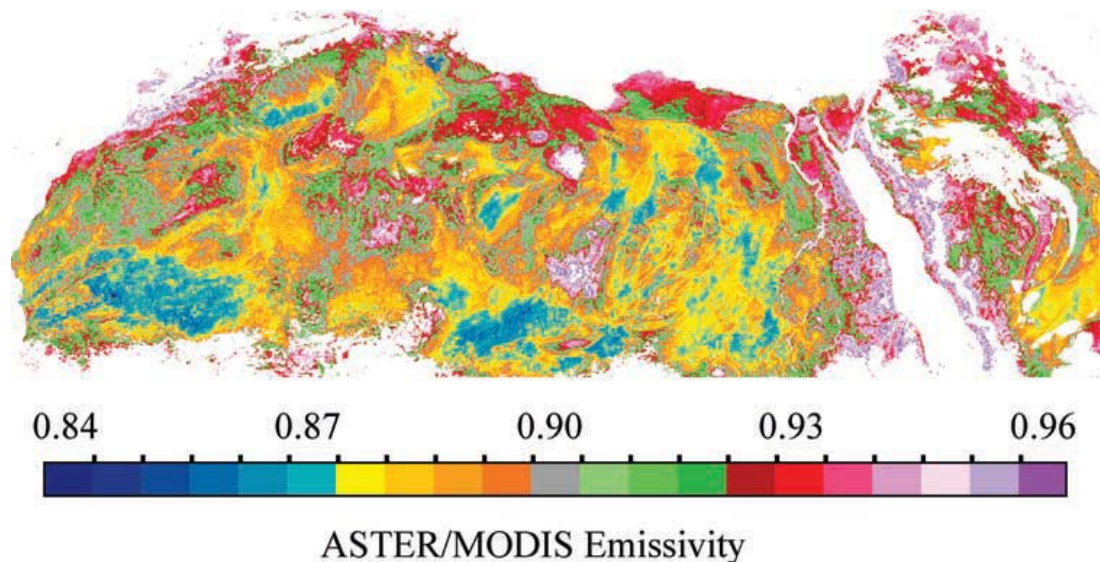
Figure 2-6 Spatial variations of ε in the 8–12 µm interval over the Sahara desert and Arabian Peninsula [8].

As shown in the figure, ε shows significant spatial variability [8]. In addition to spatial variations, seasonal and spectral ε variations are important in ε determination, which will be discussed in the next chapter.

CHAPTER 3

EMISSIVITY VARIATIONS

The IR radiation from a natural opaque surface originates within a fraction of a millimeter of the surface; therefore, ε is a strong function of the surface state and/or cover [9]. Emissivity, which is a dynamic parameter, shows significant spatial, temporal, and spectral variations. To understand and interpret emissivity variations, a detailed literature survey on ε variations is necessary. According to literature survey done, these variations are investigated mainly in two groups: variations due to land cover type and seasonal effects.

3.1 Land Cover Type Dependent Emissivity Variations

Different land cover types reveal different ε characteristics. An ε look up table (LUT) at four wavelengths for 19 International Geosphere Biosphere Programme (IGBP) classes, which is the most common worldwide land cover type classification, is given in Table 3-1 [27]. Table 3-1 shows that highest ε variations among all land cover types are observed particularly for the 3.7 μm and 8.5 μm bands. The highest ε variations are observed between the vegetated and barren-sparsely vegetated areas among all land cover types (excluding water and snow/ice).

Table 3-1 Emissivity LUT for the IGBP surface types [27].

IGBP class	IGBP type	3.7 µm ε	8.5 µm ε	10.8 µm ε	12 µm ε
1	Evergreen needleaf	0.9647	0.9589	0.9894	0.9902
2	Evergreen broadleaf	0.9329	0.9596	0.9742	0.9731
3	Deciduous needleaf	0.9685	0.9658	0.9924	0.9960
4	Deciduous broadleaf	0.9440	0.9596	0.9811	0.9818
5	Mixed forests	0.9638	0.9571	0.9887	0.9913
6	Closed shrublands	0.9390	0.9416	0.9833	0.9849
7	Open shrubland	0.8503	0.8899	0.9572	0.9688
8	Woody savannas	0.9369	0.9474	0.9801	0.9830
9	Savannas	0.9014	0.9263	0.9657	0.9701
10	Grasslands	0.8910	0.9338	0.9690	0.9748
11	Permanent wetlands	0.9758	0.9656	0.9955	0.9973
12	Croplands	0.9193	0.9417	0.9725	0.9758
13	Urban	0.9264	0.9436	0.9757	0.9748
14	Mosaic	0.9261	0.9484	0.9760	0.9781
15	Snow/ice	0.9718	0.9715	0.9946	0.9909
16	Barren-sparsely vegetated	0.7692	0.7806	0.9368	0.9639
17	Water	0.9637	0.9967	0.9775	0.9431
18	Tundra	0.9671	0.9615	0.9931	0.9881
19	Coastline	0.9533	0.9571	0.9849	0.9823

Figure 3-1, shows a global ε map, which is obtained by applying different algorithms to MODIS ε data for all IGBP surface types, in the 3.7 µm in April 2001 [27]. As seen in the figure, the densely vegetated areas have ε values greater than 0.925 while intermediate values are found for less vegetated regions.
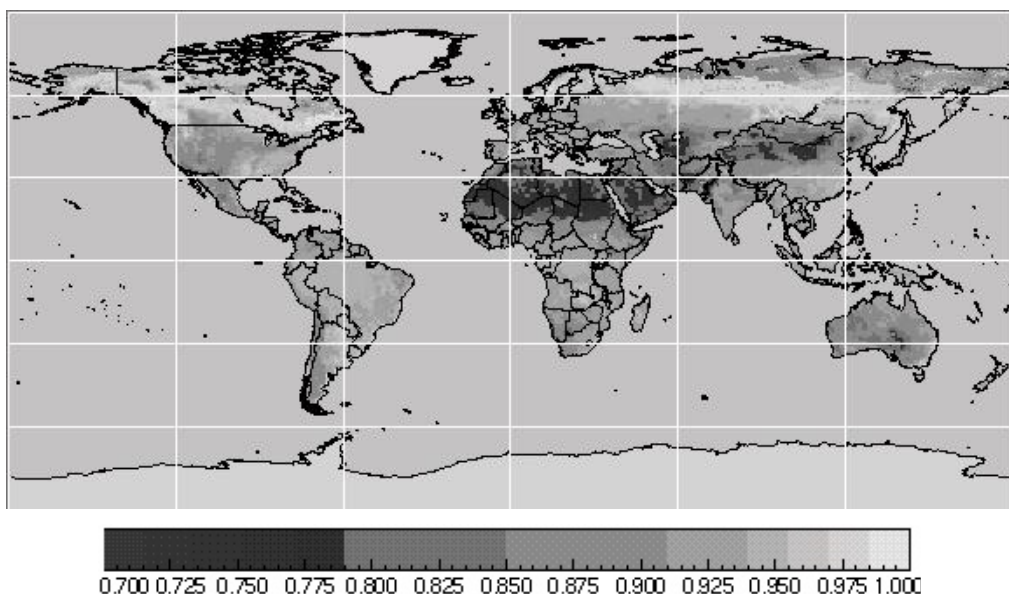
Figure 3-1 Mean MODIS ε data for the 3.7 µm in April 2001 [27].

22

As a result, we can conclude that densely vegetated areas have ε values greater than less vegetated regions (barren-sparsely vegetated and savannas etc.) both in LWIR and MWIR, however difference between ε values of less and densely vegetated regions are higher in MWIR when compared to LWIR. Difference between vegetated and non-vegetated areas can be examined from MODIS ε values as shown in Figure 3-2 [9].
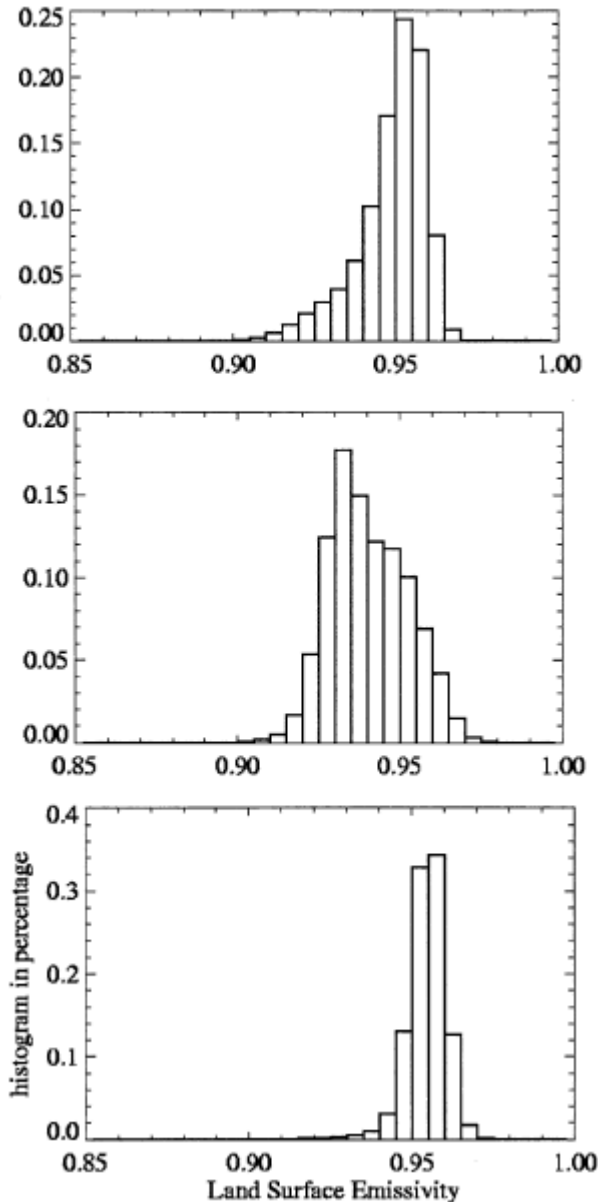
Figure 3-2 MODIS ε values in April for the different land cover types: grassland (upper), barren-sparsely vegetated (middle), and forest (lower) [9].

In Figure 3-2, barren sparsely vegetated region has significant variations in the ε, ranging from 0.87 to 0.97 because of the underlying soil conditions. For mixed forest, the range of ε is between 0.93 and 0.97 and it is much more moderate than that of bare soil because forest dominates underlying soil spectrum. Figure 3-3 shows the spectral reflectance values for five soil samples, one of which is vegetated [22].
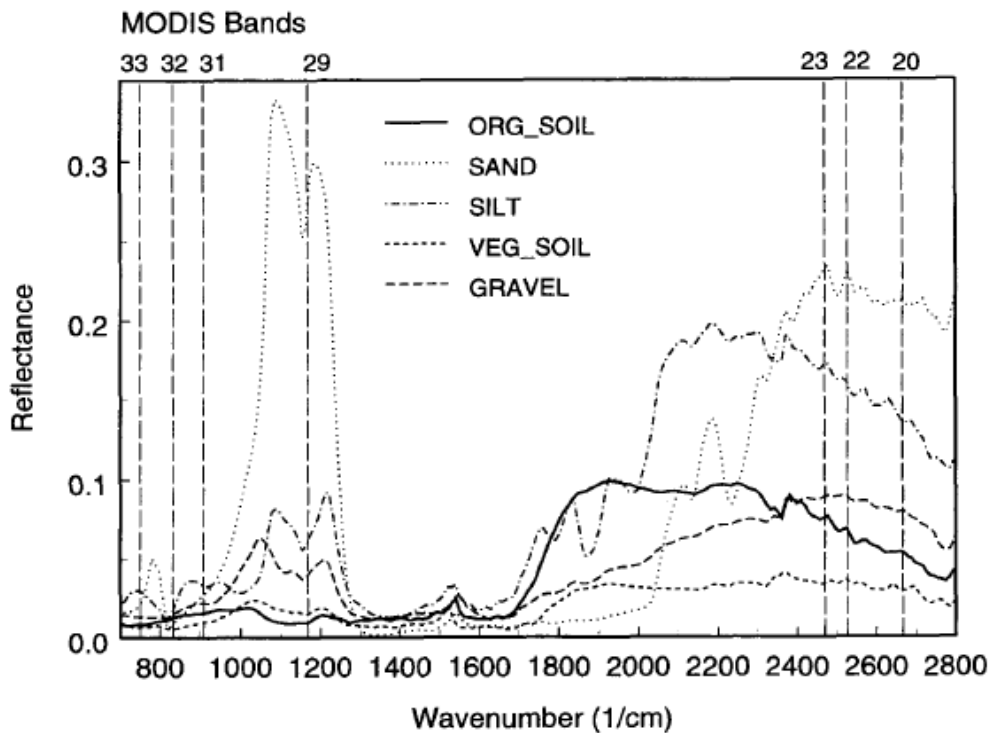
Figure 3-3 BRDF measurement spectra of five samples (organic soil, sand, silt, vegetated soil, and gravel) [41].

Different features of the ε spectra are observed between vegetated soil and non-vegetated samples. Land cover type dependent variations occur mainly due to the two factors: non-vegetated and vegetated. For this reason soil and vegetation spectra properties will be studied in more detail in the following subsections.

3.1.1 Soil emissivity spectra properties

Emissivity of soil depends on the soil composition and moisture content [9]. Figure 3-4 shows ε spectra of soils in MWIR and LWIR, which are classified into totally five soil spectra types from the laboratory measurements of thirty natural soil samples [31][33].
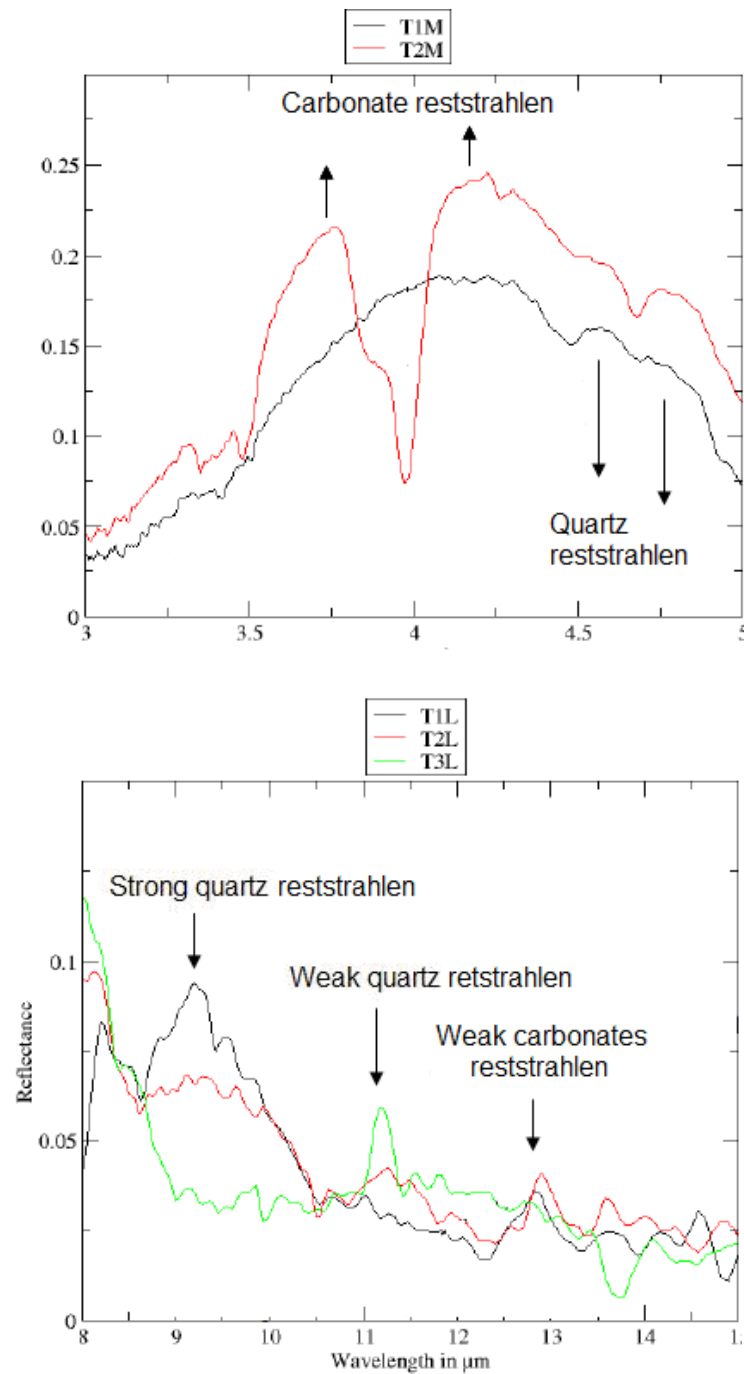
Figure 3-4 Soil spectra behavior of dry samples: in MWIR (top), in LWIR (bottom) [33].

In Figure 3-4, minimum emissivities (maximum reflectance values) are observed due to reststrahlen bands. As shown in Figure 3-4 (top), spectra bell-shaped (T1M) and spectra with two lobes (T2M) are the two types of soil spectra in MWIR. Figure 3-4 (bottom) shows the three types of soil reflectance spectra in LWIR. The first one (T1L) has strong and weak reststrahlen bands of quartz, second one is (T2L) spectra with strong reststrahlen bands of carbonates, which does not appear in the figure, and plus T1L, and the third one (T3L) is spectra with weak reststrahlen bands of carbonates [33].

Reststrahlen bands or the fundamental molecular vibration bands reflect most where they emit least [2][25][26]. Presence of quartz (SiO_2) and carbonates (CO_3) are the primary causes of the reststrahlen bands in soils [25][26]. Firstly, quartz is a common mineral and major component in soils and its reststrahlen bands dominate soil spectra behavior in LWIR when compared to that in MWIR [25][26]. In LWIR, strong and weak quartz reststrahlen occur in the 8-10 µm and 12.2-13.0 µm, respectively and maximum ε in soils is found mostly near the 12.2 µm [25][26]. Much weaker quartz bands exist near the 4.5 µm and 4.7 µm in MWIR [25][26]. Secondly, carbonate reststrahlen band is between 6 and 8 µm and secondary band can exist near the 11.3 µm in LWIR [17]. In MWIR, strongest carbonate doublet is near the 4 µm and carbonate bands are more important than quartz bands in MWIR [26][30].

3.1.2 Vegetation emissivity spectra properties

Vegetation can cover a large surface densely, which may result in masking of the soil spectral signature. Generally higher ε values are observed for vegetation when compared to barren/sparsely vegetated regions, as discussed previously (see Table 3-1 and Figure 3-1).

Emissivity of a canopy is even more complex than that of soil because it is affected by plant species, growth stage, proportion of vegetation, and underlying soil. Canopy geometry structure causes multiple internal reflections called cavity effect, because three dimensional structures of plant canopies tends to act as blackbody cavities due to internal scattering [9][34]. The cavity effect causes larger ε of a canopy when compared to the ε of single leaf and bare soil [9][34]. Maximum ε in a vegetation signature is generally observed near 12.4 μm for green foliage, near 8.5 μm for senescent leaves and bark, and near 10.1 μm for rock lichens [25]. However, this value will decrease as the vegetation becomes sparse and the soil contributes to the emittance.

3.2 Temporal Emissivity Variations

Temporal (seasonal/monthly) ε variations occur due to the seasonal effects. Precipitation amount and type (snow and rain), drought, vegetation greenness, proportion of vegetation, and the growth stage of vegetation can cause significant temporal variations on the ε. Precipitation and vegetation greenness change are the two factors causing temporal ε variations.

3.2.1 Precipitation

Precipitation causes seasonal ε variations in the form of snow and rainfall depending on the season. Due to seasonal variations, the annual periodicity of precipitation is expected to cause annual periodic ε values, which is considered in our study.

Snow causes significant temporal ε variations. It can cover whole surface. Figure 3-5 shows spectral ε of a snow-ice sample [9][40].
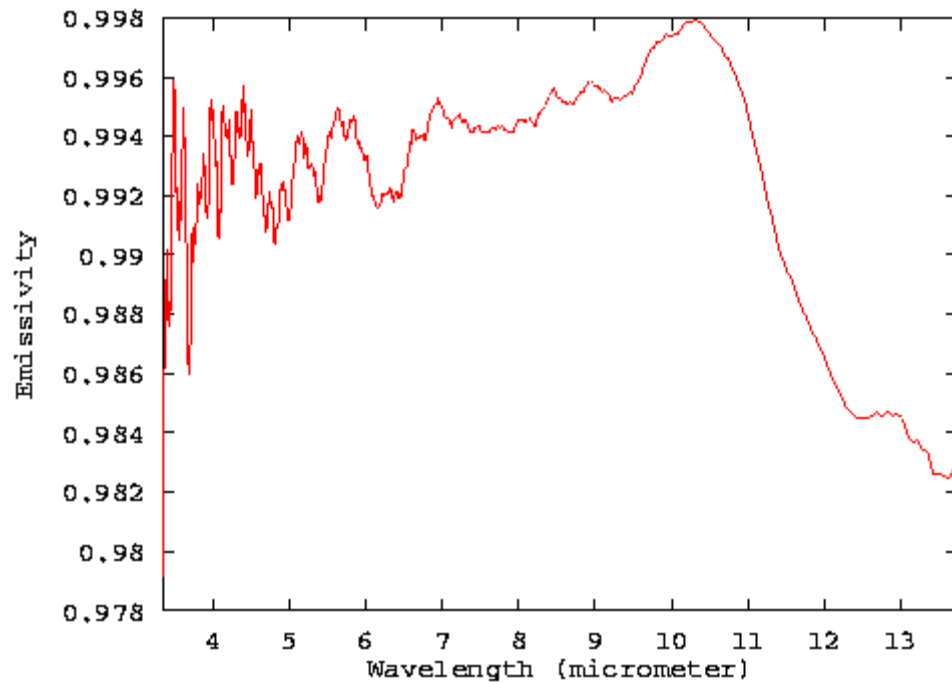
Figure 3-5 Ice-snow sample spectral ε [9][40].

As shown in Figure 3-5, snow-ice ε has an overall value of 0.99 in the 4-10 μm interval. ε increases with snow cover in winter season because snow cover hinders and dominates the underlying surface ε. The influence of snow is expected to be dominant particularly for barren-sparsely vegetated regions because these regions do not have any vegetation cover which decreases the effect of snow.

Rainfall is other form of precipitation causing temporal ε variations. Rainfall affects ε by increasing soil moisture (SM). Figure 3-6 shows the comparison between temporal variations of the measured SM values from Advanced Microwave Scanning Radiometer AMSR-E sensor on satellite and rainfall estimates during April 2006 [31].
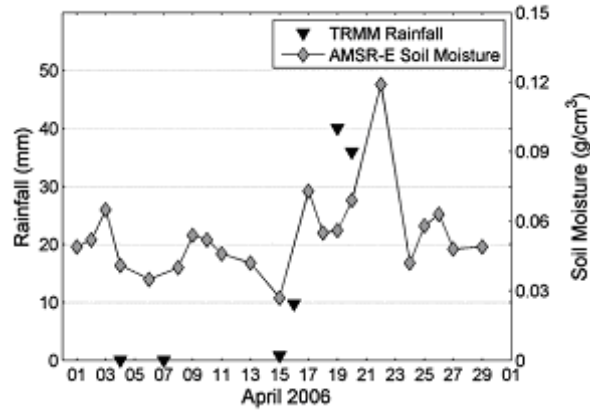
Figure 3-6 Rainfall estimates and SM values [31].

As shown in Figure 3-6, rainfall estimates and SM are correlated. SM values increase only one day after the rainfall and rainfall directly increases SM. All other forms of precipitation (snowfall, snowmelt and watering) can also increase SM. Influence of SM on ε is discussed in the next part.

3.2.1.1 Soil moisture

SM is basically due to water content of the soil. It should be considered in ε studies because its variation can cause high ε fluctuations. Few studies in IR are published in IR concerning SM effect on ε, where different approaches are used to model this dependency [31]-[37]. From the results of these studies, it can be concluded that ε increases with SM especially for sandy soils. SM depends on soil composition and field capacity (FC) of the soil.

ε values increase with SM in different wavelength intervals depending on the soil composition (quartz, carbonate, and organic matter content). Figure 3-7 shows ε comparison between wet and dry soil samples [31].
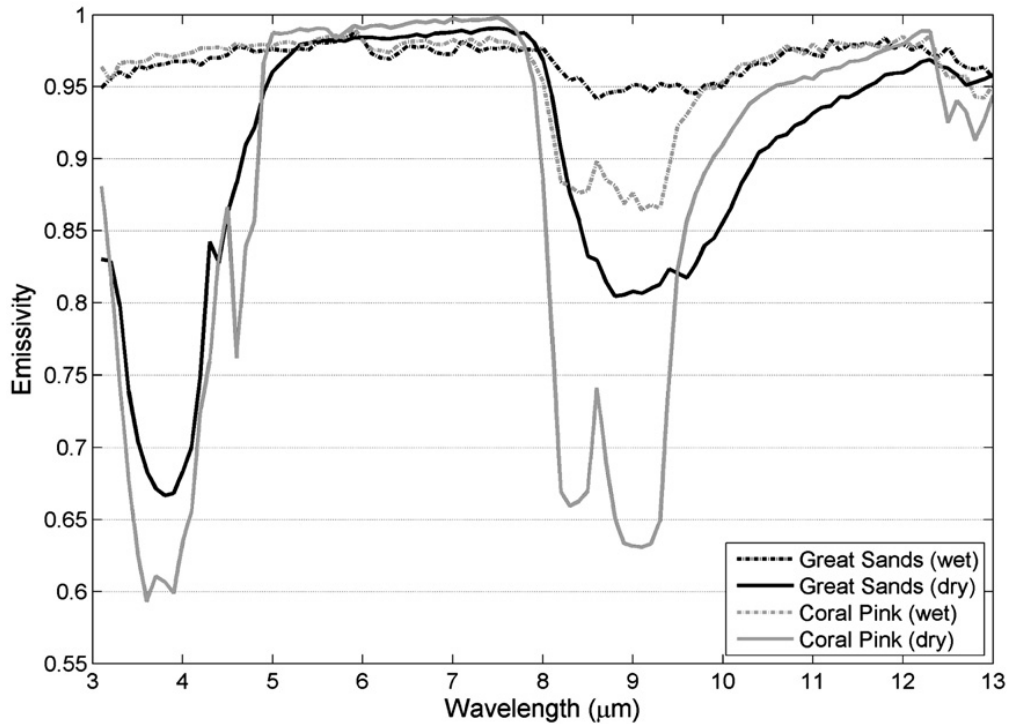
Figure 3-7 Laboratory ε spectra for a wet and dry (dashed and solid lines, respectively) two different samples [31].

In Figure 3-7, ε spectra for wet samples are higher and spectrally flat in the 3-5 μm interval when compared to dry samples [31]. Moreover, two characteristic quartz doublets are present in Figure 3-7 for Coral Pink (CP) sand sample between the 8.0-9.5 μm and 12-13 μm intervals due to quartz abundance in CP sample [31]. On the other hand, Great Sands (GS) sample has less spectral variations in these intervals due to less quartz presence [31]. In quartz reststrahlen bands, emissivities of both wet samples are 10-15% higher and their spectral contrasts are lower when compared to those for drier ones [31]. Figure 3-8 shows spectral reflectance curves of two different samples with respect to different SMCs [32][33].
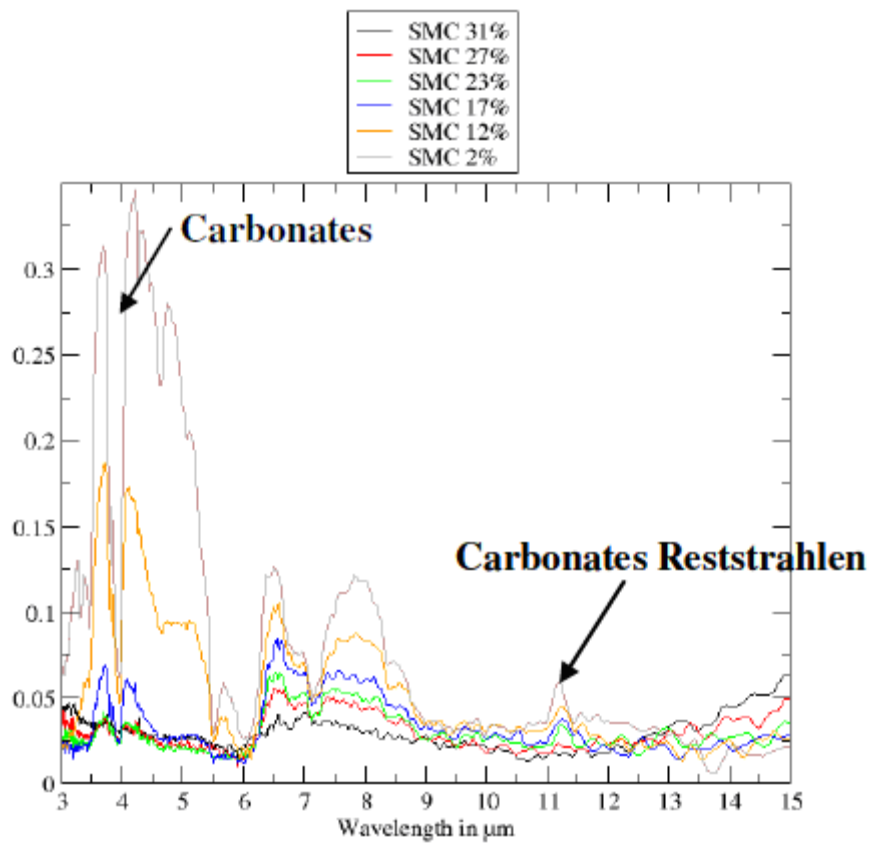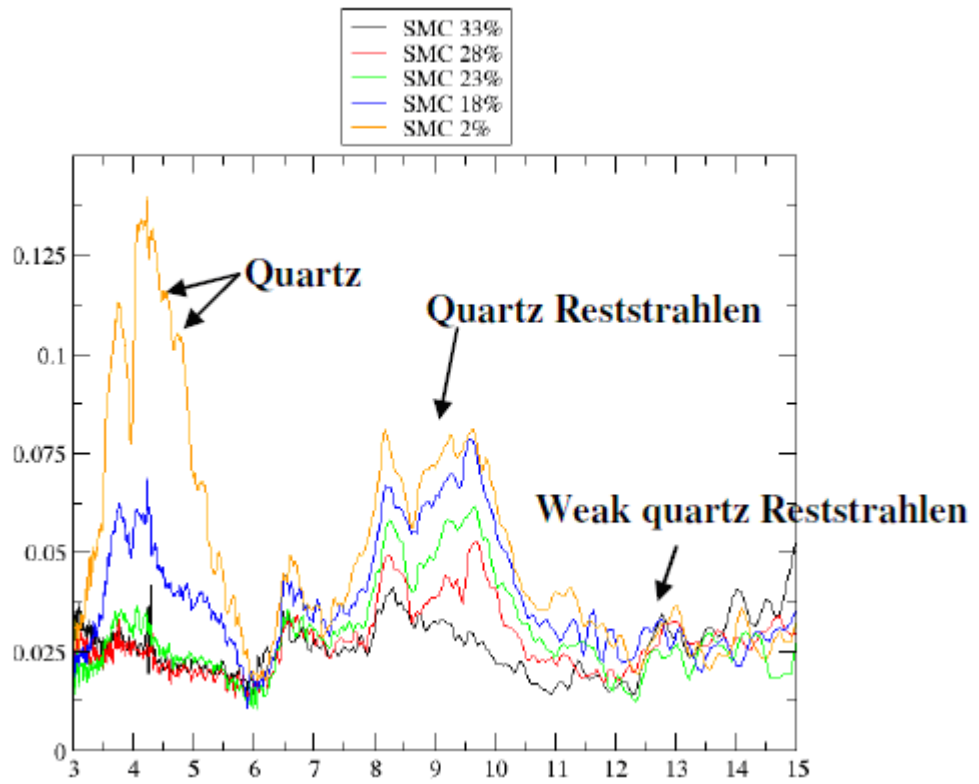
Figure 3-8 Spectral reflectance at different SMC for two samples having different compositions: quartz (upper) and carbonates (lower) [32][33].

As shown in Figure 3-8, in reststrahlen bands, water absorption occurs resulting in decrease in reflectance (increase in ε) with the increase in SMC. In the remaining wavelength intervals, less ε variation (0-3%) with SMC is found for both samples. Strong water absorption (sharp decrease in reflectance with increase in SMC) occurs in quartz reststrahlen bands for the first sample in Figure 3-8 (topom) due to its quartz abundance. Similarly, for the second sample in Figure 3-8 (bott) it occurs in carbonates reststrahlen bands due to its carbonate abundance. Maximum ε values are observed for both samples near the 12 μm independent of the SMC and composition of the soil [32][33].

In addition to the soil composition, SM impact on ε depends on FC, which is water content held in soil after excess water has drained away [34][[35]. For example, Figure 3-8 shows that peak detection is almost impossible if SMC is above 20%, i.e. when FC of soil is exceeded [32][33]. Figure 3-9 shows change in ε values for six samples with respect to SMC in different wavelength intervals [34].

As shown in Figure 3-9, the dependency of ε on the SM is negligible in high water contents, i.e. water contents higher than FC. On the other hand, no changes are observed for moisture level above a certain SM value due to FC [34]. It is concluded that in the case where SMC is higher than FC value of the soil, emissivities are close to 1.0 due to water, which is retained in the soil macropores [34][35]. If FC value is not exceeded water is retained in micropores and macropores are full of air, therefore ε values are lower and have considerable variations with respect to SMC and wavelength interval [34][35].
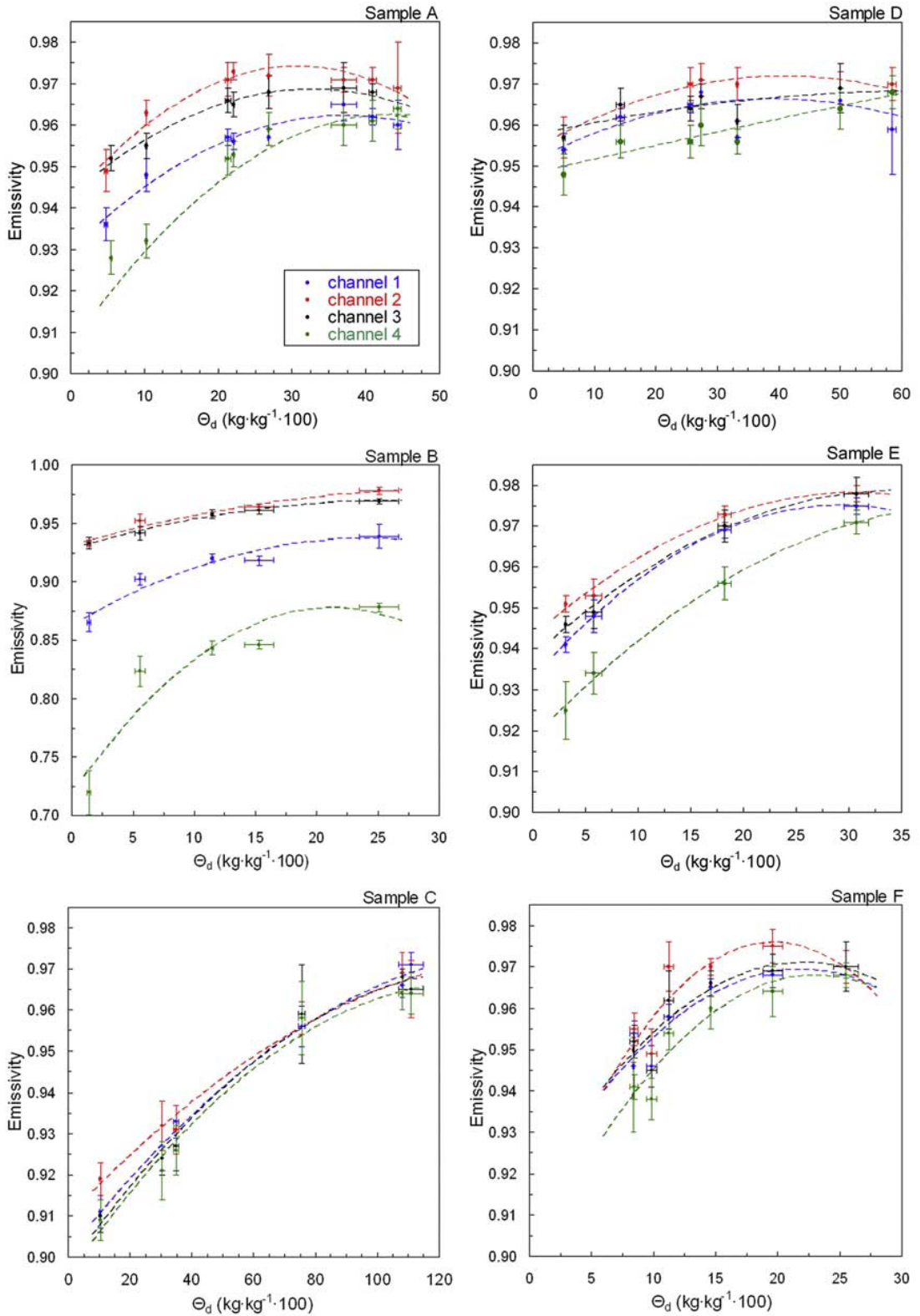
Figure 3-9 Measured spectral ε values versus soil water content θ_d (kg.kg^{-1}.100) for six soil samples. (channels 1, 2, 3, and 4 represent 8-14 μm, 11.5-12.5 μm, 10.5-11.5 μm, and 8.2-9.2 μm respectively.) [34].

3.2.1.2 SM effect on MODIS derived emissivities

It is observed that monthly ε values for MODIS band 29 (in the 8.400-8.700 µm interval) are increased by about 0.1 in each July/August in the Southwestern Sahara [36][37]. This ε variation is compared with MODIS Normalized Difference Vegetation Index (NDVI) data, which shows the presence of vegetation and SM values derived both from AMSR-E and ground measurements [36][37]. As a result, it is found that ε increase is highly correlated with the increase in SM and no correspondence is found with the NDVI [36][37]. Therefore, MODIS band 29 is expected to be sensitive to the changes in SM because water is strongly absorbing in the quartz reststrahlen band (8-10 µm) as discussed previously [31].

It is also found that ε values in MODIS bands 31 and 32 (in the 10.780-11.280 µm and 11.770-12.270 µm intervals) are nearly constant and stable independent from the season and SM [31]. Because MODIS ε retrieval algorithm fixes ε values in these bands depending on the land cover type, which is discussed in the Section 2.2.6.1. [12][38].

As shown in Figure 3-8, although SM is also effective on ε values in MWIR, we could not find any study investigating SM influence on ε in MODIS MWIR bands (bands 20, 22, and 23). It should be noted that in our seasonal ε variation studies, all six MODIS IR bands (including MWIR bands) are considered.

3.2.2 Vegetation greenness change

Vegetation greenness and type, growth stage, and proportion of vegetation are the main factors leading to the seasonal ε changes, as stated previously. Temporal changes on vegetation differ for vegetation types: conifers are

evergreen forests and on the other hand, deciduous forests lose their leaves temporally. Conifers are expected to retain their ε values at all seasons, because they are not affected too much from seasonal changes [25]. On the other hand, for grassland surfaces and temporally affected forest types, season effect should be taken into consideration [25]. For example, maximum emissivity is observed near the 12.4 μm (band 32) for the green foliage and lower ε is observed in the 4.0-5.5 μm region for the dry plant material [25][26][34]. However, it should be considered that at a pixel scale vegetation greenness change and its impact on ε can be difficult to detect [6].

According to the literature survey on ε variations, we found that land cover type and time (season and month) are the two main parameters, which affect spectral ε variations dominantly. Precipitation has also a great influence on ε and causes seasonal variations of ε. By means of the results of literature survey, our ε variation studies for the specific regions in Turkey are introduced in the next chapter.

CHAPTER 4

EMISSIVITY VARIATIONS FOR THE SELECTED REGIONS IN TURKEY

In the previous chapter, the detailed literature survey on ε reveals that ε shows significant spectral variations depending on the land cover type (soil and vegetation) and precipitation. However, these emissivity analyses are done for many critical regions (Europe, Iran, Morocco, Sahara Desert, Northern Africa and the Arabian Peninsula) except Turkey [5][8][11][12]. Determination of the ε values for the selected regions in Turkey and investigation of their variations with respect to land cover type, IR wavelength, and time (season and month) are our main goals in this study. The results of this study are to be used in many critical applications for Turkey, which is our main motivation.

We selected seven regions from Anatolia, which have different land cover types and precipitation properties, to determine land surface ε values and investigate their variations. For the selected regions, land surface ε values are obtained from monthly MODIS land surface ε database for four years in six different IR bands. We developed an interface to study spectral ε variations with respect to monthly, seasonal, and yearly changes for the selected regions. In addition, precipitation dataset, obtained from the Turkish State Meteorological Services for these regions, is used to investigate the dependence of the ε on the precipitation. In this chapter, ε dataset and selected regions are briefly explained and the related work is presented.

4.1 Emissivity Dataset and IR Land Surface Emissivity Analyses (IR-LSEMA)

For the study of the temporal and spectral ε values at different IR wavelengths for any location in Turkey, we used global MOD11C3 Land Surface Temperature and Emissivity dataset of MODIS, whose specifications and ε determination algorithms are explained previously. This dataset is widely used in ε determination studies in the literature because standard deviations of MODIS ε errors change between 0.005-0.008 for all spectral bands [16]. It is composed of monthly ε values for six spectral bands and different years in any location in the world. We used the four year ε dataset from 2005 to 2008 to study monthly and yearly ε variations.

Our emissivity database is composed of 288 ε matrices (6*12*4) for six spectral bands (band 20, 22, 23, 29, 31, and 32) for every month of the four year. Each ε matrix has a dimension of 3600x7200, which provides global coverage of the world. We found that only 501x501 part of this ε matrix encloses the whole Turkey with its neighbors as shown in Figure 4-1. We converted each element in this 501x501 sub-matrix to the corresponding coordinate information (latitude/longitude) to obtain ε values of a selected region from its coordinate information.
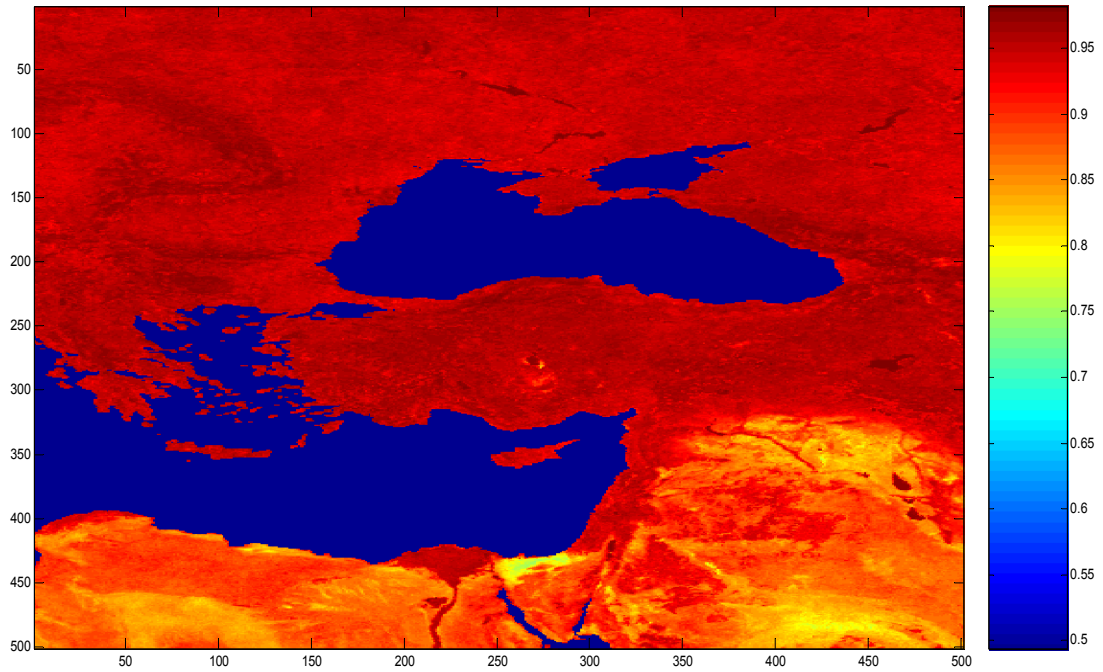
Figure 4-1 Image of the 501x501 part of the MODIS ε matrix for band 20 in August 2007, which covers the whole Turkey.

A single matrix element encloses an area of 31.36 km^2 because MODIS spatial resolution is 5.6 km. This matrix element gives ε value of the center of this area for a month of a year at the desired spectral band. However, major land cover type distribution cannot be homogenous in the pixel area. Therefore, an averaged ε value including neighboring pixel emissivities are assigned for the ε value of that region. For this reason, average emissivities of four pixels, which enclose approximately an area of 123.6 km^2, are computed using Equation (4-1), as shown in Figure 4-2.
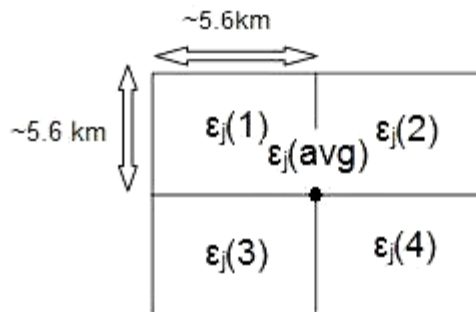
Figure 4-2 Averaging of four neighboring pixels for emissivity determination.

38

$$\varepsilon_j(avg) = \frac{\varepsilon_j(1) + \varepsilon_j(2) + \varepsilon_j(3) + \varepsilon_j(4)}{4} \qquad \text{for any band j (j=1,2,....6)}$$

$$\varepsilon_j = \varepsilon_j(avg)$$

(4-1)

This averaged ε value (ε$_j$(avg)) is the ε value (ε$_j$) for the selected region. We developed an interface with MatlabGUI to calculate ε$_j$ values for any selected region and study their variations. It is called as IR-LSEMA and shown in Figure 4-3.
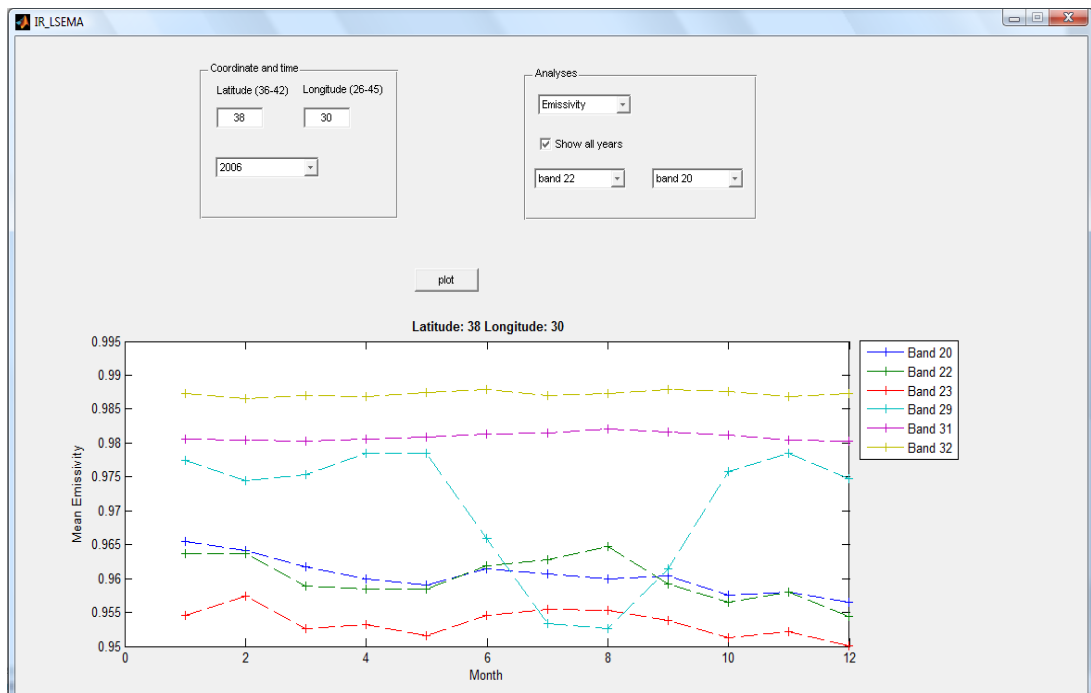
Figure 4-3 IR-LSEMA interface.

In the following section, ε variation studies performed by using IR-LSEMA are explained in detail.

4.2 Determination of Emissivity and Its Variations for the Selected Regions in Turkey

We chose seven different widely known regions in Turkey in order to examine ε variations with respect to precipitation and land cover types. In the selection of these regions we considered the diversity of the land cover types and climates in Turkey, which is shown in Figure 4-4. These regions in the figure are selected from the different parts of Anatolia according to their different land cover types and precipitation properties i.e. rain, snow, and drought.

One of the regions is the Salt Lake, which is used for calibration purposes. Other regions have three main land cover types (forest, cropland, and barren/sparsely vegetated). For a fair comparison of the emissivity studies, two different regions having similar land cover properties are considered. The regions are; Kastamonu-Küre (forest), Antalya (forest), Adana-Çukurova (cropland), Şanlıurfa-Harran (cropland), Konya (barren-sparsely vegetated), and Antalya-TUG (barren-sparsely vegetated).

We determined the coordinates of the selected regions from the Google Earth views and also confirmed the land cover type information of these regions from these views [44]. Monthly ε_j values of these regions are obtained from IR-LSEMA using the determined coordinates of the regions. We used long years (1975-2008) average monthly precipitation amount of five cities (Antalya, Adana, Konya, Şanlıurfa, and Kastamonu) to examine the correlation between ε_j variations and precipitation [45]. Only one year (2006) monthly precipitation amount is used for the Salt Lake due to lack of the data for this region [43]. In the following subsections, we performed a detailed investigation of monthly and spectral ε variations for each region using precipitation and ε_j values.
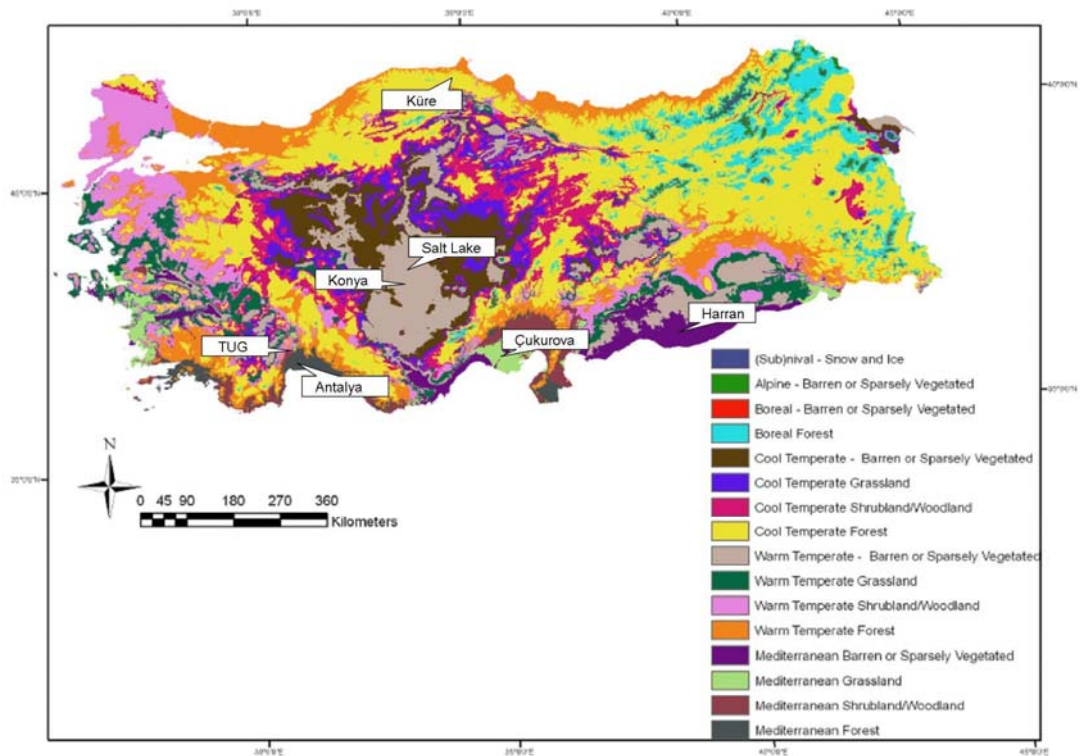
Figure 4-4 Spatial distribution of land cover types and climate groups and selected regions in Turkey [42].

4.2.1 Salt Lake

Salt Lake, shown in Figure 4-5 is used as a calibration region in our study to investigate ε variations where no vegetation and low precipitation present. It is commonly chosen as a radiometric calibration side in many geological and remote sensing applications due to the following reasons [43]:

- It is a shallow (between 0.5 and 1 m), sufficiently large (~1900 km^2), flat, and homogeneous saline lake.

- It is located at a high altitude (~900 m).

- It is a bright natural target and free of vegetation.

- It has a semi-arid climate and is one of the regions in Turkey, where least precipitation occurs.
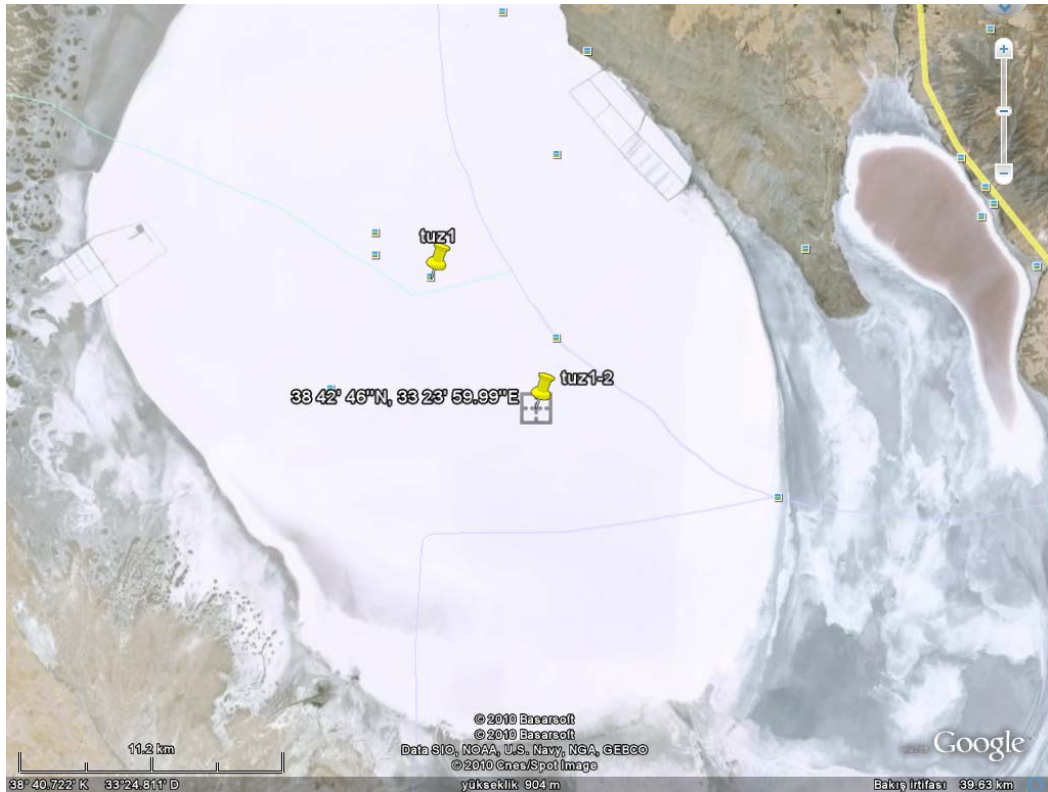
Figure 4-5 Salt Lake view (38.763˚N - 33.35 ˚E) [44].

Because of these properties, this lake is accepted to be a Lambertian surface, which has equal reflected radiances in all viewing directions depending on the incident angle of the incoming radiance when it hits the surface. Furthermore, we do not expect ε variations with vegetation for this calibration region because it has no vegetation. Least precipitation in this region can cause least ε variations depending on the precipitation among the other selected regions. Due to these properties, we expect high ε values (close to 1.0) in all bands for this lake when compared to other regions. For these reasons, we chose this region as a calibration and reference region for the other selected regions.

For this lake, calculated monthly ε_j values with their standard deviations are shown in Figure 4-6 for six different bands and four years, which are separated with dashed vertical lines. The standard deviations, which are

42

given in the figure as error bars for each month, are calculated from the four pixel and four year averages of the ε values for each month.

In Figure 4-6, we found that ε values are yearly periodic in the 3.660-4.080 μm and the 11.770-12.270 μm intervals (bands 20, 22, 23, and 32), but ε values in the 8.400-8.700 μm and 10.780-11.280 μm intervals (bands 29 and 31) are not. ε values are assumed to be constant, which are equal to 0.987 and 0.984 with standard deviation of 0.001 in the 10.780-11.280 μm and 11.770-12.270 μm intervals, respectively. This constant ε assumption can be explained by the MODIS ε retrieval algorithm because it fixes ε values of these intervals [31][36][38]. In addition, we can assume constant ε value in the 8.400-8.700 μm interval, which equals to 0.980 with standard deviation of 0.002. Therefore, we only considered periodic ε values in the 3.660-4.080 μm interval.

The periodicity in the 3.660-4.080 μm interval is due to low ε values in July and August and high ε values in winter and spring seasons, as seen in Figure 4-6. Similarly, precipitation is also expected to show periodicity due to the seasonal changes with snow in winter, rainfall in spring and autumn, and drought in summer. To determine whether the periodic behavior of ε is related to the precipitation or not, monthly precipitation amount, which is called p (kg/m^2), shown in Figure 4-7 is examined. As shown in the figure, p is high in spring season (particularly in April). Low precipitation occurs in summer (almost zero in July-August period) and winter (almost zero in December) seasons.
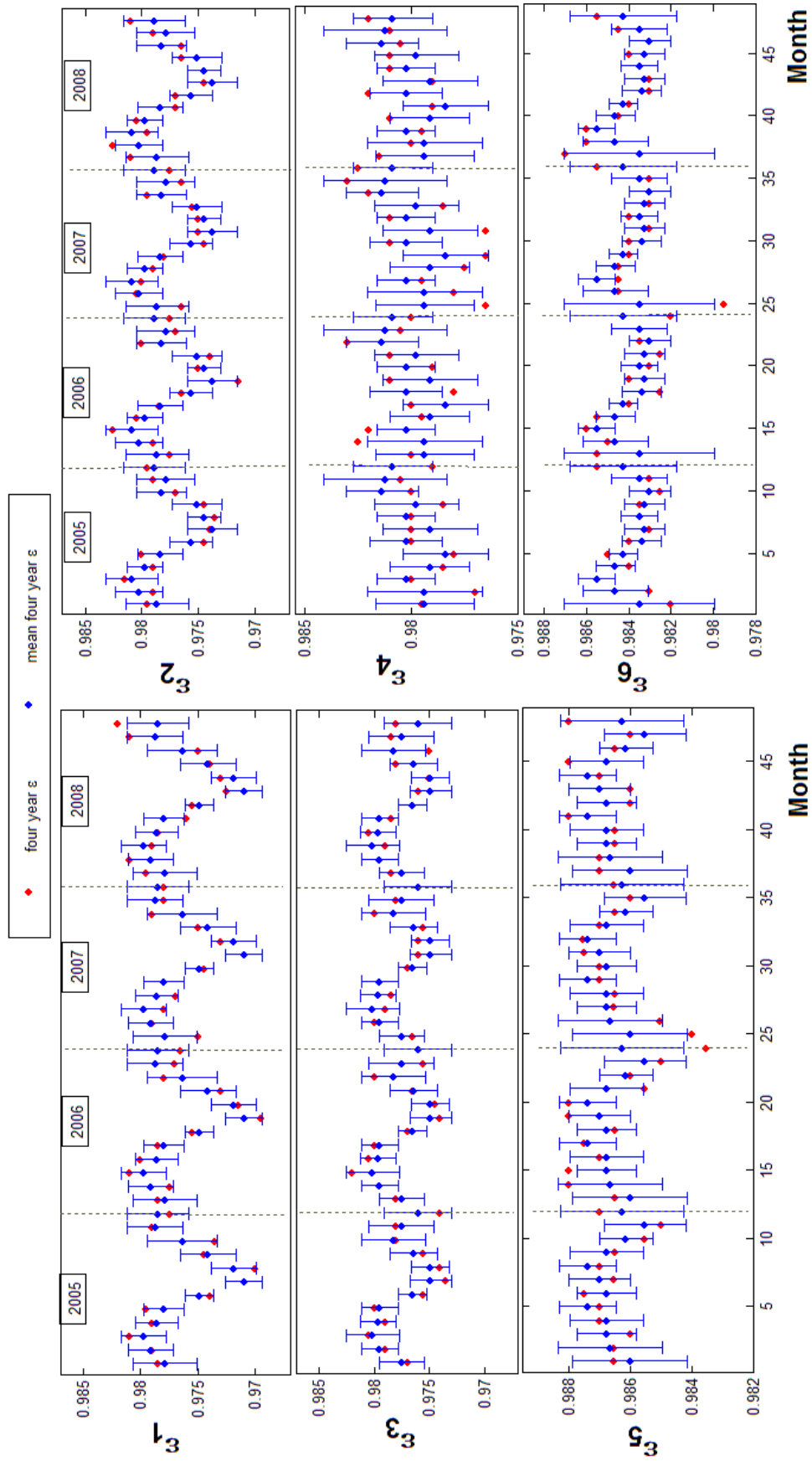
Figure 4-6 Calculated monthly ε_j values of Salt Lake for four years, which are separated with vertical dashed lines. Red dots show monthly ε values of for each four year. Monthly averaged ε values over four years are shown with blue dots and repeated in every year with their errors to check the periodicity. Six graphs for ε_1-ε_6 correspond to six band ε values from 3.660-3.840 μm to 11.770-12.270 μm intervals.
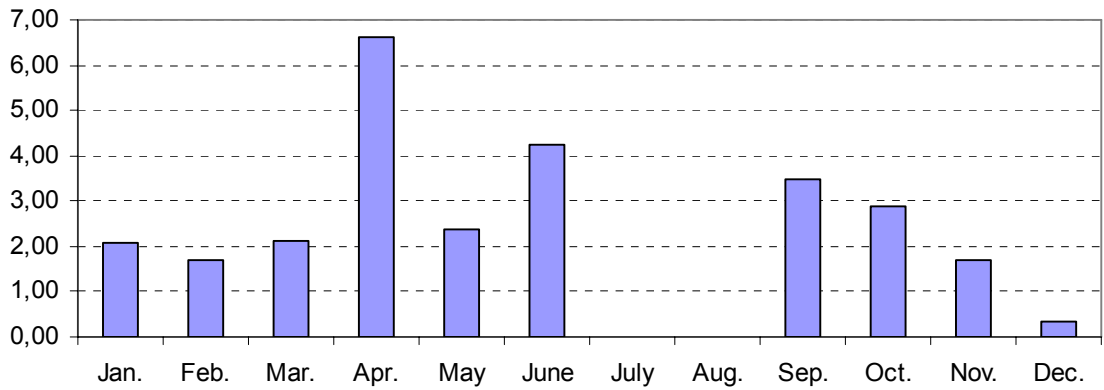
Figure 4-7 Turkish State Meteorological Services monthly p (kg/m^2) in 2006 for Salt Lake [43].

The possible correlation between the ε values and p is investigated with the graphs shown in Figure 4-8. In this graphs, ε values in the 3.660-4.080 μm interval are considered due to their periodicity.
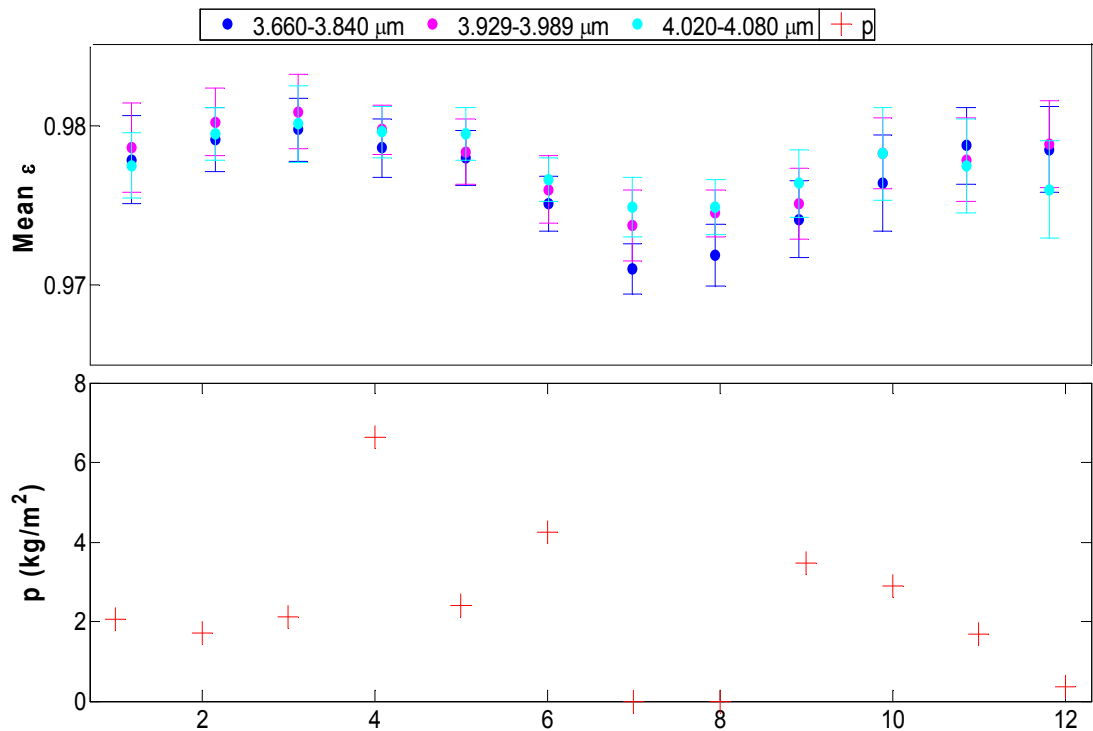
Figure 4-8 The first graph shows monthly ε values averaged over four years for three wavelength intervals. The last graph shows p in 2006.

As shown in Figure 4-8, both ε and precipitation are low in July and August. As a result, we concluded that almost zero precipitation in these months can

be the reason of decrease of ε values in the 3.660-4.080 μm interval. In December, precipitation is also low but ε values are not. Possible reason for this difference between July-August period and December can be drought and evaporation present in summer.

In July and August, high increase in the temperature with low precipitation causes drought and increase in the evaporation from the lake, which leaves a thick crust of salt on the surface [43][45][46]. Figure 4-9 shows the comparison of the lake views between May and July to demonstrate the evaporation and drought present in July.
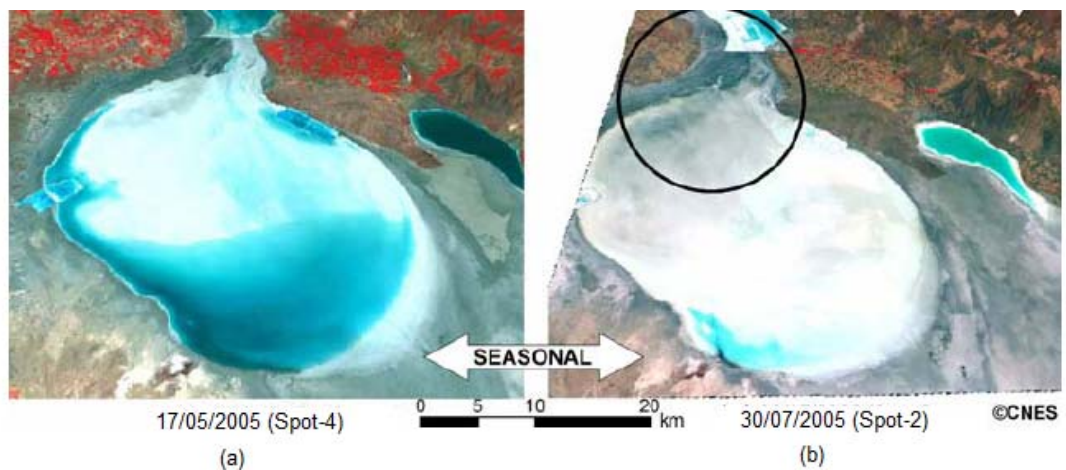
Figure 4-9 Seasonal changes in Salt Lake between months (a) May and (b) July. In these images white color in the lake corresponds to salt percentage [46].

In Figure 4-9, due to evaporation and drought, the lake becomes very shallow in July and August and it is expected to have low ε values at almost zero precipitation. In December precipitation is also low, but drought and evaporation do not occur and lake is not very shallow. In addition, if snow-ice covers the lake during December, ε values are not expected to be low [9][40].

Furthermore, Figure 4-8 shows that ε values in spring season are high in all bands showing similar characteristics as precipitation. P is also high in autumn, but ε values increase at the end of the season in the same figure.

As a summary, except for July-August period and spring season, we could not generalize the ε dependency on the precipitation. We can conclude that ε values have periodic behavior in the 3.660-4.080 μm interval. Because of this periodicity, Figure 4-8 can be used for the estimation of the monthly ε values. On the other hand, ε values in the 8.400-8.700 μm interval are not periodic and they fluctuate independent from the precipitation as given in Figure 4-6. ε values corresponding to 8.400-8.700 μm interval are affected much from the factors other than precipitation.

Figure 4-10 shows monthly averaged ε values over four years for each month in the six different wavelength intervals, which are used as reference for the ε values of the other selected regions.

4.2.2 Barren-sparsely vegetated regions

For barren-sparsely vegetated regions TUG and Konya regions are chosen because both of them have no or sparse vegetation covers. In the following sections, we provide a detailed investigation of monthly and spectral ε variations for each region using precipitation and ε_j values of these regions.

4.2.2.1 TUG region

TUG region, shown in Figure 4-11, is located in Antalya close to the TÜBİTAK National Observatory (TÜBİTAK Ulusal Gözlemevi-TUG) whose

altitude is greater than 2000 m. This region has only sparse savanna which can grow above 2000 m [50].
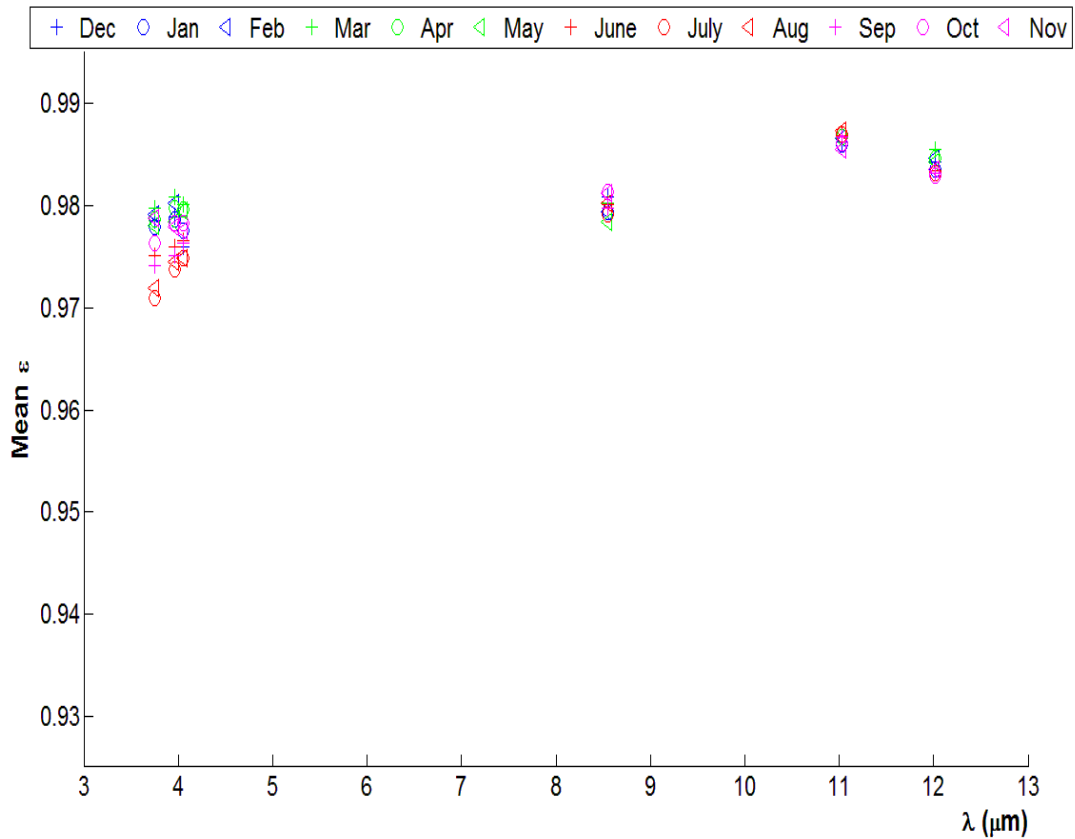
Figure 4-10 Monthly averaged ε values over four years are shown with respect to wavelength (Blue, green, red, and magenta colors represent winter, spring, summer, and autumn seasons, respectively.) Note that for this graph y axis rangeis fixed to 0.93-0.99 for all selected regions.

Intense snowfall occurs during winter season in this region generally between November and April [47]. Snow cover due to this intense snowfall hinders and dominates underlying soil ε. Snow ε values are high and snow cover results in high ε values [9][40]. For this reason, we expect high ε values starting from November to April (especially in winter). This snow effect is expected to be dominant factor on ε variations because this region has only sparse savanna.
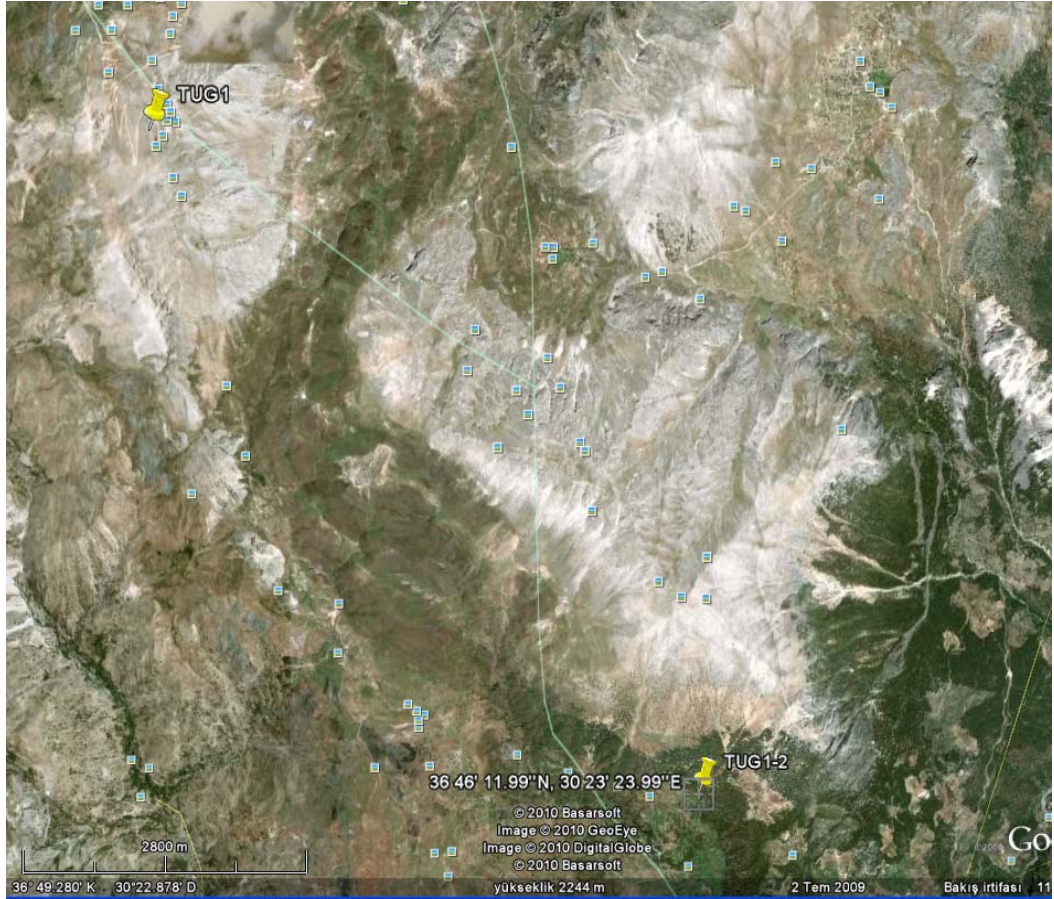
Figure 4-11 View of TUG region (36.82 ˚N - 30.34 ˚E) [44].

For this region, calculated monthly ε_j values are shown in Figure 4-12 with their standard deviations for six bands and four years. In Figure 4-12, we found that ε values are yearly periodic in the 3.660-4.080 μm and 11.770-12.270 μm intervals, but not in the 8.400-8.700 μm and 10.780-11.280 μm intervals. High standard deviations of ε are computed in March and in December in the 3.660-4.080 μm and 11.770-12.270 μm intervals, respectively because ε data corresponding to some pixels and years diverge much from the mean. In the 10.780-11.280 μm and 11.770-12.270 μm intervals, we determined constant ε values, which are equal to 0.982 and 0.986 with standard deviations of 0.001 and 0.002, respectively because ε values are fixed in these intervals [31][36][38]. In the 8.400-8.700 μm interval, we can assume constant ε value, which is 0.977 with standard deviation of 0.003. As a result of these constant ε values, we only considered periodic ε values in the 3.660-4.080 μm interval.

49
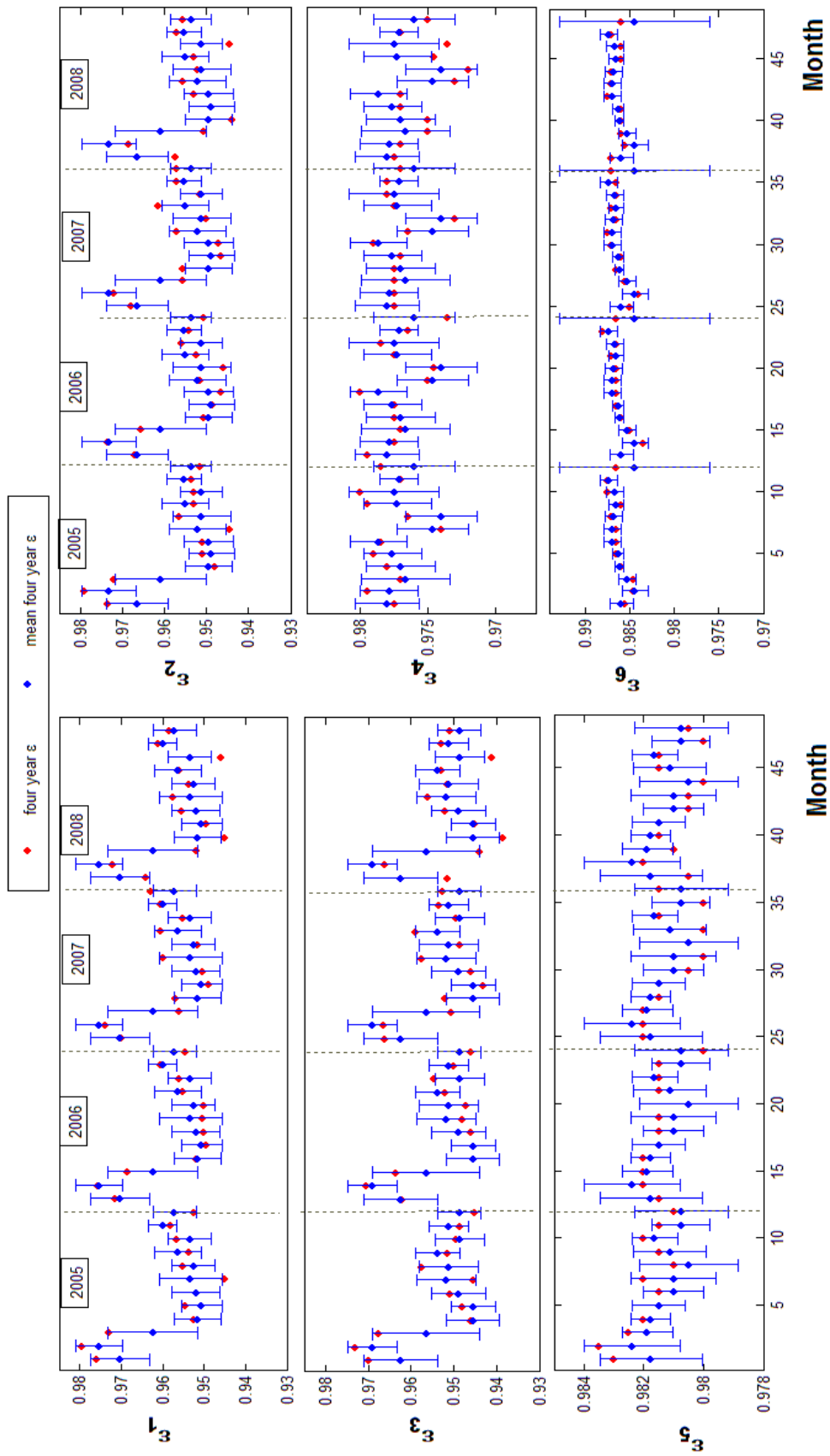
Figure 4-12 Calculated monthly ε_j values of TUG region for four years, which are separated with vertical dashed lines. Red dots show monthly ε values of each four year. Monthly averaged ε values over four years are shown with blue dots and repeated in every year with their errors to check the periodicity. Six graphs for ε_1-ε_6 correspond to six band ε values from 3.660-3.840 μm to 11.770-12.270 μm intervals.

In Figure 4-12, the periodicity in the 3.660-4.080 µm interval is due to high ε values and sharp ε peak in January, February, and March. In the 3.660-3.989 µm interval ε values increase starting from November to February. We also note that snow cover can remain on the surface during these months [47]. For this reason, a possible effect of precipitation (mostly snow in this region) on the periodic behavior of ε is studied using monthly p for Antalya given in Figure 4-13.
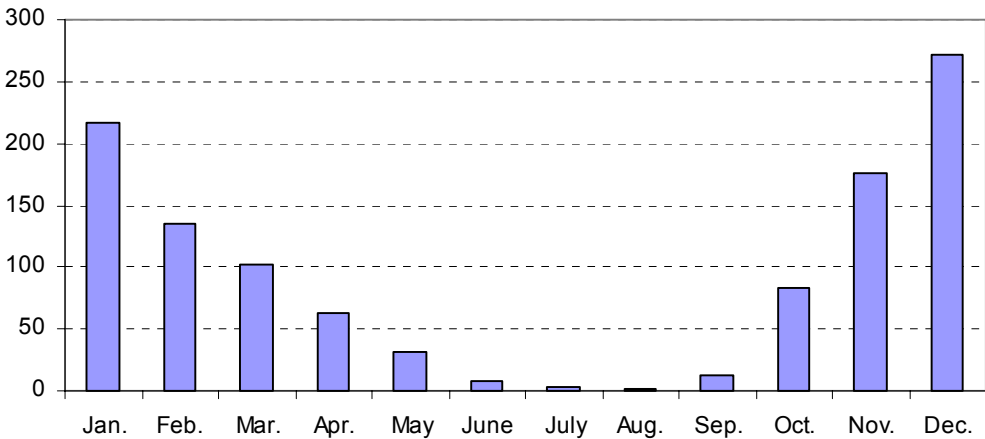
Figure 4-13 Average (1975-2008) monthly p (kg/m^2) for Antalya [45].

As shown in Figure 4-13, precipitation decreases continuously from January to August and low precipitation occurs during summer season (particularly in July and August). Precipitation increases starting from September to December and high precipitation occurs during the winter season (particularly in December and January) due to snow. The possible correlation between p and ε values is examined with the graphs shown in Figure 4-14.
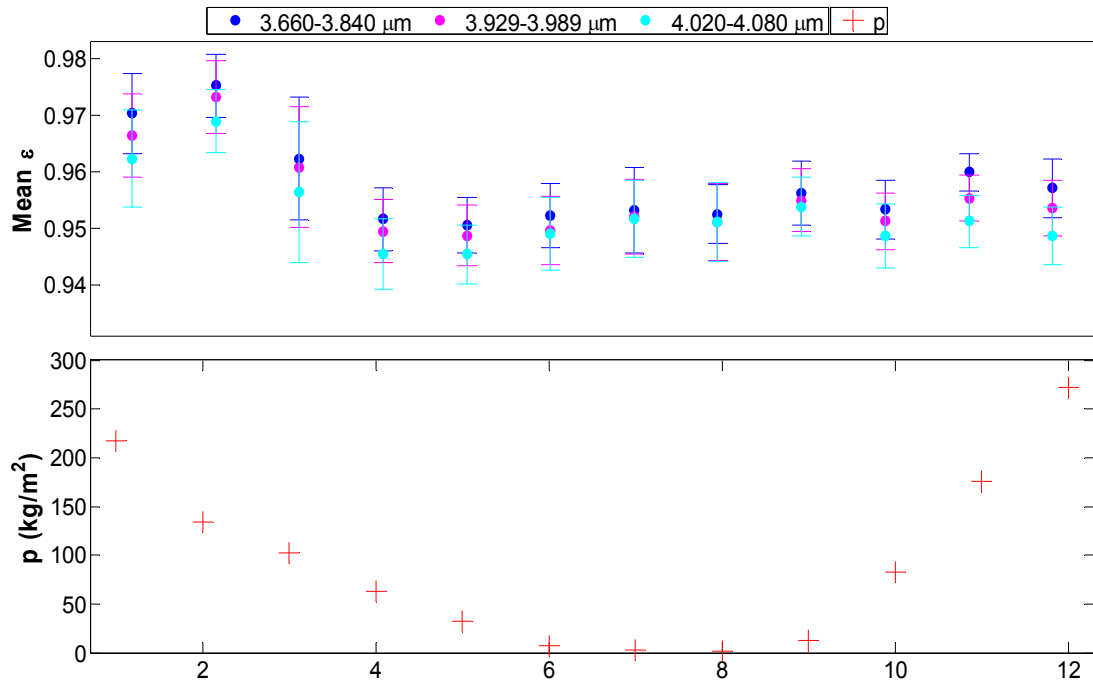
Figure 4-14 The first graph shows monthly ε values averaged over four years for three wavelength intervals. The last graph shows long years averaged p.

Figure 4-14 shows that both ε values and precipitation are high in January. In addition, it is known that snow cover remains in TUG region from November to April [47]. As a result, high precipitation (intense snowfall) and snow cover result in high ε values in January [9][40]. Similar to January, we expect high ε values also in December due to high precipitation occurring in winter. In December, precipitation is highest, but ε values are not. This difference in the ε values between January and December can be explained by the different ε values of snow cover and snowfall. In January, very intense snow cover is present due to high precipitation (snowfall) in December, resulting in high ε values. For this reason, in December lower ε values can be found contrary to high precipitation when compared to January.

As shown in Figure 4-14, ε values decrease with precipitation starting from February to May due to snowmelt. Furthermore, ε values in the 3.660-3.989 μm interval are higher in November when compared to those in other months (except January, February, and March.) due to high precipitation.

Moreover, precipitation is low in July and August; however, ε values are not, depending on the factors other than precipitation.

To summarize, we determined that ε values are yearly periodic in the 3.660-4.080 μm interval and nearly constant in the 8.400-8.700 μm and 10.780-11.280 μm intervals similar to our results obtained for the Salt Lake. ε values are periodic in the same intervals for the Salt Lake and TUG regions. As a result of the periodic ε values in the 3.660-4.080 μm interval, we can estimate monthly ε values using Figure 4-14.

We concluded that for TUG region snow is dominant factor on the ε values in the 3.660-4.080 μm interval because snow cover causes peak ε values in January and February and ε values decrease with snow melt between February and May. Salt Lake has also high ε values in winter, but not as much as high when compared to TUG region because we expect that calibration region is affected less from the seasonal variations when compared to other regions. Moreover, in TUG region ε values do not decrease with low precipitation in July and August contrary to the calibration region. For this reason, we can conclude that low precipitation is more effective on ε values for Salt Lake when compared to the TUG region. Figure 4-15 shows monthly averaged ε values over four years for each month in the six different wavelength intervals for TUG region. This figure is given to compare ε values of TUG with reference ε values of Salt Lake.

ε values of TUG in Figure 4-15 are lower than reference values in Figure 4-10 in all wavelength intervals and months. Therefore, ε values are higher in calibration region as expected. In the next section, Konya region is studied to confirm our results from barren-sparsely vegetated regions.
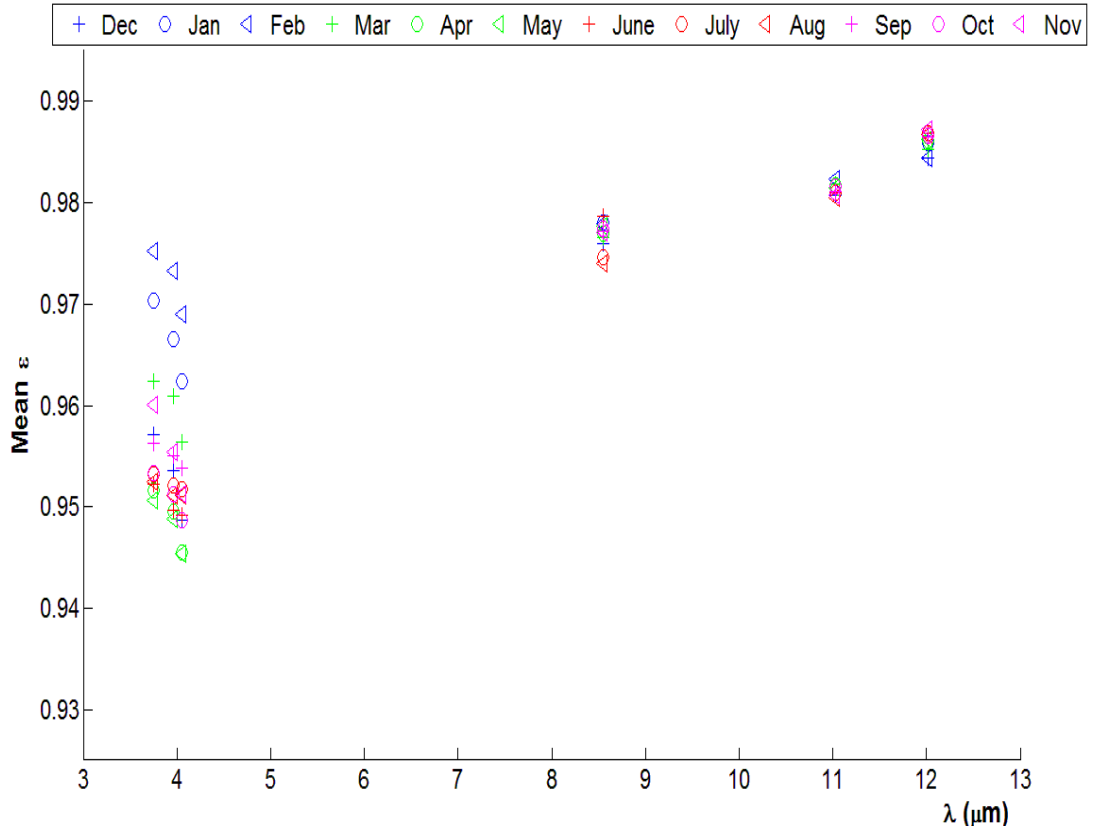
Figure 4-15 Monthly averaged ε values over four years are shown with respect to wavelength. (Blue, green, red, and magenta colors represent winter, spring, summer, and autumn seasons, respectively.)

4.2.2.2 Konya region

Konya region, shown in Figure 4-16, is barren-sparsely vegetated and its altitude is approximately 1500 m [44].

Figure 4-16 View of Konya region (38.10˚N - 35.35˚E) [44].

For this region, calculated monthly ε_j values with their standard deviations are shown in Figure 4-17 for six bands and four years. In Figure 4-17, we determined that ε values are yearly periodic in the 3.660-4.080 μm interval, but not in the remaining intervals. In the 10.780-11.280 μm and 11.770-12.270 μm intervals, we determined constant ε values, which are equal to 0.981 and 0.986 with standard deviation of 0.001, respectively because of fixed ε values in these intervals [31][36][38]. In addition, we can assume constant ε value 0.977 with standard deviation of 0.002 in the 8.400-8.700 μm interval. High standard deviations of ε values are present in August and December in the 8.400-8.700 μm and 11.770-12.270 μm intervals, respectively because ε data of some pixels and years diverge much from the mean. As a result of these constant ε values, we only considered periodic ε values in the 3.660-4.080 μm interval.
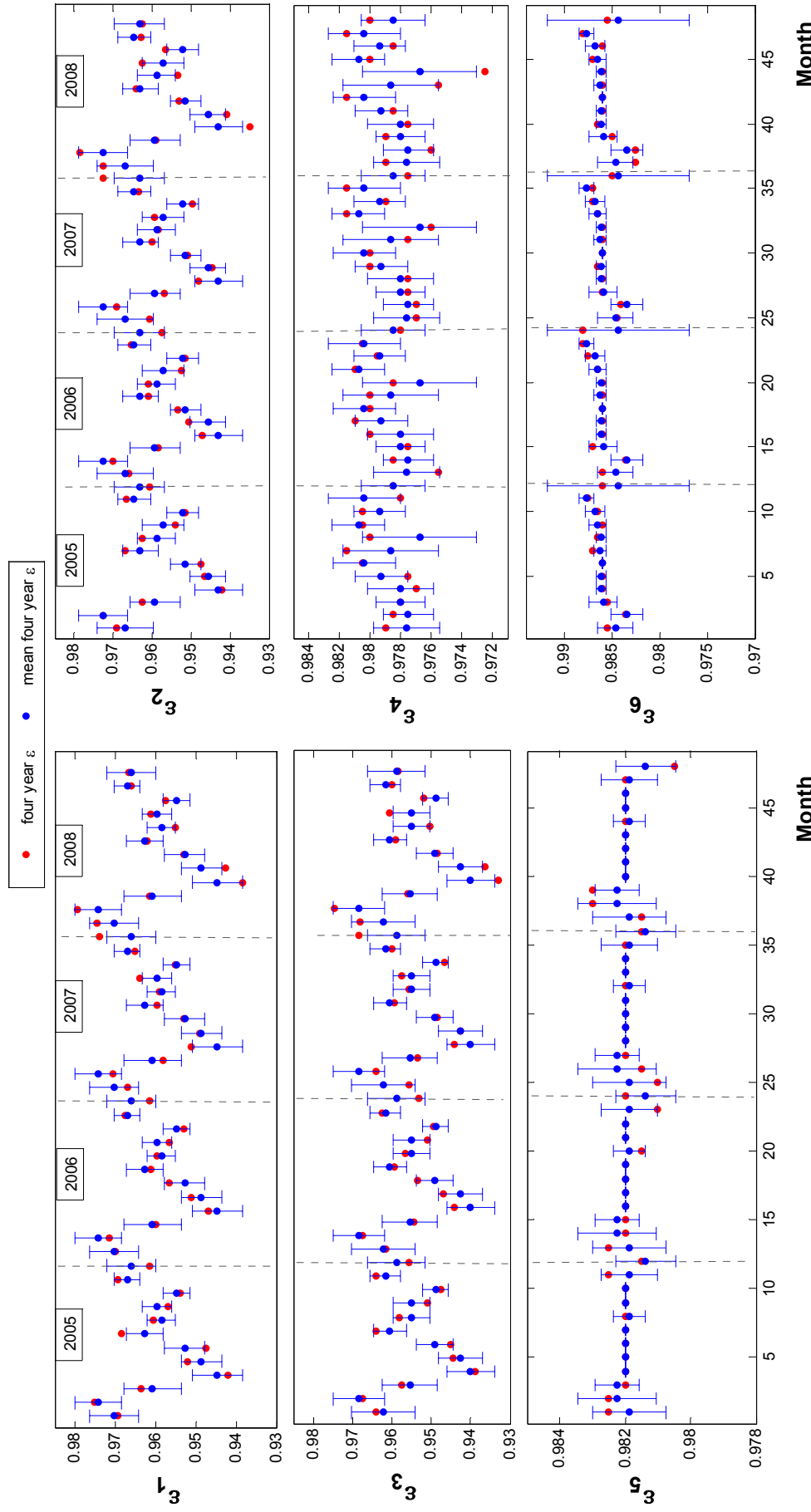
Figure 4-17 Calculated monthly ε_j values of Konya region for four years, which are separated with vertical dashed lines. Red dots show monthly ε values of each four year. Monthly averaged ε values over four years are shown with blue dots and repeated in every year with their errors to check the periodicity. Six graphs for ε_1-ε_6 correspond to six band ε values from 3.660-3.840 μm to 11.770-12.270 μm intervals.

56

In Figure 4-17, the periodicity in the 3.660-4.080 µm interval is due to increase and decrease in ε values between different months, high ε values in winter season, and low ε values in April and May. In order to investigate possible effect of precipitation on the periodic behavior of ε, monthly p for Konya given in Figure 4-18 is used.
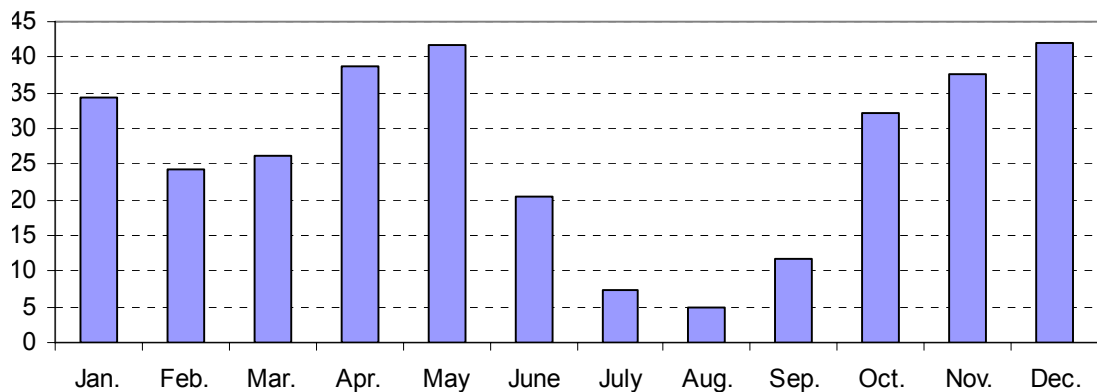
Figure 4-18 Average (1975-2008) monthly p (kg/m^2) for Konya [45].

As shown in Figure 4-18, low precipitation occurs in July and August and high precipitation occurs in spring and winter seasons. Precipitation increases starting from September to December and from February to May because of rainfall in spring and snowfall in winter. It decreases starting from May to August due to drought occurring in summer season. The possible correlation between the ε values and monthly p is investigated with the graphs given in Figure 4-19.

As shown in Figure 4-19, both p and ε increase starting from October to January and have high values during this period. High precipitation also occurs in April and May, but contrarily, ε values are even low. Possible reason for this difference is the high precipitation in winter and at the end of autumn is due to snowfall and/or snow coverage resulting in high ε values [9][40]. For these reasons, we concluded that ε values increase with increase in precipitation starting from October to January. In addition, ε values decrease starting from February to April and this decrease is most probably due to snow melt. Moreover, we determined that decrease in

57

precipitation in July and August does not have an influence on the ε values. Therefore, we concluded that precipitation in the form of snow raises ε values in the 3.660-4.080 µm interval in winter and at the end of autumn and it is the dominant factor on ε values in this region.
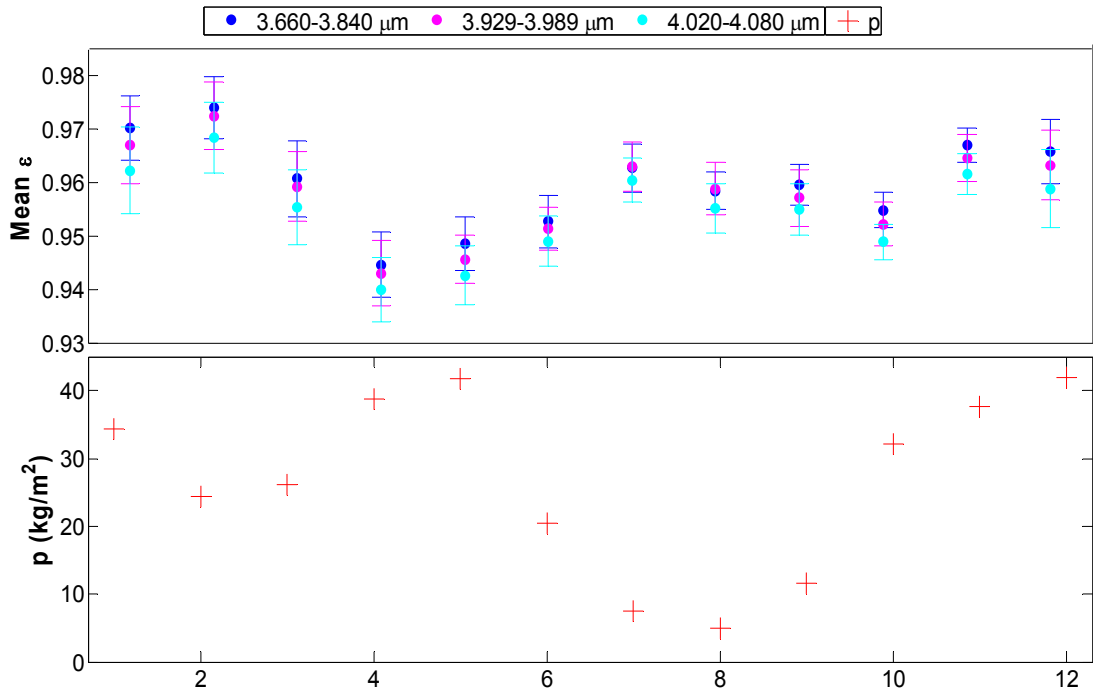
Figure 4-19 The first graph shows monthly ε values averaged over four years for two wavelength intervals. The last graph shows long years averaged p.

As a summary, we found that ε values are periodic in the 3.660-4.080 µm interval and nearly constant in the 8.400-8.700 µm and 10.780-11.280 µm intervals, similar to our results for the Salt Lake. As a result of this periodicity, Figure 4-19 can be used for the estimation of the monthly ε values in the 3.660-4.080 µm interval. Furthermore, we determined that ε values in this interval are high during winter and increase with precipitation between October and January due to snowfall. In calibration region, ε values are also high in winter, but not as much as those in Konya region. Because we expect that ε values of calibration region are less affected from the seasonal changes when compared to other regions. We concluded that precipitation lowering (particularly in July and August) is not affective on ε values in the 3.660-4.080 µm interval, contrary to calibration region because

Salt Lake suffers from evaporation and drought. In addition, the decrease in ε values with precipitation in July and August in calibration region is small when compared to ε variations in Konya region. To make a comparison between ε values of Konya and reference ε values of the calibration region, monthly averaged ε values over four years for each month in the six different wavelength intervals for Konya region are shown in Figure 4-20. ε values of Konya region, given in Figure 4-20, are lower than reference ε values in Figure 4-10 in all wavelength intervals and months. As a result, the calibration region has high ε values, as expected.

To determine common ε properties of the barren-sparsely vegetated regions, we made a comparison between the results of TUG and Konya regions. Both regions have periodic ε values in the 3.660-4.080 μm interval and by means of this periodicity monthly ε values in this interval can be estimated for these regions. In winter and spring seasons, ε values for these regions are close to each other. In other seasons, ε values in these two regions differ depending on different soil types and precipitation properties of these regions. In the 8.400-8.700 μm and 10.780-12.270 μm intervals, ε values are nearly constant and close for both regions.

In these two regions, ε values do not decrease with low precipitation occurring in summer (drought). As a result, we determined that ε values in the 3.660-4.080 μm interval are not affected from drought in barren-sparsely regions. For both regions we found that ε values in this wavelength interval increase considerably with precipitation during winter season. Snowfall dominates and raises surface ε because these regions have sparse vegetation cover. For these reasons, we concluded that snow coverage dominantly affects the ε values in the 3.660-4.080 μm interval for barren regions.
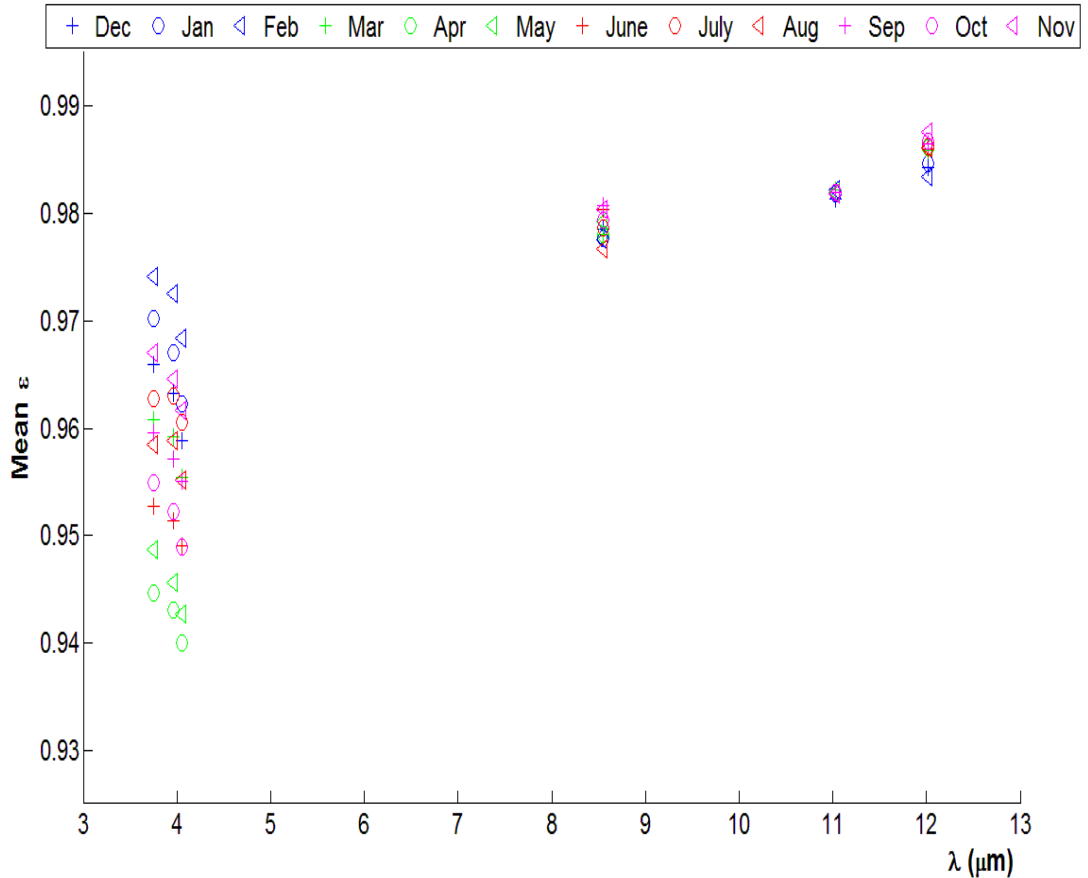
Figure 4-20 Monthly averaged ε values over four years are shown with respect to wavelength. (Blue, green, red, and magenta colors represent winter, spring, summer, and autumn seasons, respectively.)

Finally, both of the regions have higher monthly ε variations and smaller ε values for all months and wavelength intervals when compared to the calibration region. As a result, we proved that calibration region has higher ε values and less ε variations as expected.

4.2.3 Woodland regions

For woodland regions, Küre and Antalya forests are chosen because both of these regions are densely covered with forests and not affected from the human activities, such as urbanization and agriculture. In the following sections, we provide a detailed investigation of monthly and spectral ε variations using precipitation and ε_j values of each region.

4.2.3.1 Küre region

Küre region, shown in Figure 4-21, has an altitude 1000 m. approximately [44]. This region in Kastamonu is located in the north of the Turkey (see Figure 4-4), where high precipitation occurs throughout a year [51]. For this reason, we also expect high precipitation in all seasons.

Dense forest masks the underlying soil spectral signature like snow cover and dominates surface ε as we discussed in the previous chapter. For this reason, we do not expect too much ε variations with precipitation contrary to barren-sparsely vegetated regions. In addition, we expect high ε values for this region when compared to barren-sparsely vegetated and cropland regions because dense forest has high ε values and raises ε [25].
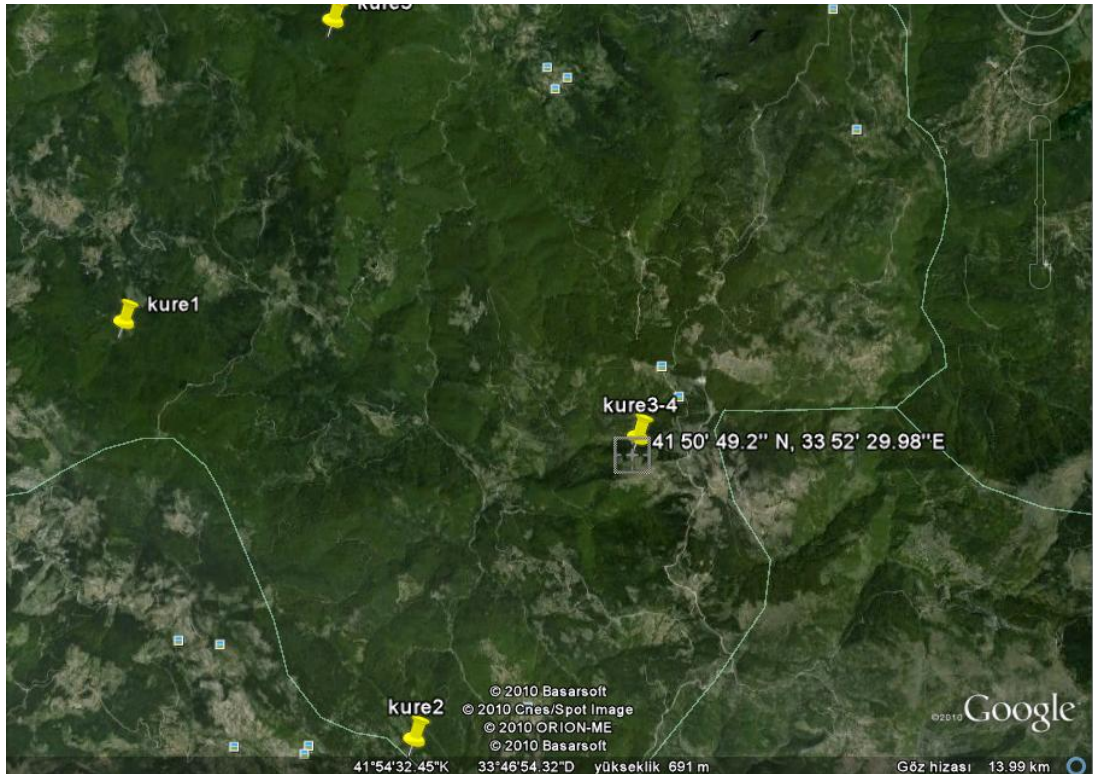
Figure 4-21 View of Küre region (41.861 ˚N - 33.789˚E) [44].

For this region, calculated monthly ε_j values with their standard deviations are shown in Figure 4-22 for six bands and four years. As shown in Figure 4-22, ε values are yearly periodic in the 3.660-3.989 µm, 8.400-8.700 µm, and 11.770-12.270 µm (bands 20, 22, 29, and 32) intervals but not in the remaining intervals. High standard deviations of ε are computed in January in the 10.780-11.280 µm interval because ε data corresponding to some pixels and years diverges much from the mean. In the 10.780-11.280 µm and 11.770-12.270 µm intervals, we determined constant ε values, which are equal to 0.982 and 0.987 with standard deviation of 0.001, respectively because MODIS fixes ε values in these intervals [31][36][38]. In addition, we can also assume constant ε value in the 4.020-4.080 µm interval, which is 0.970 with standard deviation of 0.004. As a result of these constant ε values, we only considered periodic ε values in the 3.660-3.989 µm and 8.400-8.700 µm intervals.

In Figure 4-22, the periodicity in the 3.660-3.989 µm interval is due to continuous decrease in ε from February to August, low ε values in August, and continuous increase in ε values from August to January. ε values in the 8.400-8.700 µm are periodic due to low ε values in August and high ε values in May, June, and October. ε values in both intervals are lowest in August and low precipitation occurring in this month can be possible reason for this similarity. A possible influence of precipitation on the periodic behavior of ε is examined using monthly p for Kastamonu given in Figure 4-23.
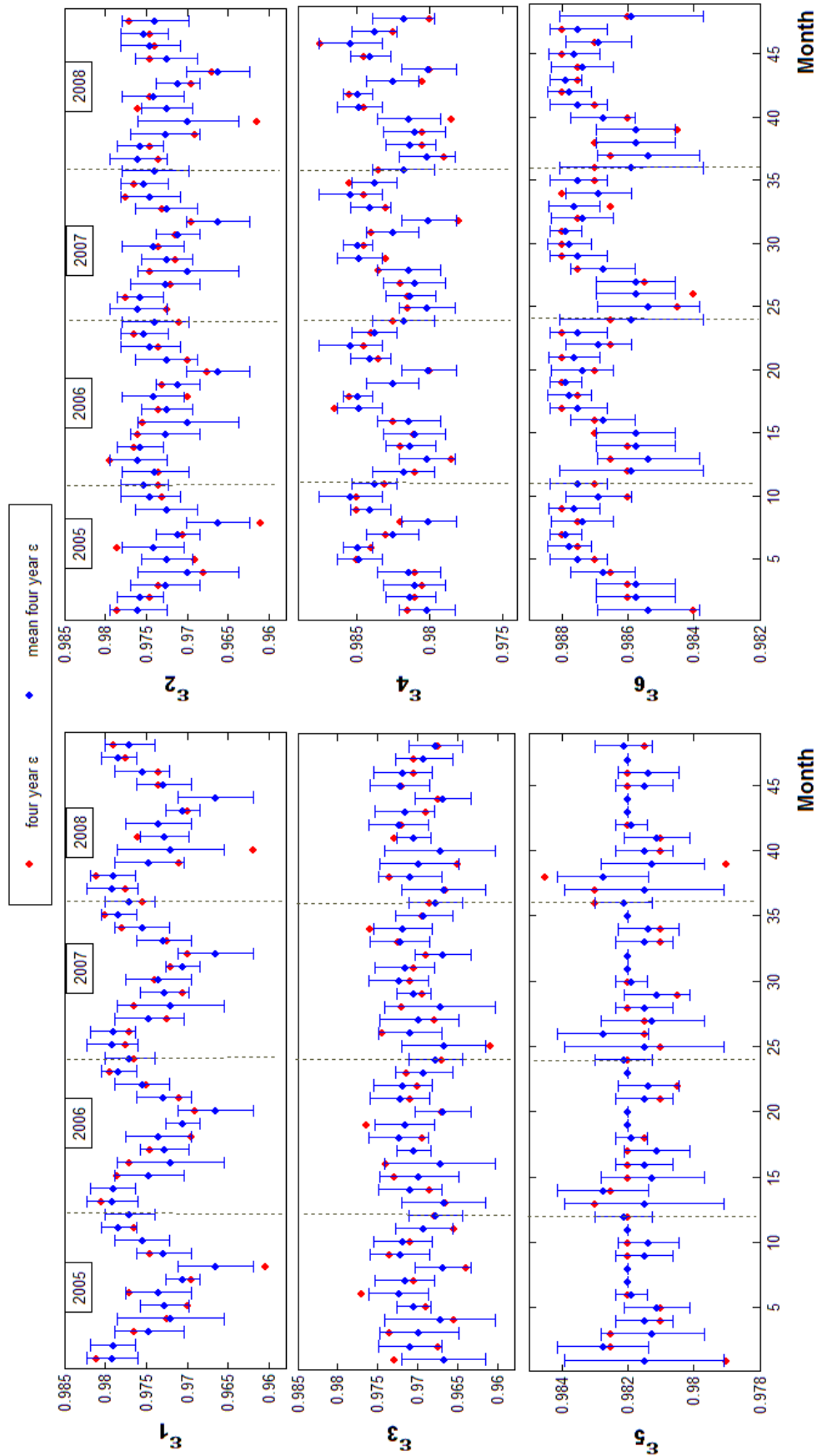
Figure 4-22 Calculated monthly ε_i values of Küre region for four years, which are separated with vertical dashed lines. Red dots show monthly ε values of each four year. Monthly averaged ε values over four years are shown with blue dots and repeated in every year with their errors to check the periodicity. Six graphs for ε_1-ε_6 correspond to six band ε values from 3.660-3.840 μm to 11.770-12.270 μm intervals.

63
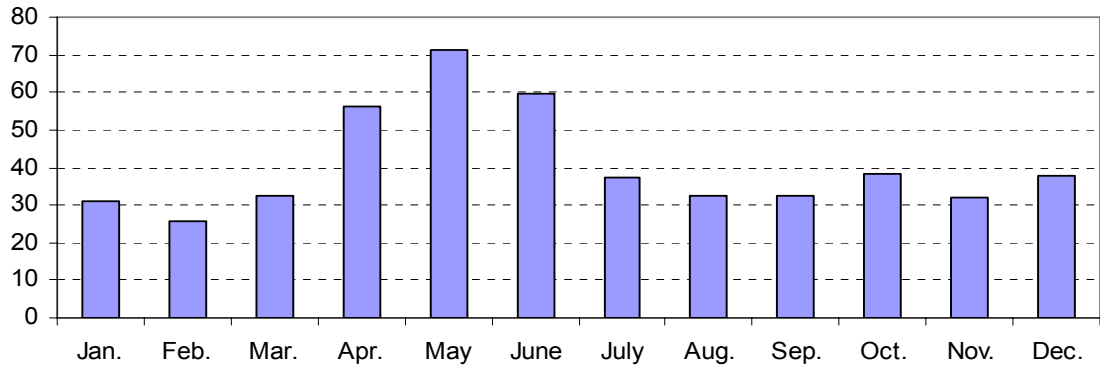
Figure 4-23 Average (1975-2008) monthly p (kg/m^2) for Kastamonu [45].

As shown in Figure 4-23, p is generally high throughout the year and highest precipitation occurs in spring and summer. p decreases starting from May to August and increases starting from February to May. The possible correlation between the ε values and monthly p is investigated with the graphs shown in Figure 4-24.
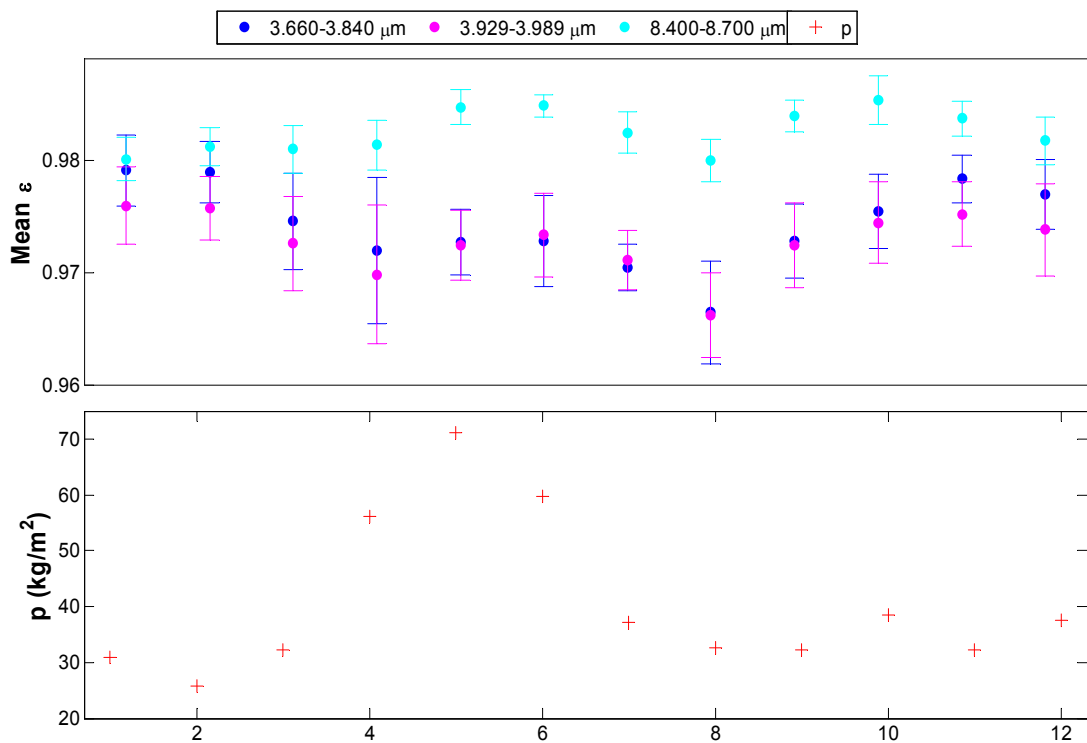
Figure 4-24 The first graph shows monthly ε values averaged over four years for three wavelength intervals. The last graph shows long years averaged p.

As shown in Figure 4-24, ε values in the three wavelength intervals and p decrease during summer (lowest in July and August). Therefore, we found that ε values in the 3.660-3.989 µm and 8.400-8.700 µm intervals decrease with the decrease in precipitation in summer season. ε values increase starting from April to June with the increase in precipitation due to rainfall. However, ε values also increase during autumn season contrary to the p. In addition, during winter season, ε values are high in the 3.660-3.989 µm interval, contrary to p. Furthermore, we determined that ε variations are small in other months except for low ε values in August in the 3.660-3.989 µm interval and high ε values in May and June in the 8.400-8.700 µm interval. As a result of these differences between the periodicity of ε values and the precipitation, we concluded that except May and August, ε values in the 3.660-3.989 µm and 8.400-8.700 µm intervals are not much affected from precipitation due to dense forest as expected. Dense forest hinders underlying surface ε and forest ε becomes dominant resulting in high and more stable ε values.

As a summary, ε values in the 3.660-3.989 µm and 8.400-8.700 µm intervals are periodic and this periodicity can be used to estimate monthly ε values in these intervals using Figure 4-24. However, ε values are nearly constant in the 8.400-8.700 µm interval in Salt Lake. Vegetation (forest) can be possible reason for the different periodicities occurred between the two regions. Moreover, we found that ε variations in the calibration region are smaller than those in Küre region as expected. Because calibration region has no vegetation and low precipitation contrary to Küre region, we expect less ε variations for Salt Lake when compared to Küre region. Both of the regions have lowest ε values in August in the 3.660-3.989 µm interval. Therefore, we can conclude that ε values of both regions in the 3.660-3.989 µm interval decrease with decrease in precipitation. During winter season, ε values are high in both regions. In order to make a comparison between ε values of Küre region and reference ε values of calibration region, Figure 4-25, which

shows monthly averaged ε values over four years for each month in the six wavelength intervals for Küre region, is given.
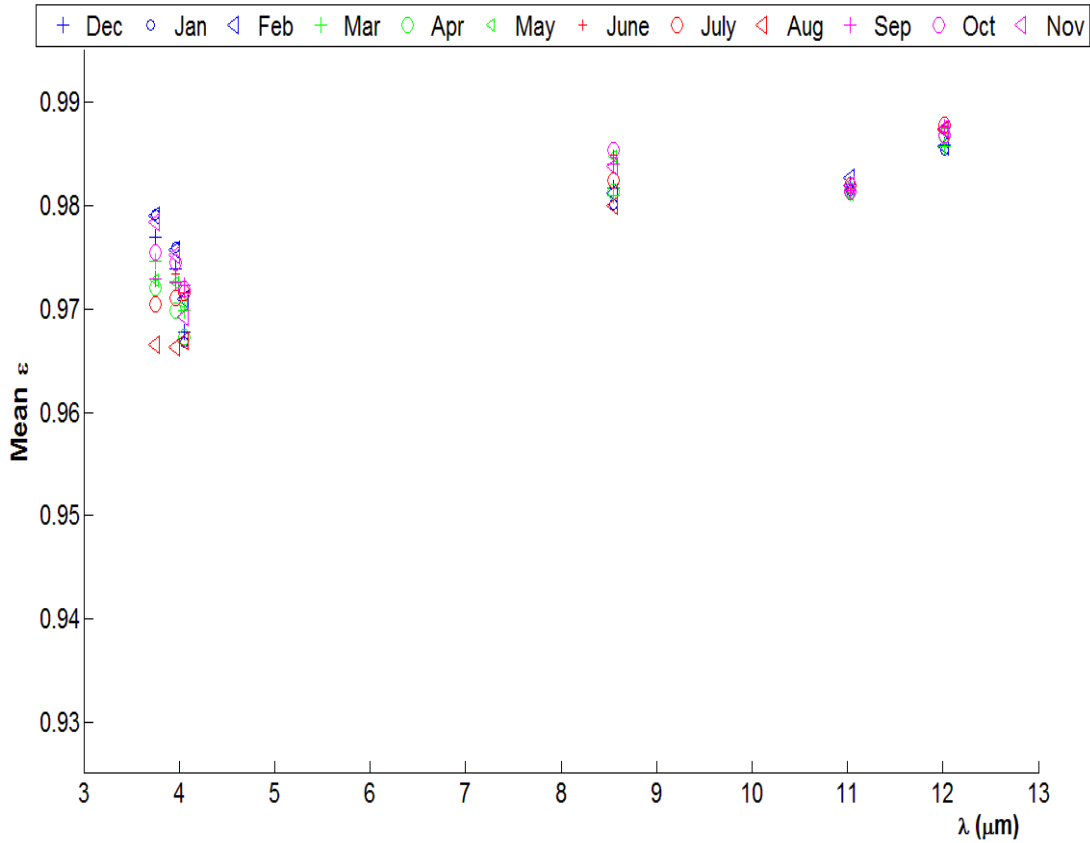
Figure 4-25 Monthly averaged ε values over four years are shown with respect to wavelength (Blue, green, red, and magenta colors represent winter, spring, summer, and autumn seasons, respectively.)

We found that ε values for Küre region in Figure 4-25 are lower than those reference ε values for the calibration region, given in Figure 4-10, in all wavelength intervals and months. Therefore, calibration region has high ε values as expected. In the next section, Antalya region is studied to confirm our results for woodland regions.

4.2.3.2 Antalya region

Antalya region, shown in Figure 4-26, has an altitude 300 m approximately [44]. For this region, we do not expect too much ε variations with

66

precipitation, due to dense forest cover because dense forest cover masks the underlying soil spectral signature and dominates surface ε. As a result, we expect high ε values for this region when compared to barren-sparsely vegetated and cropland regions, because dense forest has high ε values and raises surface ε [25].

Figure 4-26 View of Antalya region (37.253 °N - 30.863 °E) [44].

Calculated monthly ε_j values with their standard deviations are shown in Figure 4-27 for six bands and four years. In Figure 4-27, we found that ε values are yearly periodic in the 8.400-8.700 μm and 11.770-12.270 μm intervals, but not in the 3.660-4.080 μm and 10.780-11.280 μm intervals. Standard deviations of ε are very high in the 3.660-4.080 μm interval because ε data of some pixels and years diverge much from the mean. For this reason, we assumed constant ε values, which are 0.9650, 0.9633, and 0.9550 with standard deviations of 0.0094, 0.0093, and 0.0126 in the 3.660-3.840 μm, 3.929-3.989 μm, and 4.020-4.080 μm intervals, respectively. In the 10.780-11.280 μm and 11.770-12.270 μm intervals, we determined

constant ε values, which are equal to 0.9810 and 0.9860 with standard deviation of 0.001, respectively because of fixed ε values in these intervals [31][36][38]. As a result of these constant ε values, we only considered periodic ε values in the 8.400-8.700 μm interval.

As shown in Figure 4-27, periodicity in the 8.400-8.700 μm interval is due to decrease in ε values starting from April to May and lowest ε values in July and August, and high ε values in spring (particularly in April and May). Monthly p for Antalya, (see Figure 4-13), is used to investigate the possible correlation between the p and ε values from the graphs given in Figure 4-28.

Figure 4-28 shows that except July and August ε values are high and nearly stable with respect to season. Dense forest cover is possible reason for these high and nearly stable ε values in most of the year. We showed that ε values of dense forest in the 8.400-8.700 μm interval do not show significant changes with respect to season except July and August. ε values decrease during summer season and similarly p is also low in the same season. On the other hand, low precipitation occurs in May and June, contrary to ε. This difference can be explained as ε values of trees are expected to be high during spring season. Therefore, we concluded that ε values in the 8.400-8.700 μm interval decrease during summer with low precipitation.
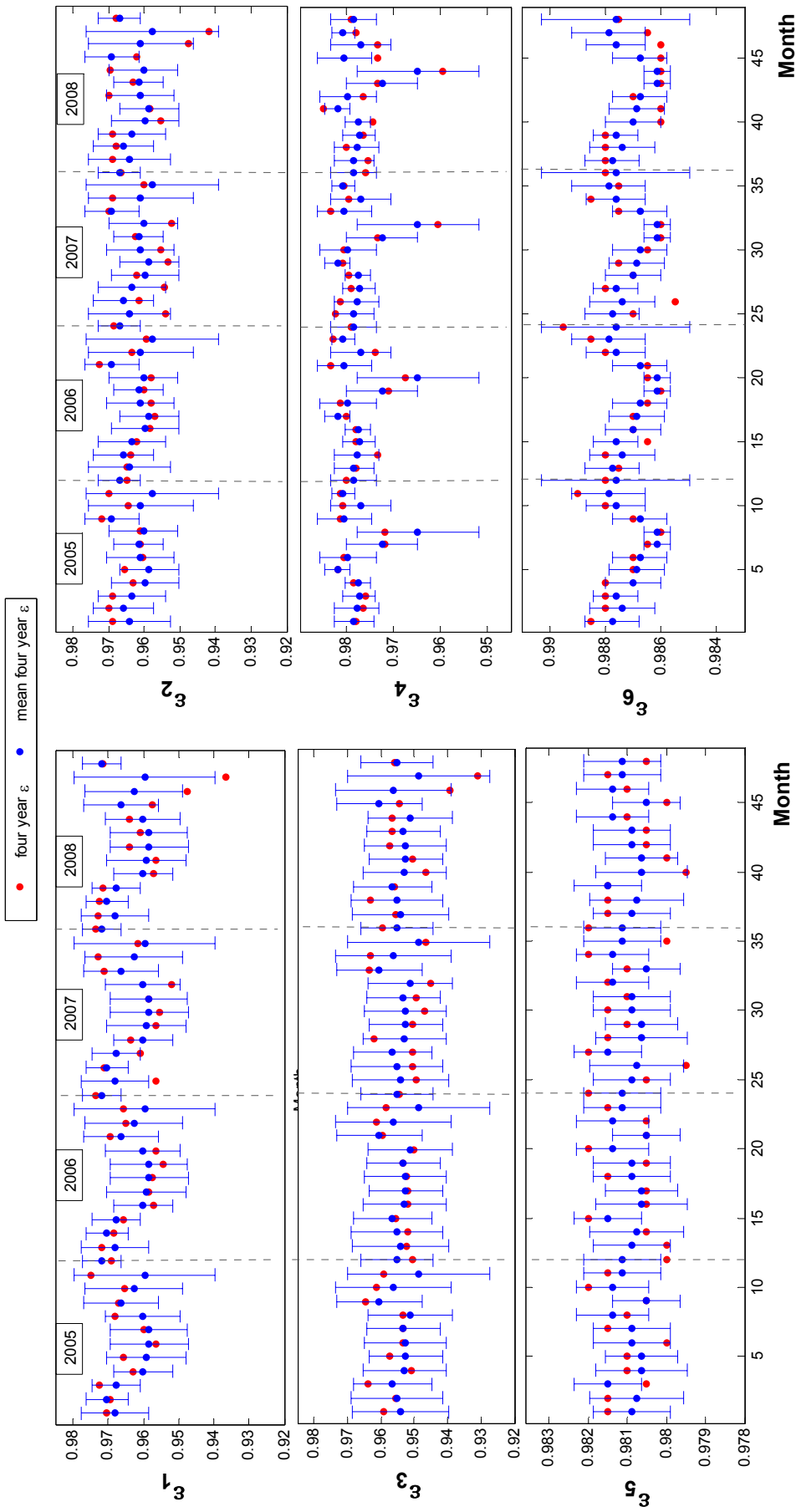
Figure 4-27 Calculated monthly ε_j values of Antalya region for four years, which are separated with vertical dashed lines. Red dots show monthly ε values of each four year. Monthly averaged ε values over four years are shown with blue dots and repeated in every year with their errors to check the periodicity. Six graphs for ε_1-ε_6 correspond to six band ε values from 3.660-3.840 µm to 11.770-12.270 µm intervals.
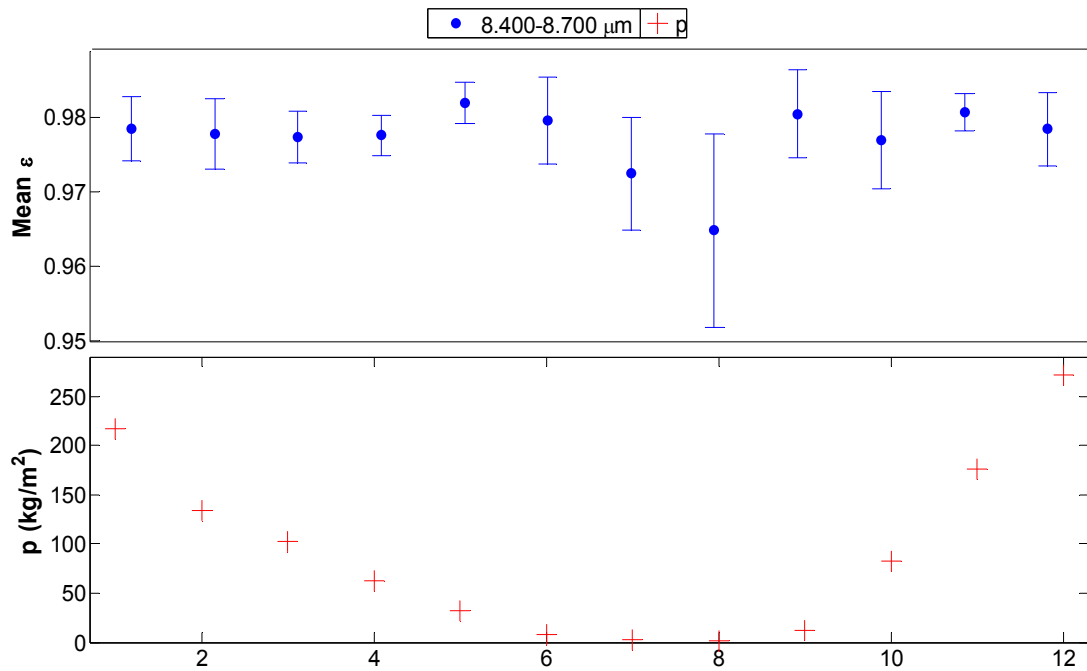
Figure 4-28 The first graph shows monthly ε values averaged over four years for the 8.400-8.700 μm interval. The last graph shows long years averaged p.

To summarize, we found periodic ε values only in the 8.400-8.700 μm interval and determined constant ε values in the remaining wavelength intervals. As a result of this periodicity, Figure 4-28 can be used for the estimation of the monthly ε values in this interval. In Salt Lake, ε values in this wavelength interval are nearly constant. We can conclude that forest cover causes periodic ε values in the 8.400-8.700 μm interval. Moreover, in the calibration region ε values in the 3.660-4.080 μm interval are periodic, contrary to those in Antalya region. Furthermore, we found that ε values in the 8.400-8.700 μm interval decrease with decrease in precipitation during summer for Antalya region, same with the results of Salt Lake. In addition, ε variations in the 8.400-8.700 μm interval due to precipitation are small for Antalya region except July and August. We note that dense cover hinders and dominates underlying surface ε, so we concluded that forest cover cause less ε variations for Antalya region.

Figure 4-29 shows monthly averaged ε values over four years for each month in the six wavelength intervals for Antalya region. This figure is given

to make a comparison between ε values of Antalya region and reference ε values of calibration region.

ε values for Antalya region, which is shown in Figure 4-29, are lower than reference ε values for the calibration region, given in Figure 4-10 in all wavelength intervals and months. Therefore calibration region has expected high emissivity values.

To determine common ε properties of the woodland regions, we compared the results of Küre and Antalya regions. For both regions, ε values in the 8.400-8.700 μm interval are periodic. Different from the Antalya, Küre region has also periodic ε values in the 3.660-3.989 μm interval. This can be explained by the forest type (conifers, deciduous, and mixed forest) differences of these two regions. As a result of these periodicities, we can estimate monthly ε values for these regions. For Salt Lake, we previously found that ε values in the 4.020-4.080 μm interval are periodic contrary to those for two woodland regions. From these differences, we concluded that wavelength intervals, in which ε values are periodic, depend on the land cover type.

In both woodland regions, ε values in all wavelength intervals, which have periodicity, decrease with precipitation decrease in July and August. We concluded that forest ε values in all wavelength intervals are affected from low precipitation occurring in July and August. We could not make any generalization to prove precipitation dependence of ε values, except July and August. As discussed in the previous chapter, dense forest cover dominates underlying surface ε and precipitation is expected to be less effective in densely vegetated woodland regions. As a result, we proved that precipitation does not have great influence on dense woodland regions, except July and August.

Finally, both of the regions have higher monthly ε variations and smaller ε values for all months and bands when compared to calibration region. In the previous section we found ε values of barren-sparsely vegetated regions are also lower than reference ε values. By comparing ε values of these two different regions, we conclude that woodland regions have higher ε values in all wavelength intervals and months than those for barren-sparsely vegetated regions with respect to reference ε values of Salt Lake. As a result forest raises ε values in the land surface as expected.
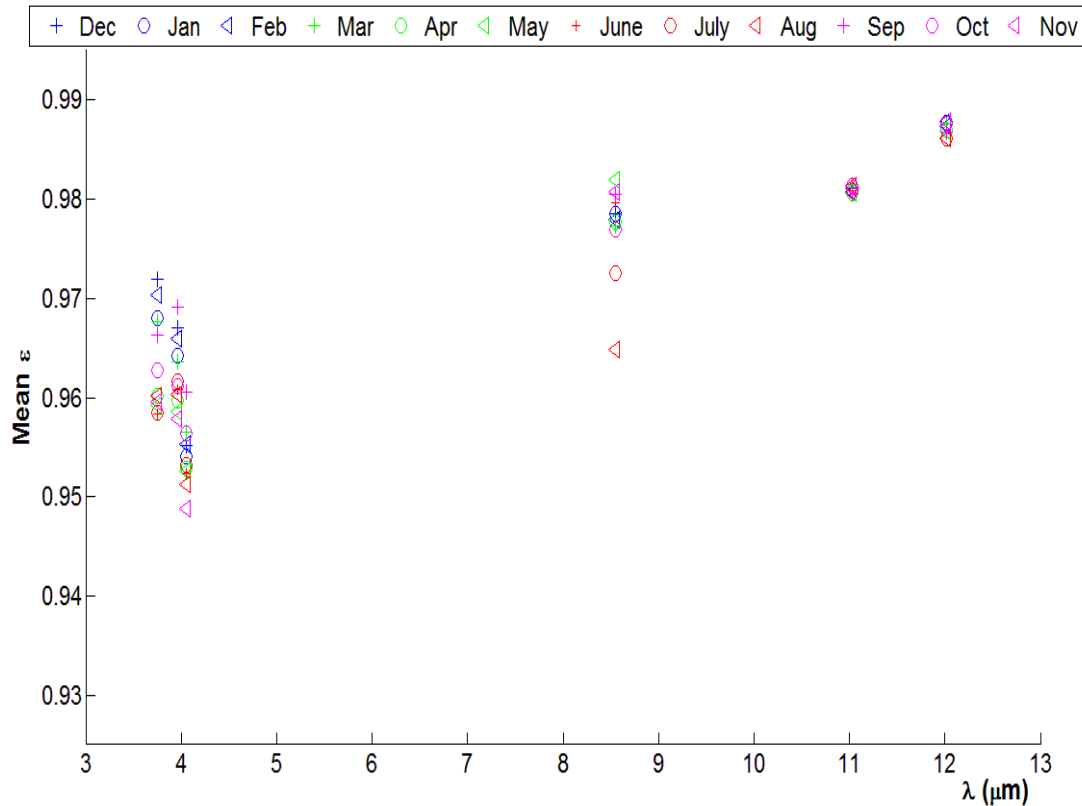
Figure 4-29 Monthly averaged ε values over four years are shown with respect to wavelength (Blue, green, red, and magenta colors represent winter, spring, summer, and autumn seasons, respectively.)

4.2.4 Croplands

For cropland regions we chose Çukurova in Adana and Harran in Şanlıurfa. In the following sections, a detailed investigation of monthly and spectral ε

variations for each region is provided using precipitation and ε_j values of these regions.

4.2.4.1 Harran region

Harran region, shown in Figure 4-30, has an altitude 400 m. approximately [44]. Irrigation-watering, harvesting, cultivating, and fallowing are possible human activities observed mostly in cropland regions. These types of human activities can have influence on ε values resulting in unexpected variations of ε independent from the precipitation. For example, in the Harran cropland, irrigation (watering) is provided within the scope of GAP (Güneydoğu Anadolu Projesi-Southeastern Anatolia Project) [48].

Figure 4-30 View of Harran region (36.89884 ˚N - 38.86537 ˚E) [44].

Calculated monthly ε_j values with their standard deviations are shown in Figure 4-31 for six bands and four years, which are separated with vertical dashed lines. Figure 4-31 shows that ε values are yearly periodic in the 3.929-4.080 µm and 8.400-8.700 µm intervals, but not in the remai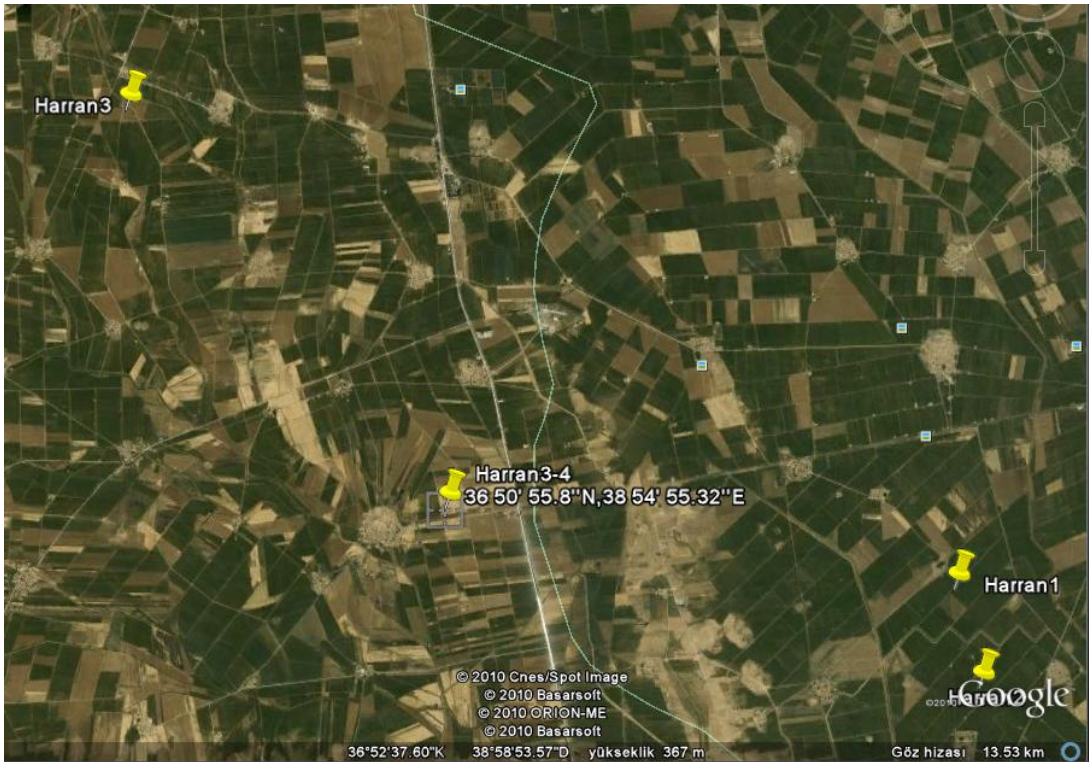ning intervals. High standard deviations of ε values in the 10.780-12.270 µm interval are computed in some months because ε data corresponding to some pixels and years diverge much from the mean. In the 10.780-11.280 µm and 11.770-12.270 µm intervals, we determined constant ε values, which are equal to 0.9819 and 0.9864 with standard deviations of 0.00026 and 0.0014, respectively due to fixed ε values of MODIS in these intervals [31][36][38]. In the 3.660-3.840 µm interval, we can assume constant ε value, which is 0.9558 with the standard deviation of 0.0055. As a result of these constant ε values, we only considered periodic ε values in the 3.929-4.080 µm and 8.400-8.700 µm intervals.

In Figure 4-31, the periodicity in the 3.929-4.080 µm interval is due to the decrease in ε starting from June to August, low ε values in July and August, and high ε values in February. ε values in the 8.400-8.700 µm are also periodic due to the high ε values in May, decrease in ε starting from May to August, low ε values in July and August, and increase in ε starting from August to December. ε values in both intervals are lowest in August and low precipitation occurring in this month can be possible reason for this similarity. A possible influence of precipitation on the periodic behavior of ε is examined using monthly p for Şanlıurfa given in Figure 4-32.

As shown in Figure 4-32, precipitation decreases starting from February to August and low precipitation occurs during summer season. Precipitation increases starting from August to December and has high values during winter and spring. The possible correlation between p and ε values is examined with the graphs shown in Figure 4-33.
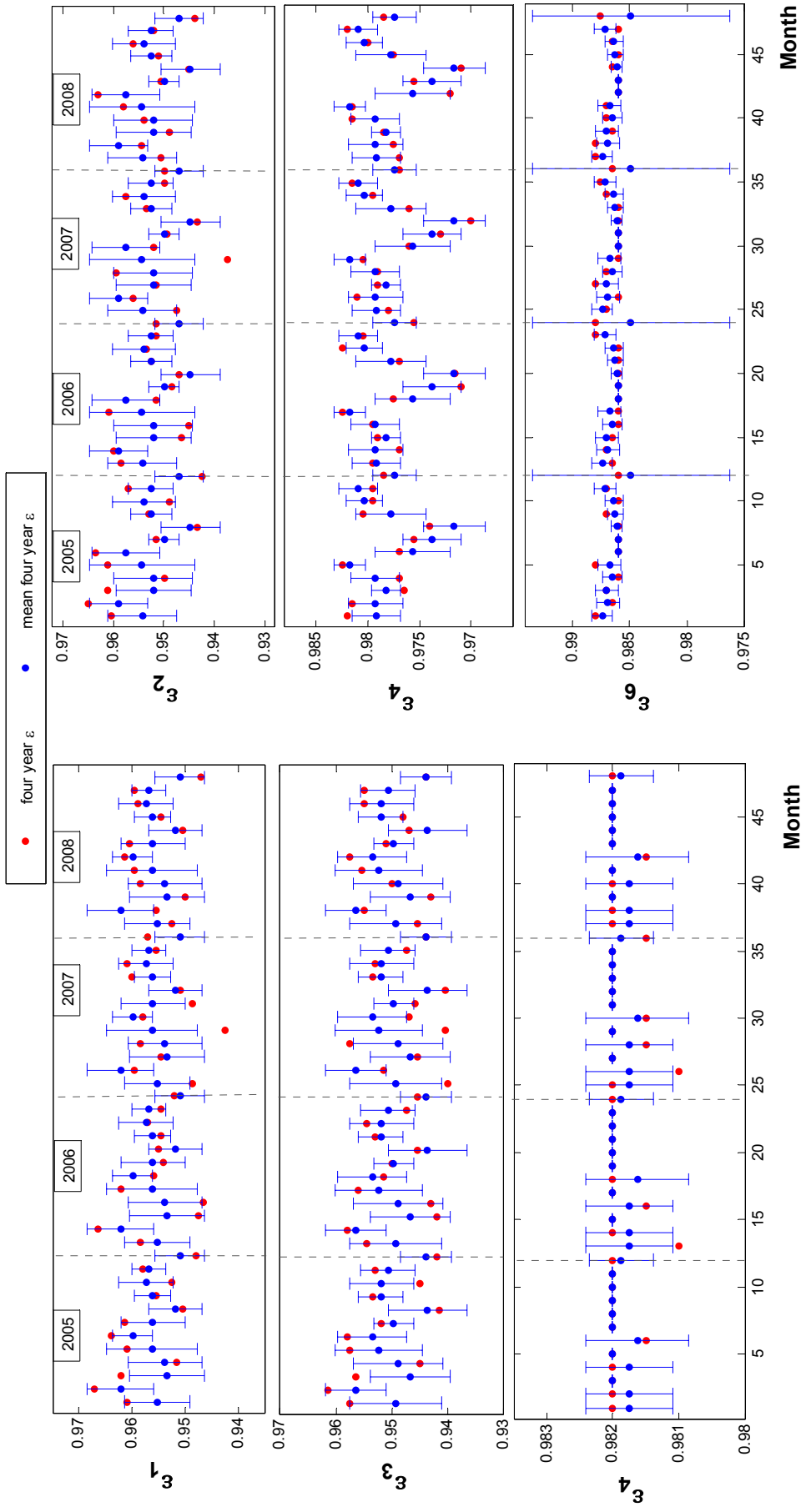
Figure 4-31 Calculated monthly ε_i values of Harran region for four years, which are separated with vertical dashed lines. Red dots show monthly ε values of each four year. Monthly averaged ε values over four years are shown with blue dots and repeated in every year with their errors to check the periodicity. Six graphs for ε_1-ε_6 correspond to six band ε values from 3.660-3.840 μm to 11.770-12.270 μm intervals.
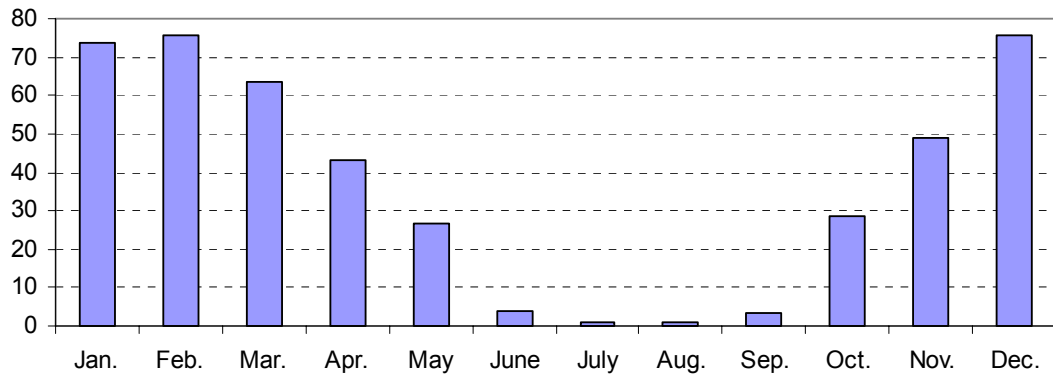
Figure 4-32 Average (1975-2008) monthly p (kg/m^2) for Şanlıurfa [45].
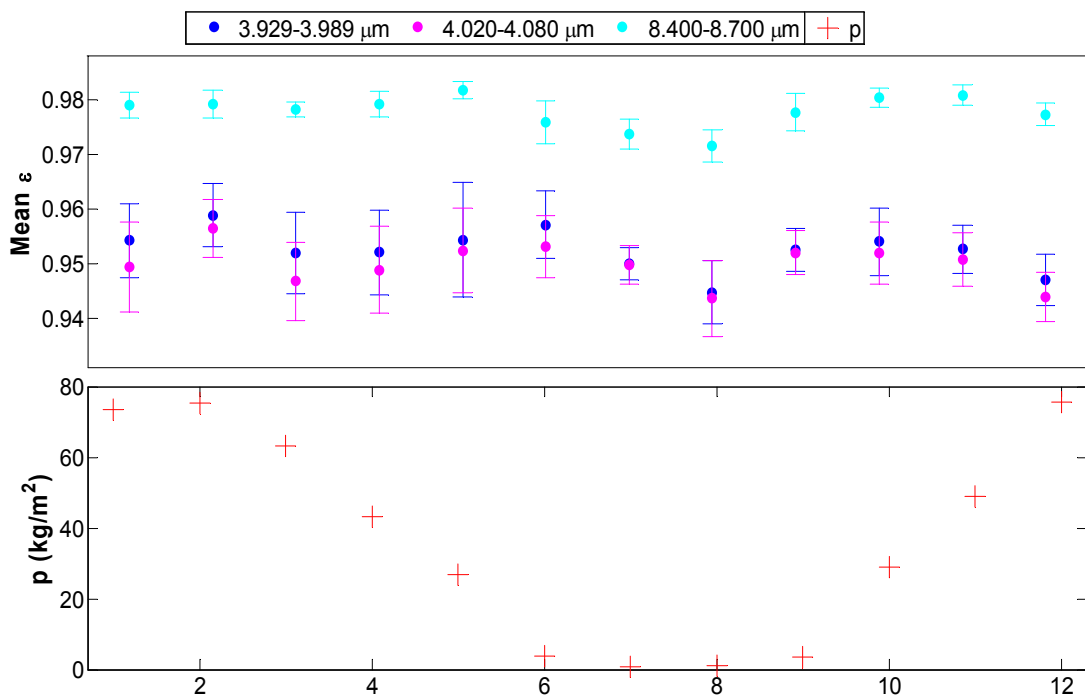
Figure 4-33 The first graph shows monthly ε values averaged over four years for three wavelength intervals. The last graph shows long years averaged p.

Figure 4-33 shows that periodicitiy of precipitation and ε values are higly correlated to each other. Both ε values and precipitation are lowest during summer season and start to increase in August. Similarly, both of them are highest in February and start to decrease in this month. As a result of these correlations, we found that precipitation has a great influence on the ε values in the 3.929-4.080 μm and 8.400-8.700 μm intervals. On the other hand, in December, ε values in the 3.929-4.080 μm interval are not as high as

precipitation and in May ε values in all intervals are high contrary to precipitation. Human activities and GAP mentioned previously can be possible reasons for these unexpected behaviors of ε values independent from the precipitation.

To summarize, we found that ε values are yearly periodic only in the 3.929-4.080 μm and 8.400-8.700 μm intervals. As a result of these periodicities, we can estimate monthly ε values in these two wavelength intervals using Figure 4-33. Different from Harran region, Salt Lake, which is free of vegetation, ε values are periodic in the 3.660-3.840 μm interval and they are not periodic in 8.400-8.700 μm. We found that wavelength intervals, in which ε values are periodic, can be affected by the presence of vegetation (particularly in the 8.400-8.700 μm interval).

For Harran region, we concluded that periodicity of ε values in the 3.929-4.080 μm and 8.400-8.700 μm intervals depend on the precipitation and these values increase (decrease) with high (low) precipitation except for December and May. For both regions (Salt Lake and Harran), we found that ε values are high in spring season and low in July and August. Therefore, we showed that drought in summer and rainfall in spring affect ε values in both regions. Figure 4-34, which shows monthly averaged ε values over four years in Harran, is given to compare ε values of Harran and reference ε values of the calibration region.

We concluded that ε values for Harran region, shown in Figure 4-34, in all wavelength intervals and months are lower when compared to the reference ε values of the calibration region in Figure 4-10. In the next section, Çukurova region is studied to confirm our results for cropland regions.
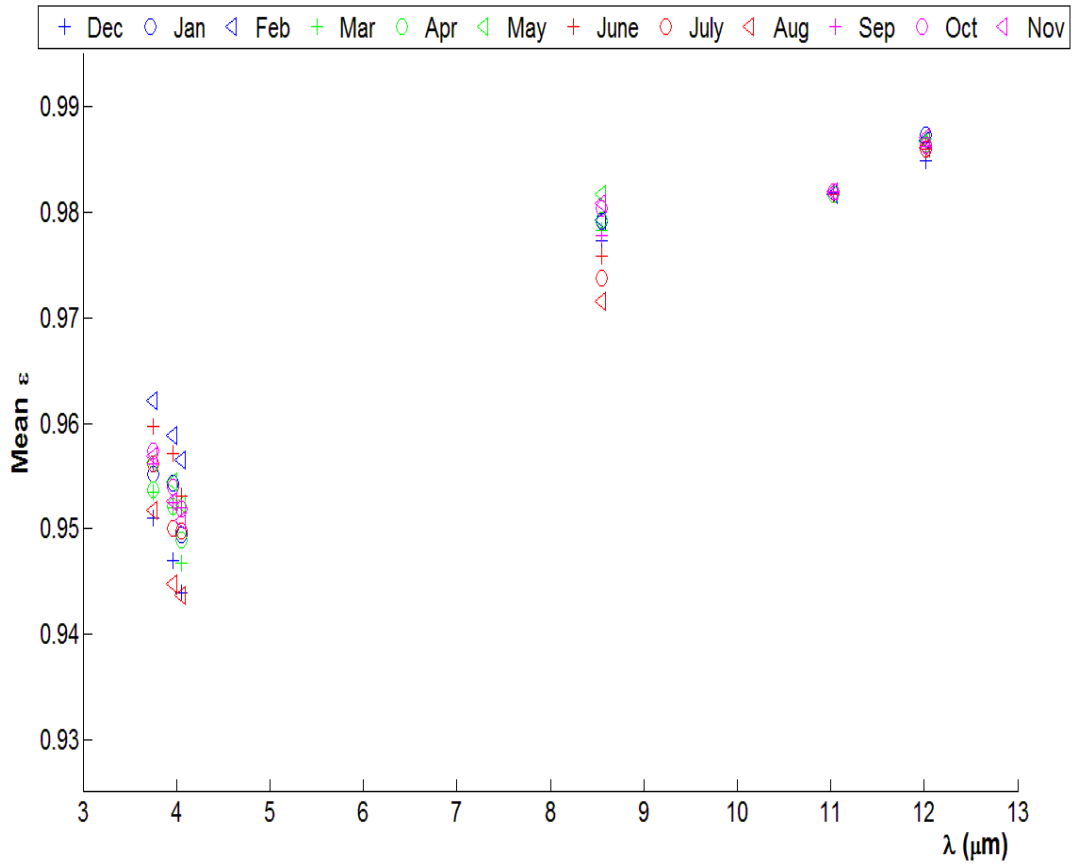
Figure 4-34 Monthly averaged ε values over four years are shown with respect to wavelength (Blue, green, red, and magenta colors represent winter, spring, summer, and autumn seasons, respectively.)

4.2.4.2 Çukurova region

Çukurova region, shown in Figure 4-35, has an altitude 10 m approximately [44]. Human activities, which are irrigation-watering, harvesting, cultivating, and fallowing land, can cause changes in the cropland regions. As a result, ε values can be affected by these changes resulting in unexpected ε variations independent from the precipitation in cropland regions.
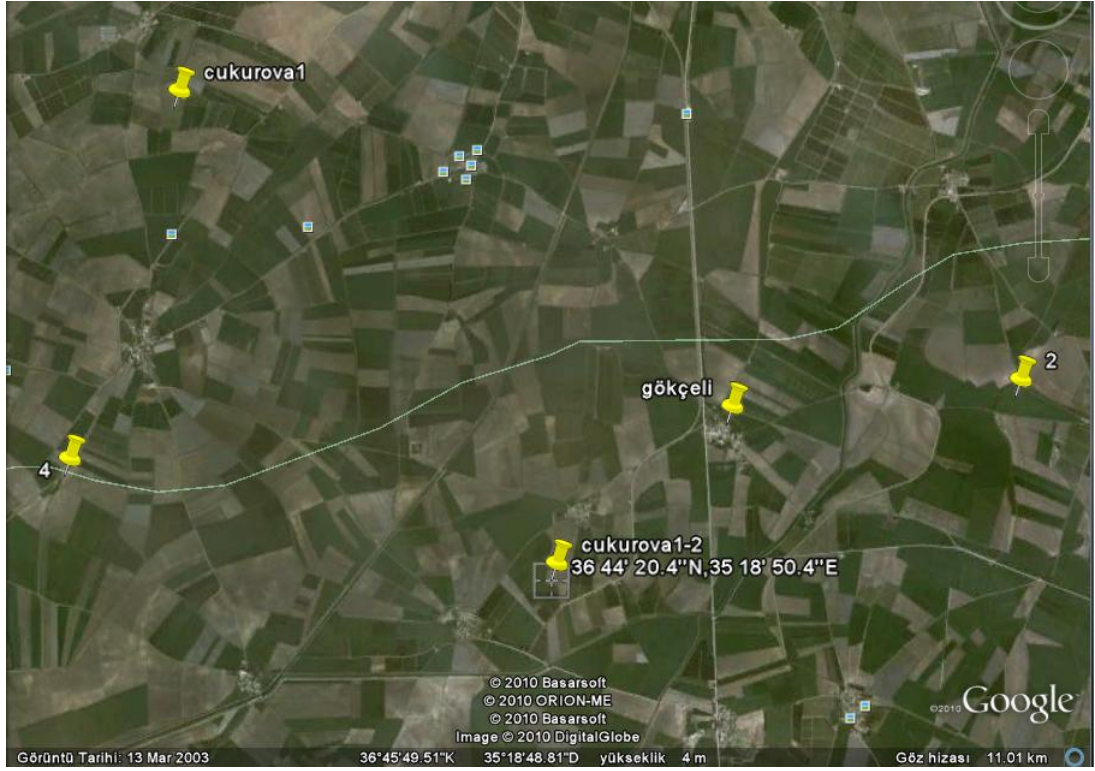
Figure 4-35 View of Çukurova region (36.789˚N -35.314 ˚E) [44].

Calculated monthly ε_j values with their standard deviations are given in Figure 4-36 for six bands and four years. As shown in Figure 4-36 ε values are yearly periodic in the 3.660-4.080 µm and 8.400-8.700 µm intervals. The same figure also shows that ε values are constant in the 10.780-11.280 µm and 11.770-12.270 µm intervals, which are equal to 0.982 and 0.986 with standard deviation of 0.001 respectively, as MODIS algorithm noted [31][36][38]. As a result of these constant ε values, we only considered periodic ε values in the 3.660-4.080 µm and 8.400-8.700 µm intervals.

In Figure 4-36, the periodicity in the 3.660-4.080 µm interval is due to continuous decrease in ε starting from February to August, low ε values in summer season, and high ε values in winter. ε values in the 8.400-8.700 µm are periodic due to decrease in ε values starting from May to August, low ε values in July and August, and high ε values in winter and spring seasons. In order to investigate possible effect of precipitation on the periodic behavior of ε, monthly p for Adana given in Figure 4-37 is used.
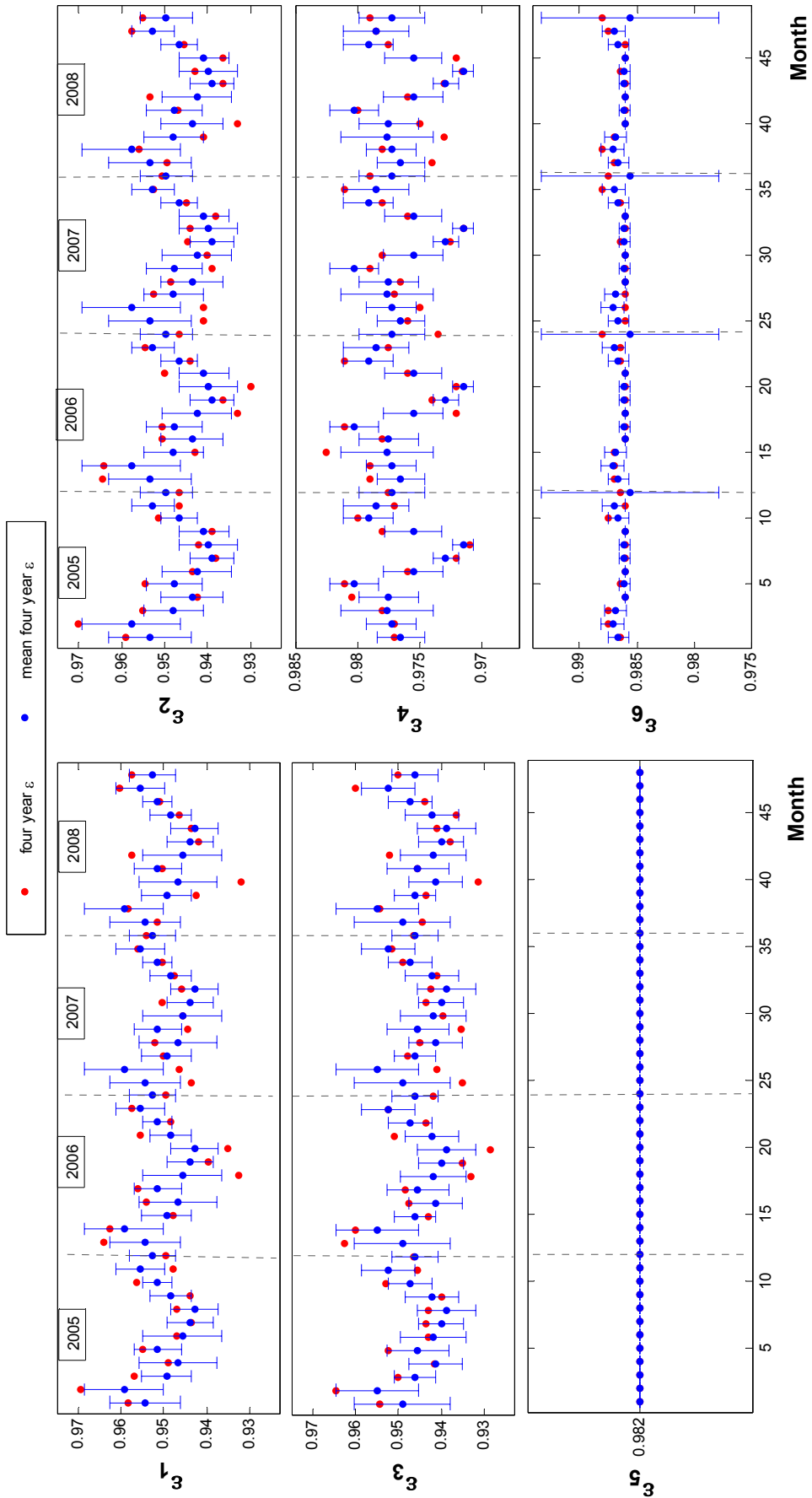
Figure 4-36 Calculated monthly ε_j values of Çukurova region for four years, which are separated with vertical dashed lines. Red dots show monthly ε values of each four year. Monthly averaged ε values over four years are shown with blue dots and repeated in every year with their errors to check the periodicity. Six graphs for ε_1-ε_6 correspond to six band ε values from 3.660-3.840 μm to 11.770-12.270 μm intervals.
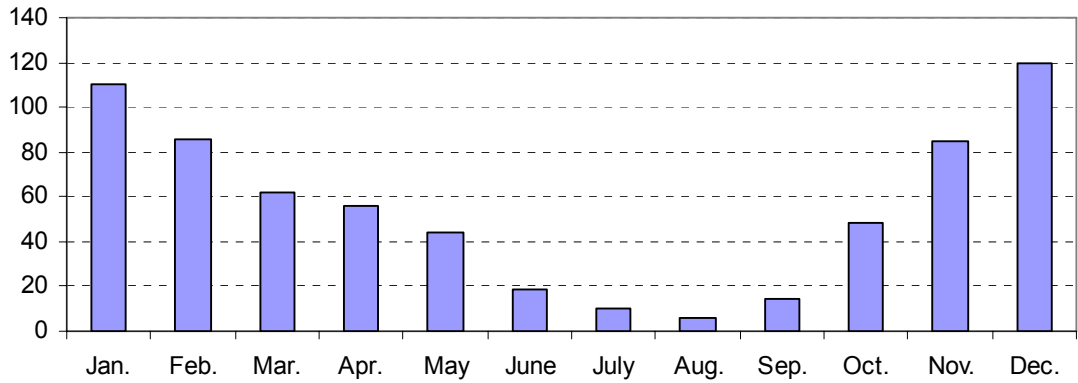
Figure 4-37 Average (1975-2008) monthly p (kg/m^2) for Adana [45].

Figure 4-37 shows that precipitation decreases continuously starting from December to August and low precipitation occurs during summer season (particularly in July and August). Moreover, precipitation increases starting from August to December and high precipitation occurs during winter and spring seasons. The possible correlation between p and ε values is investigated with the graphs shown in Figure 4-38.

As shown in Figure 4-38, periodicitiy of precipitation and ε values are higly correlated to each other. Both ε values and precipitation are high during winter season and start to decrease in this season. Similarly, both of them are lowest during summer season and start to increase in August. As a result of these correlations, we found that precipitation has a great influence of the ε values in the 3.660-4.080 μm and 8.400-8.700 μm intervals. On the other hand, in May ε values in all wavelength intervals are high contrary to precipitation. Human activities (irrigation-watering, harvesting, cultivating, and fallowing land) can be possible reasons for this unexpected behavior of ε values independent from precipitation.
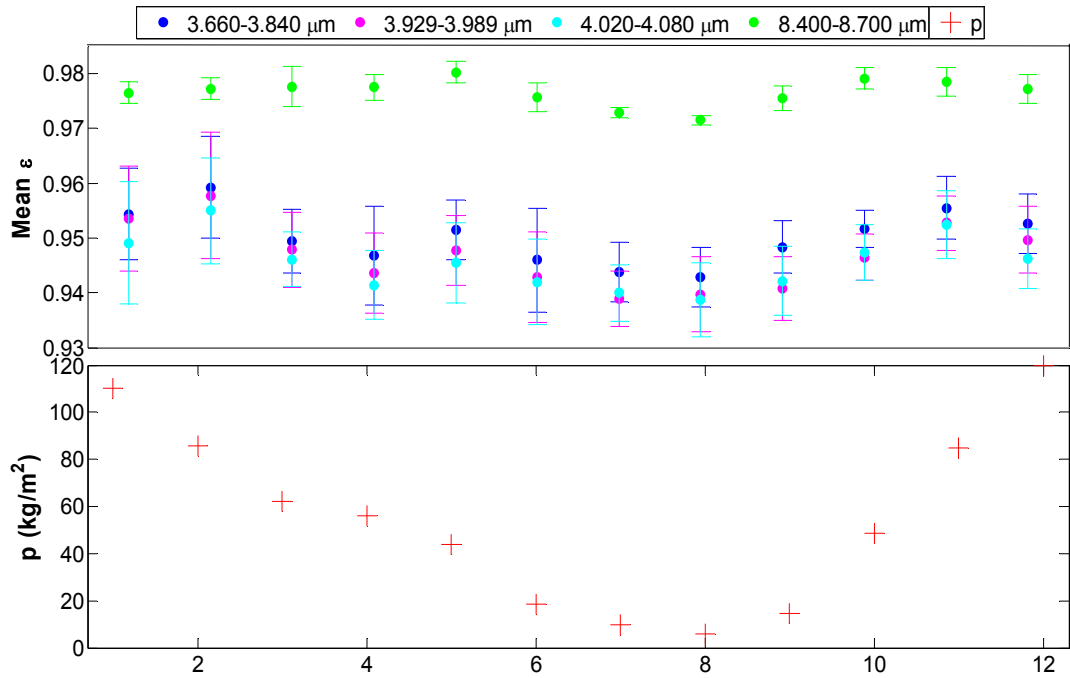
Figure 4-38 The first graph shows monthly ε values averaged over four years for four wavelength intervals. The last graph shows long years averaged p.

As a summary, we found that ε values in the 3.660-4.080 µm and 8.400-8.700 µm intervals are yearly periodic and this periodicity can be used to estimate monthly ε values in these wavelength intervals using Figure 4-38. For Salt Lake, ε values are also periodic in the 3.660-4.080 µm interval, but not in the 8.400-8.700 µm. Therefore, wavelength intervals, in which ε values are periodic, can be affected from the presence of vegetation (particularly in the 8.400-8.700 µm interval).

We concluded that periodicity of ε values in the 3.660-4.080 µm and 8.400-8.700 µm intervals depend on the precipitation and these values decrease (increase) with low (high) precipitation, except May. For Salt Lake and Çukurova regions we found that ε values are high in spring season and low in July and August. Therefore, we found that drought in summer and rainfall in spring affect ε values independent from the land cover type. Figure 4-39 shows monthly averaged ε values over four years in Çukurova region and it is given to compare ε values of Çukurova and reference ε values of calibration region.
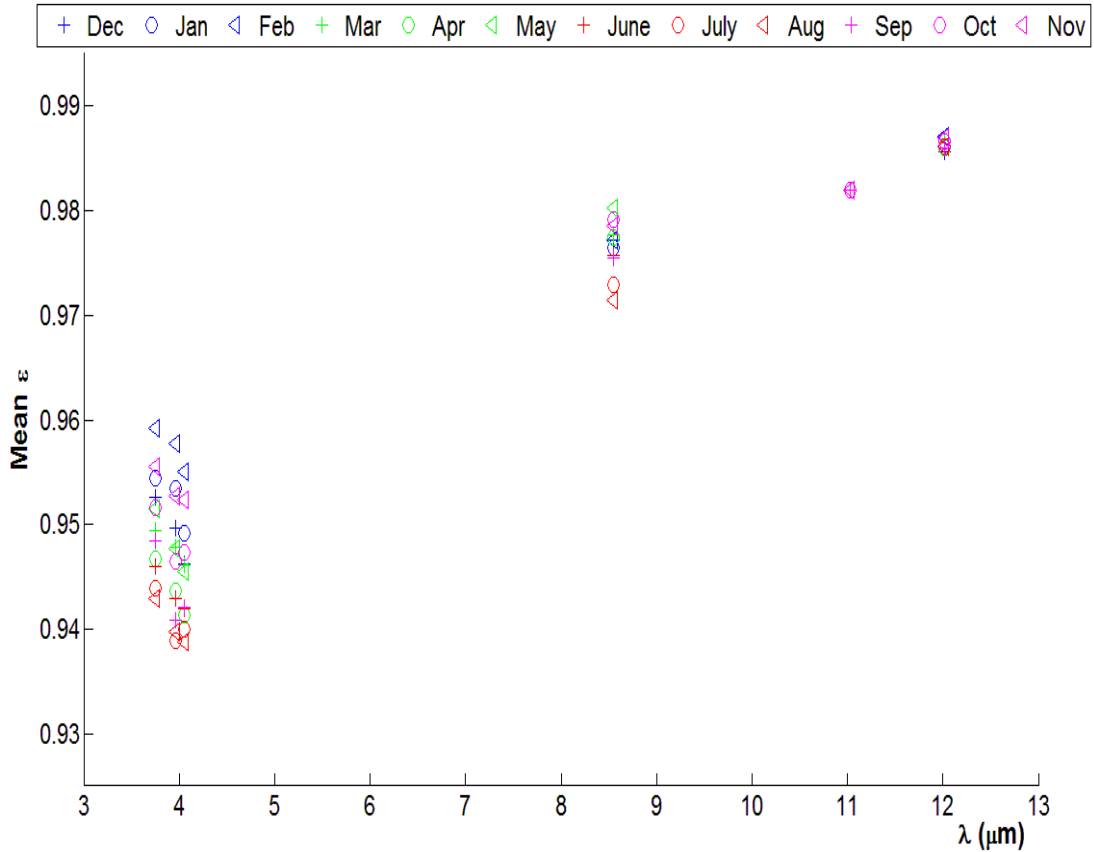
Figure 4-39 Monthly averaged ε values over four years are shown with respect to wavelength (Blue, green, red, and magenta colors represent winter, spring, summer, and autumn seasons, respectively.)

In all wavelength intervals and months ε values of Çukurova region, shown in Figure 4-39, are lower than reference ε values of the Salt Lake, given in Figure 4-10, as expected.

To determine common ε properties of the cropland regions, we compared the results of Harran and Çukurova regions. In both regions, ε values are yearly periodic in the 3.929-4.080 µm and 8.400-8.700 µm intervals and using these periodicities monthly ε values can be estimated for these regions. When periodic ε values for the two regions in Figure 4-38 and Figure 4-33 are compared, we found that ε values and their periodicities of these two regions are very similar to each other, except 3.660-3.840 µm interval. Differences in crop types of these two regions can be the possible reason for this difference. Furthermore, from the comparison of the results

between cropland and calibration region we found that wavelength intervals, in which ε values are periodic, depend on the land cover type. As a result, we determined that ε values in the 8.400-8.700 μm interval are periodic for cropland regions, contrary to Salt Lake.

In both cropland regions, periodic ε values are low during summer season and decrease with low precipitation. They are high during winter season and increase with high precipitation, except May. Therefore, we found that for cropland regions ε values are high in May contrary to the precipitation, due to human activities (irrigation-watering, harvesting, cultivating, and fallowing land). Consequently, we proved that precipitation has a great influence on ε values and ε and precipitation are highly correlated for cropland regions, except May.

Finally, both of the regions have higher monthly ε variations and smallest ε values for all months and wavelength intervals when compared to calibration region. In the previous section we found that woodland ε values are higher than those for barren-sparsely vegetated regions. When ε values of the three regions (barren-sparsely vegetated, woodland and cropland) are compared, we conclude that in all wavelength intervals and months ε values of woodland regions are highest and ε values of the remaining two regions are lower with respect to reference ε values of Salt Lake.

As a summary, for the seven selected regions, we examined emissivity variations for three main land cover type (barren-sparsely vegetated, forest, and cropland) with respect to p and wavelength interval. All selected regions show significant emissivity variations when compared to those for the calibration region. We concluded that precipitation causes monthly ε variations depending on the wavelength interval and land cover type. As a result, for the estimation of monthly ε values, these factors should be taken into account.

CHAPTER 5

RESULTS AND CONCLUSIONS

In this thesis, land cover type, time (season and month), and wavelength dependent emissivity variations examined using precipitation and emissivity data for seven selected regions in Turkey, which have different land cover types and precipitation properties.

It is found that precipitation has a great influence on the emissivity variations. These variations show differences with respect to wavelength and land cover type of the region. Emissivity values are constant in the 10.780-11.280 µm and 11.770-12.270 µm intervals, therefore those bands are not appropriate for the determination of land cover type and investigating precipitation effect. In the 3.660-4.080 µm interval, we found that emissivity variations are highly season dependent for barren-sparsely vegetated and cropland regions. In the 8.400-8.700 µm interval, we showed that barren-sparsely vegetated regions have nearly constant emissivity values contrary to forest and cropland regions. As a result, we can conclude that emissivity variation studies should be performed in the appropriate wavelength interval depending on the land cover type.

Precipitation in summer and winter seasons leads to significant emissivity variations particularly for different regions and wavelength intervals. We found that low precipitation during summer season (drought) decreases the emissivity values of forest and cropland regions dramatically. This decrease occurs in the 8.400-8.700 µm interval for forests and in the 3.929-4.080 µm

and 8.400-8.700 µm intervals for cropland regions. Furthermore, we found that in barren-sparsely vegetated regions, snow cover is the dominant factor on emissivity. Snow cover causes sharp increase of the emissivity values in the 3.660-4.080 µm interval.

Another outcome of the study is that emissivity values in all wavelength intervals are highest for woodland regions among all regions. Most effective parameter on emissivity variations of cropland regions is the amount of precipitation. Küre woodland shows seasonal emissivity variations in three wavelength intervals (3.660-3.840 µm, 3.929-3.989 µm and 8.400-8.700 µm intervals) on the other hand Antalya woodland shows emissivity variations only in one wavelength interval (8.400-8.700 µm interval). Such a difference can arise from tree (conifers, deciduous and mixed) and soil type, local human activities, and local meteorological parameters.

The main contribution of this thesis is the determination of appropriate IR wavelength intervals for the investigation of the seasonal emissivity variations. The results of this study can be used as a prior knowledge for the estimation of emissivity values. Using estimated emissivity values seasonal effects (drought and snow), forest destruction (fire and cutting), surface radiation budget calculations, IR background models, and the basic land cover type classification can be done. As a future work, this work can be expanded to whole Turkey in order to develop season and land cover type dependent spectral emissivity database.

REFERENCES

[1] Elachi C. and Zyl J. V., Introduction to the Physics and Techniques of Remote Sensing, second edition, John Wiley & Sons Inc., 2006.

[2] "Remote Sensing for the Earth Sciences", Manual of Remote Sensing, Third edition, Volume 3, Published in Cooperation with the American Society for Photogrammetry and Remote Sensing, edited by Rencz A. N., John Wiley & Sons Inc., 1999.

[3] Hudson J. R., Infrared System Engineering, Wiley-Interscience, USA, 1969.

[4] Sobrino J. A., Raissouni N., and Li Z. L., "A Comparative Study of Land Surface Emissivity Retrieval from NOAA Data", Remote Sensing of Environment, Vol. 75, 256-266, 2001.

[5] Snyder W., Wan Z., Zhang Y., and Feng Y. Z., "Classification-Based Emissivity for Land Surface Temperature Measurement from Space", Int. J. Remote Sensing, Vol. 19, No. 14, 2753-2774, 1998.

[6] Wan Z., "New refinements and validation of the MODIS Land-Surface Temperature/Emissivity products", Remote Sensing of Environment, Vol. 112, 59-74, 2008.

[7] Liang S., Quantitative Remote Sensing of Land Surfaces, Wiley, 2004.

[8] Zhou L., Dickinson R. E., Tian Y., Jin M., Ogawa K., Yu H., and Schumgge T., "A Sensitivity Study of Climate and Energy Balance Simulations With Use of Satellite-Derived Emissivity Data Over Northern Africa and the Arabian peninsula", Journal of Geophysical Research Letters, Vol. 18, No. D24, 4795, 2003.

[9] Jin M., and Liang S., "An Improved Land Surface Emissivity Parameter for Land Surface Models Using Global Remote Sensing Observations", Journal of Climate, Vol. 19, 2867-28881, June 2006.

[10] Ogawa K., Schmugge T., and Rokugawa S., "Estimating Broadband Emissivity of Arid Regions and Its Seasonal Variations Using Thermal Infrared Remote Sensing", IEEE Trans. Geoscience and Remote Sensing, Vol. 46, No. 2, 334-343, February 2008.

[11] Sobrino J. A. and Raissouni N., "Toward Remote Sensing Methods for Land Cover Dynamic Monitoring: Application to Morocco", Int. Journal of Remote Sensing, Vol. 21, No. 2, 353-366, 2000.

[12] Ogawa K., Schmugge T., and Jacob F., "Estimation of Land Surface Window (8–12 µm) Emissivity from Multi-spectral Thermal Infrared Remote Sensing — A Case Study in a Part of Sahara Desert", Geophysical Research Letters, Vol. 30, 1067, 2003.

[13] Dash P., Göttsche F.-M., Olesen F.-S., and Fizcher H., "Land surface Temperature and Emissivity Estimation from Passive Sensor Data: Theory and Practice–Current Trends", Int. Journal of Remote Sensing, Vol. 23, No 13, 2563-2594, 2002.

[14] Sellers P. J., Rasool S. I., and Bolle H. J., "A review of Satellite Data Algorithms for Studies of Land Surface", Bulletin American Meteorological Society, Vol. 71, No. 10, 1429-1447, 1990.

[15] Turk J., Vivekanandan J., Lee T., Durkee P., and Nielsen K. "Derivation and Applications of Near-Infrared Cloud Reflectances from GOES-8 and GOES-9", American Meteorological Society, Vol. 37, 819-831,1998.

[16] Wan Z., "MODIS Land Surface Temperature Algorithm Theoretical Basis Document (LST ATBD)", Version 3.3, Institute for Computational Earth System Science University of California, Santa Barbara, April 1999.

[17] Justice C. O., Townshend J. R. G., Vermote E.F., Masuoka E., Wolfe R.E., Saleous N., Roy D.P., and Morisette J.T., "An overview of

MODIS Land Data Processing and Product Status", Remote Sensing of Environment, Vol. 83, 3-15, 2002.

[18] Jacob F., Petitcolin F., Schmugge T., Vermote E., French A., and Ogawa K., "Comparison of Land Surface Emissivity and Radiometric Temperature Derived from MODIS and ASTER Sensors ", Remote Sensing of Environment, Vol. 90, 137-152, 2004.

[19] Wan Z., Li Z. L., "A Physics-Based Algorithm for Retrieving Land-Surface Emissivity and Temperature from EOS/MODIS Data", IEEE Transactions on Geoscience and Remote Sensing, 980-996, Vol. 35, No 4, July 1997.

[20] Australian Government Bureau of Meteorology, "Solar Radiation Definitions", www.bom.gov.au/sat/glossary.shtml., last visited on February 2011.

[21] National Institute of Standards and Technology, Math, Statistics, and Computational Science, www.math.nist.gov/, last visited on June 2011.

[22] Umea University, "Rendering, Reflection, BRDF", www8.cs.umu.se/kurser/TDBD12/VT06/lectures/Rendering,%20Reflection,%20BRDF.pdf. , last visited on June 2011.

[23] Princeton University, "A Survey of BRDF Representation for Computer Graphics", www.cs.princeton.edu/~smr/cs348c-97/surveypaper.html., last visited on June 2011.

[24] Wan Z., Zhang Y., Zhang Q., and Li Z.-L., "Quality Assessment and Validation of the MODIS Global Land Surface Temperature", Int. Journal of Remote Sensing, Vol. 25, No 1, 261-274, January 2004.

[25] Salisbury J. W., and D'Aria D. M, "Emissivity of Terrestrial Materials in the 8-14 µm Atmospheric Window", Remote Sensing of Environment, Vol. 42, 83-116, 1992.

[26] Salisbury J. W., and D'Aria D. M, "Emissivity of Terrestrial Materials in the 3-5 µm Atmospheric Window", Remote Sensing of Environment, Vol. 47, 345-361,1994.

[27] Petitcolin F, Vermote E., "Land Surface Reflectance, Emissivity and Temperatutre From MODIS Middle and Thermal Infrared Data", Remote Sensing of Environment, Vol. 83, 112-134, 2002.

[28] Chen Y., Sun-Mack S., Minnis P., Smith W. L., and Young D. F., "Surface Spectral Emissivity Derived from MODIS Data", Optical Remote Sensing of the Atmosphere and Clouds III, Proceedings of SPIE, Vol. 4891, 361-369, 2003.

[29] NASA MCST WEB, www. mcst.gsfc.nasa.gov, last visited on August 2011.

[30] Salisbury J. W., D'Aria D. M., "Infrared (8-14 µm) remote sensing of soil particle size", Remote Sens. Environ., Vol. 42, No 3, 157-165, November 1992.

[31] Hulley G. C., Hook S. J., and Baldridge M., "Investigating the Effects of Soil Moisture on Thermal Infrared Land Surface Temperature and Emissivity Using Satellite Retrievals and Laboratory Measurements", Remote Sensing of Environment, Vol. 114, 1480-1493, 2010.

[32] Lesaignoux A., Fabre S., Briottet X., and Olioso A. "Influence of Surface Soil Moisture on Spectral Reflectance of Bare Soil in the 0.4 - 15 µm Domain", 6th EARSeL SIG IS workshop, European Association of Remote Sensing Laboratories Workshop. 16-19 March 2009, Israel.

[33] Lesaignoux A., Fabre S., Briottet X. and Olioso A., "Soil Moisture Impact on Reflectance of Bare Soils in the Optical Domain [0.4-15 µm]", 2nd Workshop on Remote Sensing and Modeling of Surface Properties, 9 - 11 June 2009, Météo France, Toulouse, France.

[34] Mira M, Valor E., Boluda R., Caselles V., and Coll C., "Influence of Soil Water Content on the Thermal Infrared Emissivity of Bare Soils:

Implication for Land Surface Temperature Determination", Journal of Geophysical Research, Vol. 112, F04003, 2007.

[35] Mira M., Valor E., Caselles V., Rubio E., Coll C., Galve J. M., Niclos R., Sanchez J. M., and Boluda R., "Soil Moisture Effect on Thermal Infrared (8-13 μm) Emissivity", IEEE Trans. Geoscience and Remote Sensing, 2251-2260, Vol. 48, No 5, May 2010.

[36] Schmugge T., Ogawa K., and De Rosnay P., "Satellite Observations of the Land Surface Emissivity in the 8-12 μm Window: Effect of Soil Moisture", Remote Sensing for Environmental Monitoring and Change Detection (Proceedings of Symposium), Perugia, July 2007.

[37] Ogawa K., Schumugge T., and Rokugawa S., "Observations of Soil Moisture Dependence of Thermal Infrared Emissivity on Soil Moisture", Geophysical Research Abstracts, Vol. 8, 2006.

[38] Hulley G. C., and Hook S. J., "Intercomparison of versions 4, 4.1 and 5 of the MODIS Land Surface Temperature and Emissivity Products and Validation with Laboratory Measurements of Sand Samples From the Namib Desert, Namibia", Remote Sensing of Environment, 1313-1318, Vol. 113, 2009.

[39] Elvidge C. D., "Thermal Infrared Reflectance of Dry Plant Materials: 2.5-20.0 μm", Remote Sensing of Environment, Vol. 26, 1988.

[40] MODIS UCSB (University of California, Santa Barbara) Emissivity Library, www.icess.ucsb.edu/modis/EMIS/html/em.html, last visited on June 2011.

[41] Synder W. C., Wan Z., Zhang Y., and Feng Y, "Thermal Infrared Bidirectional Reflectance Measurements of Sands and Soils", Remote Sensing of Environment, 265-285, Vol. 60, 1997.

[42] Evrendilek F., Gulbeyaz Ö, "Deriving Vegetation Dynamics of Natural Terrestrial Ecosystems from MODIS NDVI/EVI Data over Turkey", 5270-5302, Sensors, Vol. 8, 2008.

[43] The USGS Remote Sensing Technologies Project, www.calval.cr.usgs.gov/sites_catalog_template.php?site=tuzg, last visited on June 2011.

[44] Google Earth, www.earth.google.com/intl/tr/, last visited on August 2011.

[45] Turkish State Meteorological Services, www.dmi.gov.tr/veridegerlendirme/, last visited on July 2011.

[46] Ekercin S. and Örmeci C., "Evaluating climate change effects on water and salt resources in Salt Lake, Turkey using multitemporal SPOT imagery", Environmental Monitoring and Assessment, 361-368, Vol. 163, 361–368, 2010.

[47] Tübitak Ulusal Gözlemevi (Tübitak National Observatory), www.tug.tubitak.gov.tr/gozlemevi.php, last visited on August 2011.

[48] Güneydoğu Anadolu Projesi (Southeastern Anatolia Project), www.gap.gov.tr/, last visited on August 2011.

[49] MODIS, www.modis.gsfc.nasa.gov/about/specifications.php, last visited on June 2011.

[50] Orman Envanteri, www.ogm.gov.tr/, last visited on June 2011.

[51] Küre Kaymakamlığı, www.kure.gov.tr/, last visited on August 2011.

APPENDIX

SURFACE RADIATION BUDGET

Surface radiation budget (SRB), shown in Figure A-1, determines the amount of incoming solar radiation and outgoing terrestrial radiation [7][9]. Surface energy model characterizes the land surface processes such as ecological, hydrological, and biogeochemical [7][9].
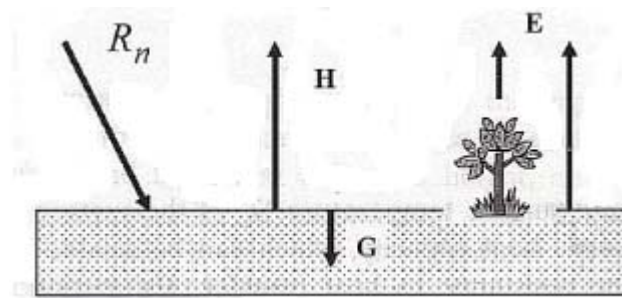

Figure A-1 Surface radiation budget illustration [7].

In Figure A-1, R_n is the total net radiation (W/m^2) and is conducted into the surface through ground heat flux, G (W/m^2). H is the sensible heat flux and the rest of the net radiation is the latent heat flux (evapotranspiration, E) [7][9].

Surface energy balance equation, given in Equation (A-1), is a major interaction between the land surface models and atmosphere [7][9].

$$R_n = H + E + G = S_\downarrow - S_\uparrow + LW_\downarrow - LW_\uparrow \qquad \textbf{(A-1)}$$

In this equation, R_n is the total surface net radiation, i.e. difference between the downward and upward shortwave and longwave radiations, where $S_\downarrow$ and $S_\uparrow$ is downward and upward solar radiation (W/m^2), $LW_\downarrow$ and $LW_\uparrow$ downward and upward longwave radiation (W/m^2), respectively [1][8][9][13].

A.1. Emissivity Impact

Effect of emissivity can be theoretically analyzed by considering LW_n given in Equation (A-2) where Kirchhoff's Law can be applied to $LW_\downarrow$ and $LW_\uparrow$ is defined from the Stephan-Boltzmann Law, which implies that emitted radiance is proportional to the fourth power of the absolute source temperature as given below [7]-[9][13].

$$LW_\uparrow = \varepsilon \sigma T_s^4$$
$$LW_n = LW_\downarrow - LW_\uparrow = \alpha L_\downarrow - \varepsilon \sigma T_s^4 \qquad \textbf{(A-2)}$$
$$LW_n = \varepsilon (L_\downarrow - \sigma T_s^4)$$

Equations in (A-3) indicate that the magnitude of any changes in LW_n and surface temperature T_s is proportional with the change in emissivity. With this change, the new balance equation becomes as in Equation (A-4).

$$\Delta LW_n = (L_\downarrow - \sigma T_s^4)\Delta\varepsilon - 4\sigma\varepsilon T_s^3 \Delta T_s$$
$$\frac{\Delta T_s}{\Delta\varepsilon} = \frac{1}{4\sigma\varepsilon T_s^3}\left[(L_\downarrow - \sigma T_s^4) - \frac{\Delta LW_n}{\Delta\varepsilon}\right] \qquad \textbf{(A-3)}$$

$$S_n + LW_n = H + E + G \Rightarrow \Delta LW_n - \Delta E \approx 0 \qquad \textbf{(A-4)}$$

Equation (A-4) suggests that change in emissivity not only affects LW_n and T_s, but also E. These changes can be observed in the Figure A-2.
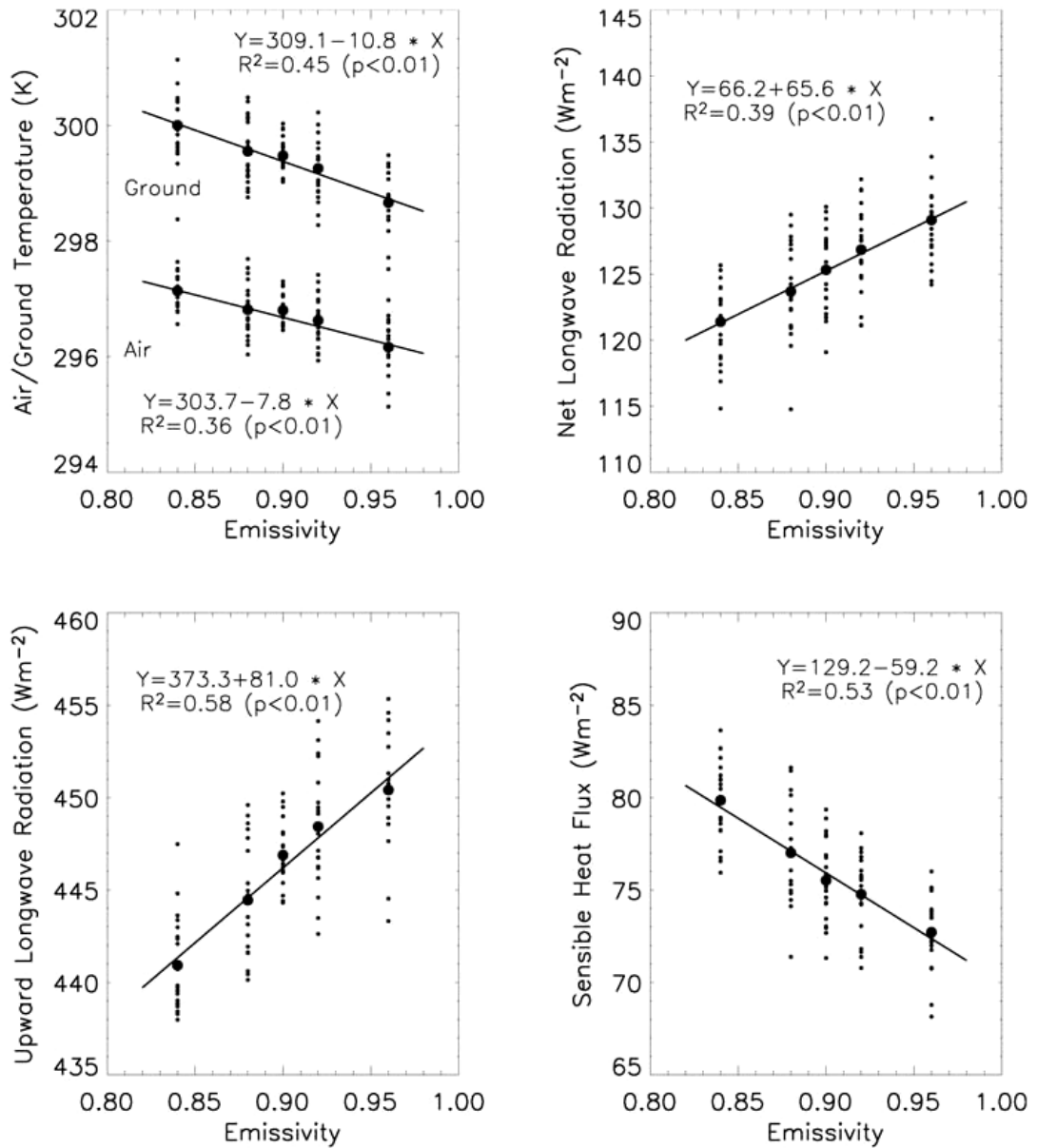
Figure A-2 Changes in air and ground temperature, LW_n, $LW_\uparrow$, and H with emissivity. The smaller dot represents annual means and the larger dot represents the 20-year average [8].

In Figure A-2, the results indicate that a decrease of soil emissivity by 0.1 will increase ground and air temperature by 1.1°C and 0.8°C, respectively and decrease LW_n and $LW_\uparrow$ by 6.6 W/m^2 and 8.1, W/m^2, respectively [8]. The decreased LW_n is balanced by an increase of sensible heat flux of about 5.9 W/m^2. In addition, all these relations vary seasonally and Figure A-3 shows seasonal variations of these parameters [8].
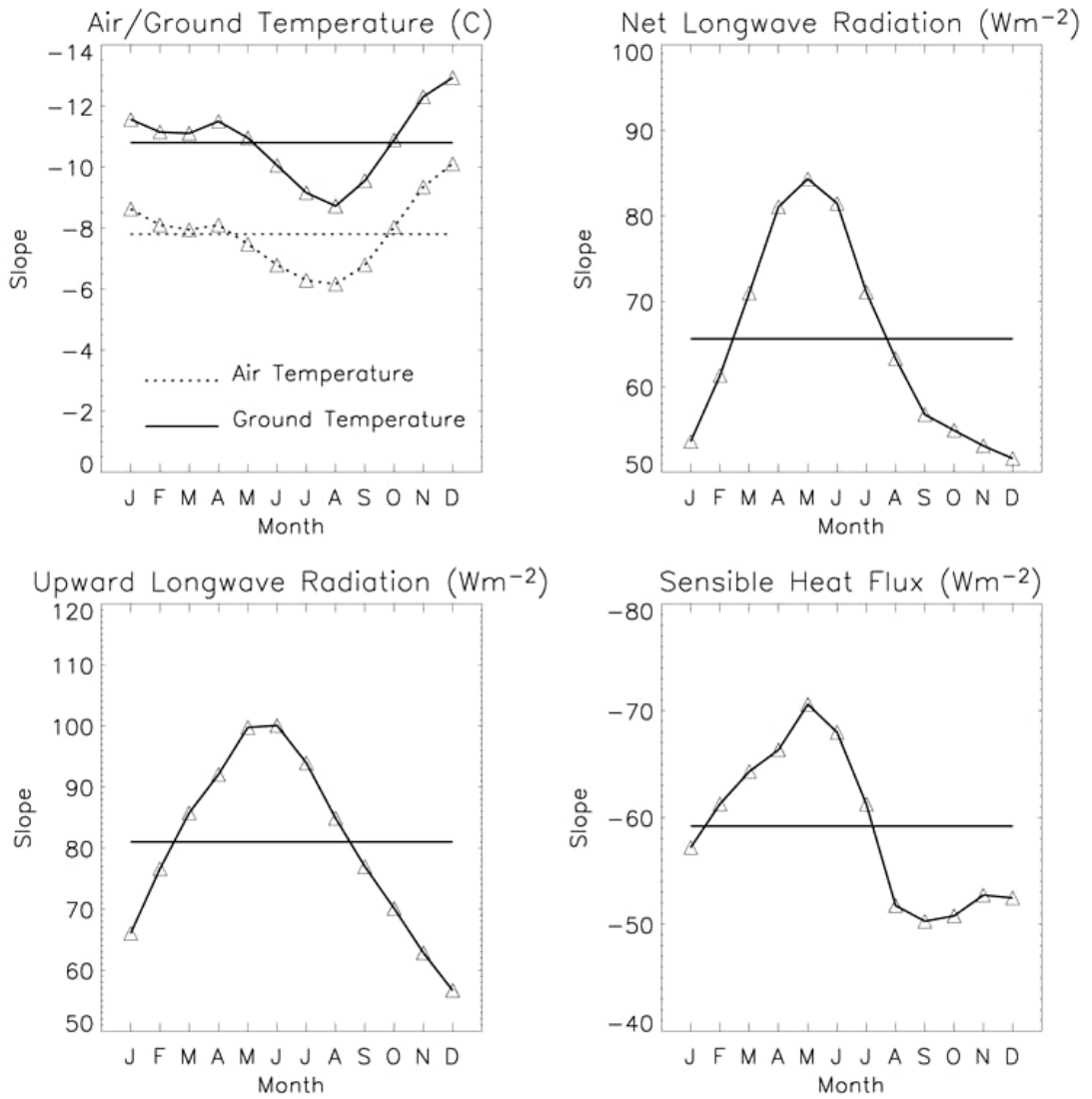
Figure A-3 Seasonal variations of air and ground temperature, LW_n, $LW_\uparrow$, and H. Slopes are estimated from Figure A-2 [8].

Figure A-3 shows that an increase in spring and decrease at the end of summer is observed as expected in the climate models [8].

A. 3. Constant Emissivity Assumption

Constant emissivity assumption introduces errors in surface radiation calculations. For example, when emissivity is assumed to be equal 1.0, it results in maximum errors, as can be seen in the Equation (A-5) [9].

$$LW_n^{\varepsilon=1} = LW_\downarrow - \sigma T_s^4$$

$$\Delta = LW_n^{\varepsilon\neq1} - LW_n^{\varepsilon=1} = \underbrace{(\sigma T_s^4 - LW_\downarrow)}_{A}\underbrace{(1-\varepsilon)}_{B} \qquad \text{(A-5)}$$

Here Δ defines the error in the LW_n if accurate emissivity is not taken into account in the land surface models. Due to inaccurate emissivity assumption, the surface emissivity departs from the unity by the term B and there are large differences between the $LW_\uparrow$ and $LW_\downarrow$ by the term A. This error is especially large for bare soil with little moisture and vegetation because these areas have small emissivity values that are far from 1.0 [9]. Figure A-4 shows impact of emissivity change on LW_n for the sensitivity run ($\varepsilon=0.90$) minus control run ($\varepsilon=0.96$) in the land surface model of the Community Land Model version 2 (CLM2) [9].
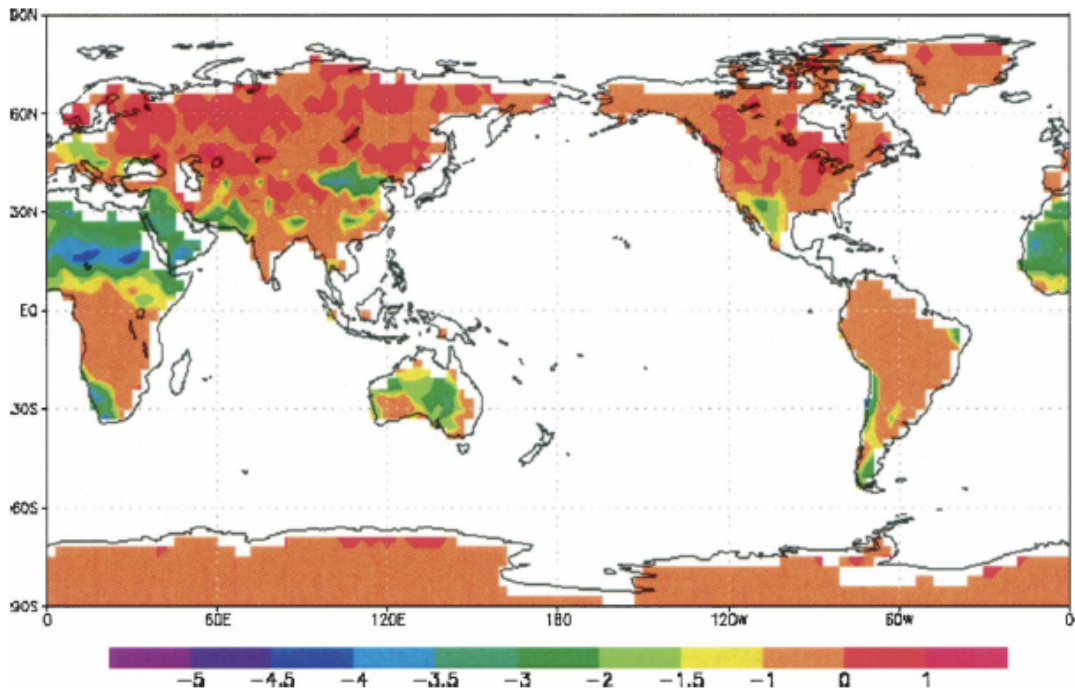

Figure A-4 Impact of emissivity change on LW_n for the sensitivity run ($\varepsilon=0.90$) minus control run ($\varepsilon=0.96$) for daily averages of January 1998 [9].

As shown in Figure A-4, the largest changes are observed over Sahara Desert region with 1-5 W/m^2 [9]. The effects of emissivity in land surface and

climate system can also be investigated by using NCAR Community Atmosphere Model version 2 coupled with CLM2 (CAM2-CLM2) in Figure A-5 [9].
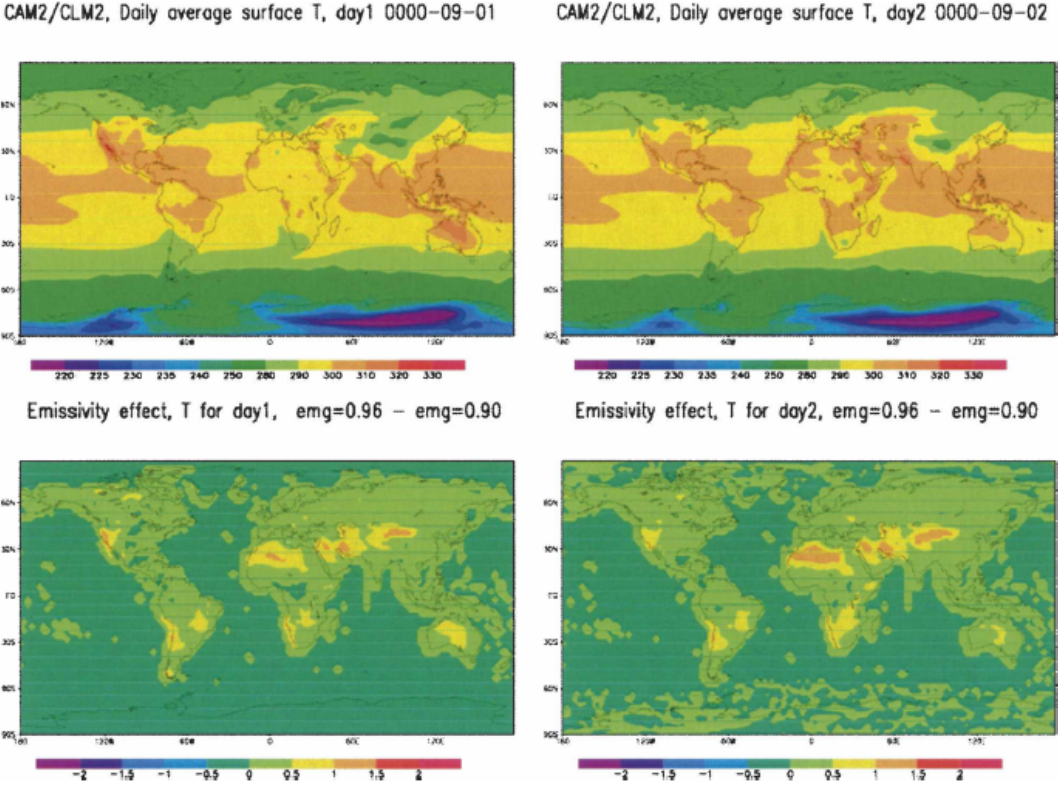

Figure A-5 Emissivity impacts on daily averaged surface air temperature in coupled model CAM2-CLM2 for two different days (a)-(b) Control run (c)-(d) the control run minus the sensitivity run [9].

In Figure A-5, a decrease of surface temperature occurs due to decrease in emissivity [9].

All of these results indicate that simple representations of the land surface emissivity in current SRB and climate models need to be improved based on satellite and in situ measurements and time dependent emissivity variations should be taken into account.